Improved Performance in Plasmonic Biosensors for Bacterial Detection Through Dielectric Conditioning and Dielectrophoretic Enhancement

Daniel David Galvan II

A dissertation

submitted in partial fulfillment of the

requirements for the degree of

Doctor of Philosophy

University of Washington

2018

Reading Committee:

Qiuming Yu, Chair

François Baneyx

Buddy Ratner

Program Authorized to Offer Degree:

Department of Chemical Engineering

University of Washington

Abstract

Improved Performance in Plasmonic Biosensors for Bacterial Detection Through Dielectric Conditioning and Dielectrophoretic Enhancement

Daniel David Galvan II

Chair of the Supervisory Committee:
Prof. Qiuming Yu
Department of Chemical Engineering

The need for rapid and specific pathogen detection is of utmost importance. Current culture based methods are time consuming, and more efficient technologies would benefit wide-ranging fields including food safety, biomedicine, homeland security, and environmental monitoring. Plasmonic biosensing, such as surface-enhanced Raman scattering (SERS) or surface plasmon resonance (SPR), can afford real-time interrogation of the unique biochemical composition of pathogenic bacteria. However, plasmonic measurements, void of complex labels or long integration times, are typically conducted with concentrated samples (10^8 CFU/mL) of pure cultures that are far outside the clinically relevant range. Real-world samples are often dilute ($< 10^3$ CFU/mL), and present in bacterial mixtures and/or complex media.

The objective of this work is to develop SERS and SPR-based approaches to enable real-time detection of dilute and/or mixed bacterial samples. To combat these issues, we have developed a two-pronged plasmonic-based approach using: (1) long-range SERS (LR-SERS)

devices to extend the effective sensing volume, and (2) SERS and SPR microfluidic devices integrated with dielectrophoresis (DEP) for the concentration and selective detection of bacterial targets. In the former, SERS-active nanohole arrays (NHAs) were embedded in refractive index-matched environments, and resulted in extension of the effective sensing region. Finite-difference time-domain simulations were conducted to investigate the plasmonic response of NHAs in symmetric and asymmetric dielectric environments. The optimal structures were fabricated, and the SERS signals of surface bound analytes dramatically increased when placed in the refractive index-matched environment. Furthermore, SERS signals were observed at a distance of 10 nm from the nanohole array surface. The increased penetration depth could enable examination of the unique bacterial composition between the peripheral cell wall and cytoplasm.

In the latter, DEP was incorporated into the SERS biosensor by dual-function, nanostructured electrodes. "Point-and-plate" and "interdigitated" electrode configurations were studied with respect to SERS detection performance. Generally, bacteria localize on the sensing surface in regions with high or low electric field gradients depending on the unique cellular dielectric properties. The effect of the applied AC frequency on the capture efficiency and SERS signals of bacteria was investigated for the point-and-plate configuration. Application of DEP afforded the successful detection of 10^5 CFU/mL *E. coli* solutions, and the applied electric fields did not alter the SERS spectra of Gram-positive and Gram-negative bacteria. Additionally, DEP-active SPR chips containing interdigitated electrodes enable sensitive, rapid, and selective *E. coli* detection. The DEP-SPR strategy enabled sensitive detection of *E. coli*, with a limit of detection of 3×10^2 CFU/mL. Integration of secondary antibody amplification led to selective detection of *E. coli* in the presence of concentrated (10^8 CFU/mL) non-target bacteria in ~2 h.

TABLE OF CONTENTS

LIST OF FIGURES

LIST OF TABLES

ACKNOWLEDGEMENTS

I have so many people to thank for their support throughout my graduate studies. First off, I would like to thank my advisor, Prof. Qiuming Yu, for her financial and intellectual support. Her mentorship has been truly appreciated, and I commend her for the lab environment that she has cultured. I feel fortunate to have been able to work in her lab, which facilitates such forward-looking scientific research aimed at addressing some of the most pressing issues in biotechnology, energy, and nanotechnology.

Additionally, I would like to thank Profs. François Baneyx and Buddy Ratner who served as on my Committee for my Prelim, General, and Final Exams. I am grateful for your time and insightful feedback. I would also like to thank Profs. Bo Zhang and Karl Böhringer for serving as my GSR during the General and Final Exams, respectively. I am thankful for the helpful communications over the years as well as hospitality of Dr. Jiří Homola and his Optical Biosensors team at the Institute of Photonics and Electronics in Prague, Czech Republic.

I am grateful to my current and past lab mates in the Yu Group including Dr. Beau Richardson, Dr. Fang Sun, Dr. Chao Hao, Dr. Ping Wu, Monica Esopi, Erjin Zheng, Gabriella Tosado, Yu-Han Ho, Vidit Parehk, Yi-Yu Lin, Xiaoyu Zhao, Erika Green, Abdulrahman Almutairi, Hannah Morgan, Jason Smith, Yajie Zhu, E-Lin Liu, and Henry Armas-Amaya. Their comradery, support, and intellectual stimulus have been wonderful to be apart of, and I will truly miss sharing the lab with them.

Finally, I would like to thank all my friends and family for their undiminishing support. To my wife, Amanda, I must say completion of this degree would not have been possible without you. You were my rock and compass when things got tough, keeping me grounded and helping

me find my way. For that I thank you. You inspire me and make me whole, and I look forward to the next chapter of our lives. I would like to say thank you to my parents and sister for their constant encouragement, and for instilling scientific curiosity in me at a young age. Finally, I would like to thank all my old friends back home in Tucson, and all the new ones I made in Seattle for sharing great times together.

Chapter 1. INTRODUCTION

1.1 CURRENT LANDSCAPE OF BACTERIAL BIOSENSORS

The need for rapid and reliable pathogen detection is of utmost importance on the global scale. Currently, culture based methods are the gold standard for bacterial diagnosis. However, culture based methods are time consuming, and depending on the specific bacterial strain a successful diagnosis can take upwards of 48 hours.[1-3] More efficient technologies are necessitated to reduce the time for positive bacterial identification. Such technologies would benefit wide-ranging fields of study such as food safety, biomedicine, homeland defense, and environmental monitoring. For example, the Centers for Disease Control and Prevention (CDC) estimates that food-borne pathogens are responsible for ~48 million new cases of infections annually,[4] and the costs associated with food-borne illness alone in the United States reached $55.5 billion.[5] Furthermore, the time delay between sample collection and diagnosis in the clinical setting has led to the over prescription of wide-spectrum antibiotics, resulting in an increase in antibiotic resistance and the emergence of 'superbugs'.[6-8] Technologies aimed at reducing bacterial detection times would have profound global benefits.

Biosensors are one class of technologies that can potentially address the need for more effective bacterial diagnosis. In 2013 the US market for bacterial diagnostic devices was estimated at ~$1.8 billion.[9] However, further research and development is necessary to achieve the US Defense Threat Reduction Agency's metrics for an ideal biosensor that are "rapid (under 6 hours), phenotypic, portable, and work(s) directly from a clinical sample".[10]

1.2 Basic Principles of Plasmonic Biosensors for Bacterial Detection

Biosensors, in the simplest sense, are comprised of a biorecognition element and electrical transducer (optical, electrical, piezoelectrical, etc.).[11] The biorecognition element brings the target analyte out of the surrounding environment and in intimate contact with the transducer. The transducer records the biorecognition event as an electrical signal, which can be processed into an analytical relationship with the quantity and/or composition of the target analyte. Performance characterization of biosensors is determined by the limit of detection (LOD), specificity, range of detection, and multiplexed capabilities. The LOD is determined by the lowest concentration at which positive identification can be achieved by the biosensor. Specificity refers to the ability of the biosensor to reject non-specific adsorption of contaminants (such as proteins, debris, or non-targeted bacterial cells) that may be present in the sample. The range of detection is the concentration range in which a linear response is obtained by the biosensor, ideally covering orders of magnitudes. Multiplexing is simultaneous recognition of multiple bacterial analytes.

Biorecognition elements define the critical interface between the sample and the transducer, and can improve all performance characteristics. Antibodies have been heavily utilized as biorecognition elements across all classes of bacterial biosensors.[12] The large, Y-shaped proteins can specifically interact with their target bacterial strain, while displaying little to no affinity towards additional bacterial cells that may be present in the sample. More recently, aptamers, or single-stranded DNA sequences, have taken predominance as the biorecognition element due to their low cost, chemical stability, and large-scale synthetic processing.[13-17] Additional biorecognition elements include bacteriophages, carbohydrates, and electrostatic-based approaches.

The biosensor transducer is responsible for conversion of the biorecognition event into an electrical signal that can be used for quantification and analysis of the bacterial target. Transduction strategies vary greatly, but the primary strategies include electrochemical, piezoelectrical, and optical. Surface plasmon resonance (SPR) and surface-enhanced Raman scattering (SERS) are two of the most widely employed optical transduction mechanisms for bacterial biosensing.

SPR biosensors rely on the generation of charge oscillation of conduction band electrons at a metal/dielectric interface through attenuated total internal reflection (ATIR) of incident light (Fig. 1.1a).[18] When the ATIR condition is satisfied light energy is absorbed, which causes a dip in the absorption spectrum at a specific wavelength (λ_{SPR}). The absorbed light generates surface plasmon polaritons (SPPs) that propagate along the metal/dielectric interface and evanescently decay away from the interface. The SPPs and λ_{SPR} are sensitive to changes in the local dielectric environment of the metal/dielectric interface, which result in a shift in λ_{SPR}. Adsorption of target analytes can be detected by monitoring the shift in λ_{SPR} (Fig. 1.1b).

SERS biosensors capitalize on the SPP-facilitated increase in the Raman scattering efficiency. Raman scattering has proven to be a powerful analytical technique for bacterial studies because it is non-invasive, oblivious to water, and can give specific vibrational information, or 'chemical fingerprints'.[19-21] The unique chemical fingerprinting has enabled both fundamental and applied studies of bacterial samples including antimicrobial susceptibility testing[22-24] and differentiation of bacterial strains.[25-27] However, Raman scattering is a weak process, and ~1 out of 10^6 photons experiences Raman scattering.[28] The discovery of surface-enhanced Raman scattering (SERS) facilitated a great expansion in the capabilities of traditional Raman spectroscopy.[29-32]

SERS biosensors require the generation of SPPs. SERS occurs on nanostructured, noble-metal surfaces due to coupling between conduction band electrons and the electric field component of incident light (Fig. 1.1c).[33] A bifurcated enhancement mechanism, consisting of electromagnetic and chemical components, can lead to amplification of inelastically scattered, Raman photons by a factor of 10^{14}.[34-36] The chemical enhancement can contribute up to 10^2 to the EF,[35] but the overall EF is dictated by the electromagnetic component.[36] Chemical enhancement results from electron transfer of π-bond electrons in surface-bound analytes with the conduction band electrons on the noble metal surface.[33] Electromagnetic enhancement is attributed to the generation of localized surface plasmon resonance (LSPR) on the nanostructured surface.[37] LSPR confines the incident light, and generates amplified electric fields on the nanostructures (a.k.a 'hot-spots'). Analytes adsorbed on, or in the immediate vicinity of the nanostructured surface can interact with the electric field (Fig. 1.1c), and produce the unique SERS spectra (Fig. 1.1d).

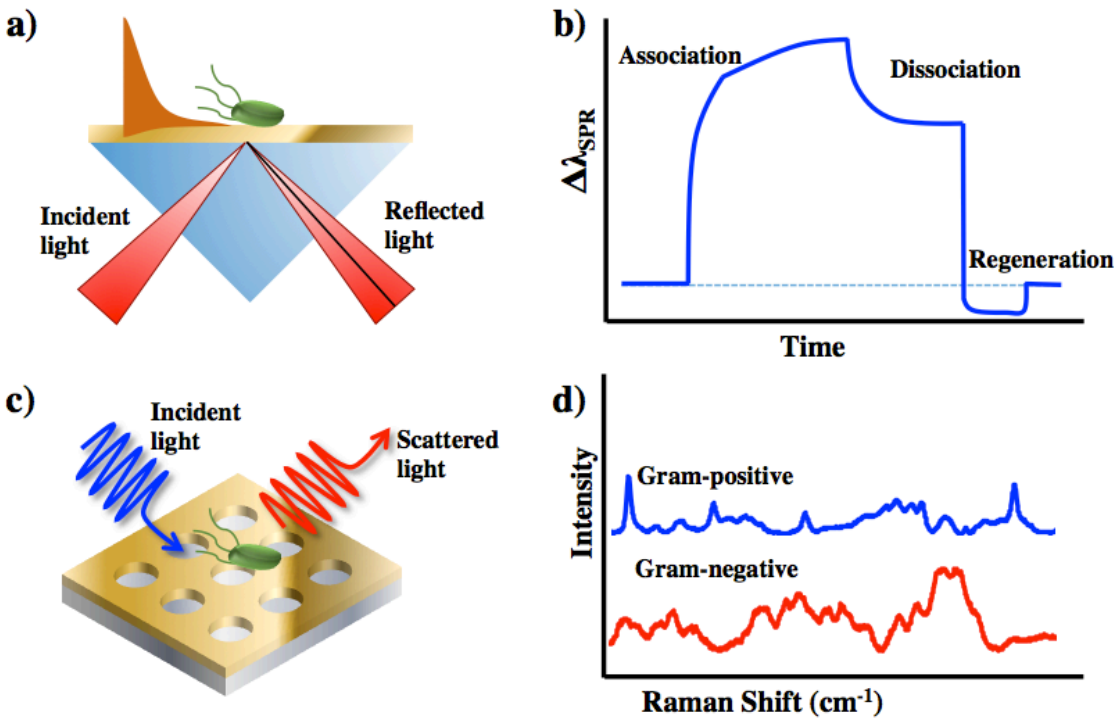

Figure 1.1. Schematic illustrations of a) SPR biosensing configuration with b) typical SPR sensorgram, and c) nanostructured SERS-active surface with d) typical Gram-positive and Gram-negative SERS spectra.

Both SPR and SERS detection require interaction of the bacterial cell wall with the transducer surface. Bacterial cell walls vary considerably, and are broadly separated into two categories: Gram-positive and Gram-negative.[38] The peripheral layers of Gram-positive and Gram-negative are primarily composed of peptidoglycans and lipopolysaccharides, respectively (Fig. 1.2). Both categories contain a heterogeneous landscape containing membrane-bound proteins that carry out diverse functions. In SPR sensing, differentiation of bacterial analytes is facilitated by interaction of the bacteria with bacterial-specific, immobilized biorecognition elements, generating a shift in λ_{SPR}.[39] SERS bacterial differentiation is achieved by direct interaction of the bacterial cell wall with the SERS-active transducer.[40] The inherent differences in bacterial cell walls are observed in the 'chemical fingerprints', which can be used to differentiate bacteria to the strain level.[41]

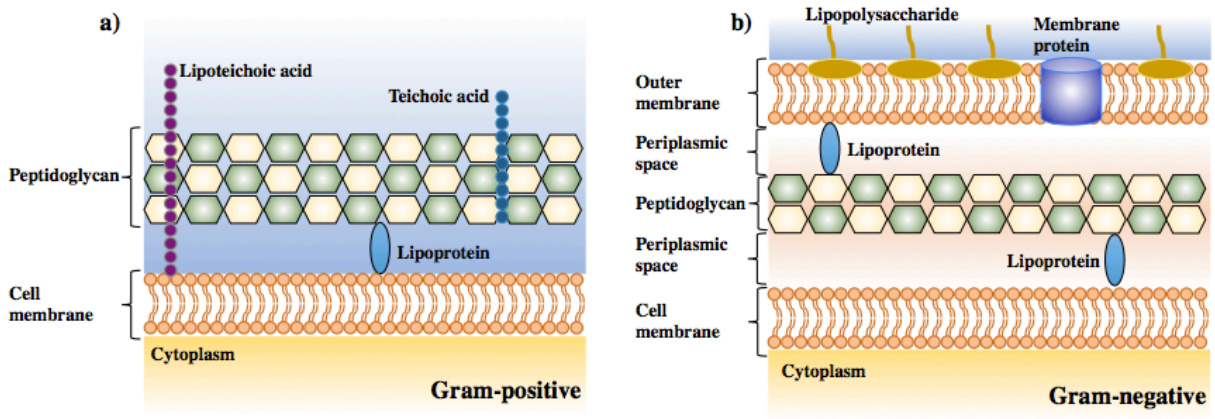

Figure 1.2. Cell wall structures of a) Gram-positive and b) Gram-negative bacteria.

Currently, bacterial biosensing with SPR or SERS is often limited by high concentration bacterial samples that are suspended in a controlled, pure environment.[2, 42] Detection of low concentration bacterial suspensions in SPR sensing has remained elusive without the addition of complicated detection schemes such as fluorescence labeling[43] or nanoparticle sandwich assays.[44] While these approaches have demonstrated LODs as low as 15 CFU/mL,[43] the additional materials and instruments required increase the cost and analysis time and negate the sensitivity benefits.[3, 45] For SERS, analytes must come within ~2 nm of the nanostructured surface to experience Raman scattering amplification.[46-49] The near-field effect results in the use of high concentration (typically > 10^8 CFU/mL),[42] or exhaustively long diffusion times; both of which are undesirable to applied studies. While LODs of 71 CFU/mL have been theoretically reported for SERS bacterial biosensing,[50] the experimental setup and complex materials required are infeasible for clinical or field-based applications. Finally, microfluidic approaches to SPR or SERS bacterial biosensing suffer from diffusion-limited mass transport of bacterial cells to the transducer surface, which lead to higher LODs and read out times.[51]

Therefore, strategies are necessitated to overcome the current plasmonic-based biosensing limitations to achieve real-time and specific identification of bacterial samples. The work presented here describes two possible routes to achieve this goal: (1) incorporation of long-

range surface plasmons in SERS devices to extend the sensing region past the ~2 nm limit, and (2) integrate dielectrophoresis in SERS and SPR microfluidic devices to overcome the diffusion-limited mass transport of bacterial cells to the sensing surface. An introduction to long-range surface plasmons and dielectrophoresis are given in the following sections, prior to discussion of the work performed.

1.3 Long-Range Surface Plasmons for Surface-Enhanced Raman Scattering (SERS)

Localized surface plasmon resonance (LSPR) on nanostructured, noble metal surfaces is generally accepted as dominant with enhancement mechanism of SERS.[36] However, the amplified electric fields responsible for EM enhancement decay rapidly from nanostructured surfaces. Multiple studies have been conducted to investigate the distance at which the SERS intensity decays from nanostructured surfaces including, ultrathin cladding layers[46] and alkane thiols[47] on electrochemically roughened Ag films, atomic layer deposition of Al_2O_3 on Ag nanodots fabricated via nanosphere lithography,[48] SiO_2-coated Ag nanosphere dimers,[49] and DNA conjugated with Raman probes on Au nanoparticles.[52] Results vary from substrate to substrate and due to differences in the experimental setup, but there is agreement that within ~2 nm from the sensing surface the SERS signal is effectively diminished. Thus, SERS is considered a near-field effect, and although it is unnecessary for a molecule to adsorb on the surface for excitation, it must come in the immediate vicinity of the light coupling nanostructure. The shortcomings created by the near-field effect necessitate the development of SERS substrates with 'long-range' capabilities through electric field extension, enabling molecular detection at distances beyond the current SERS-active substrates.

One route to achieve field extension in SERS-active substrates is to create metal/dielectric interfaces that support long-range surface plasmon resonance (LR-SPR).[53, 54] LR-SPR is a unique SPR mode. Generally, SPR is the cumulative oscillation of conduction band electrons induced through coupling to the electric field component of incident light at the interface of metal and dielectric materials.[39] Evanescent waves produced on SPR-supporting 50 nm gold films on glass substrates (n ~1.52) extend into the metal film and aqueous dielectric environment (n = 1.33), with penetration depths of 25 nm and 400 nm, respectively for near infrared excitation.[18] LR-SPR is excited when the metal film is made ultrathin (i.e. ~20 nm), and placed in a symmetrical dielectric environment (i.e. the refractive indices on either side of the film are equal).[55] The two stipulations allow the evanescent waves at opposite interfaces to couple, thus producing LR-SPR (Fig. 1.3). The main features offered by LR-SPR include strong electric fields at the metal surface, narrow reflectance bands, and extended electric field penetration depths.[56] Typical penetration depths in LR-SPR are 1.2 μm, compared to 400 nm for conventional SPR.[18, 55] LR-SPR was theoretically predicted by solving the SPR dispersion relation as a function of metal film thickness,[57] and experimentally verified by determining the propagation and attenuation constants of thin metal films.[58] Since then, LR-SPR has been implemented in a variety of SPR biosensing studies including antibody-antigen binding events,[59] SPR-coupled fluorescence emission,[60] and sensitive biosensing for bacterial[61] and eukaryotic cells.[62]

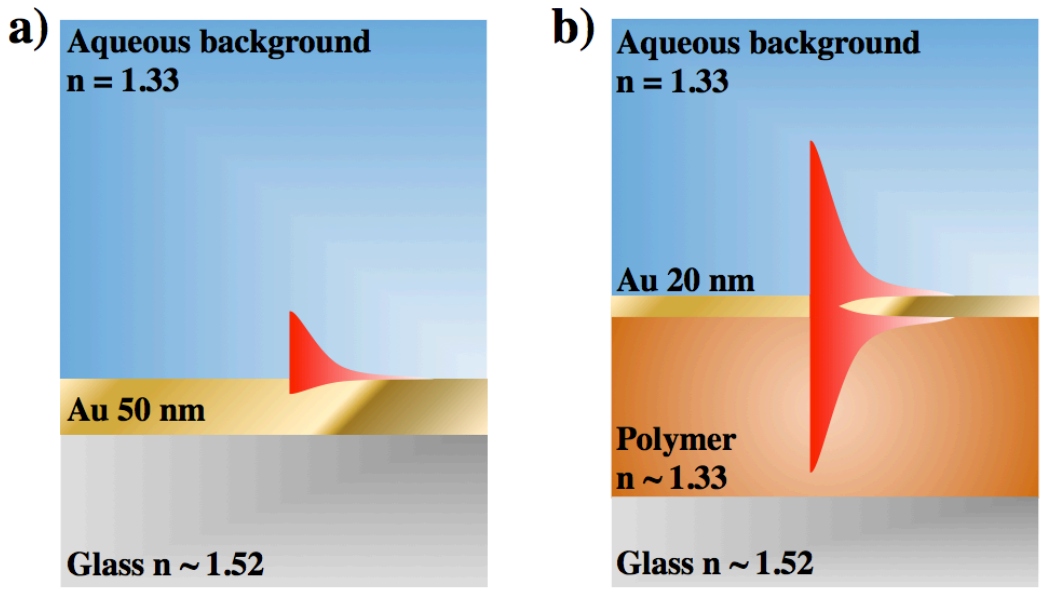

Figure 1.3. Dielectric configurations for the generation of a) conventional and b) long-range surface plasmons.

LR-SPR generated with ultrathin Ag films has demonstrated the long-range SERS (LR-SERS) effect. Liu *et. al.* utilized the Kretschmann configuration to generate LR-SPR by separating an ultrathin Ag film (16 nm) with a 1750 nm MgF_2 layer (n = 1.38) from the underlying glass substrate.[53] Because the refractive index of MgF_2 is close to that of water (n = 1.33), the Ag film satisfied the symmetrical dielectric condition, and thus supported LR-SPR generation. The extended electric fields produced by the LR-SPR enabled detection of 4-mercaptopyridine monolayers SERS signals at a distance of ~500 nm away from the Ag film. Later work by the researchers used the same device architecture with the addition of Ag NPs into the aqueous solution to increase the sensitivity through Ag film-NP coupling.[54]

1.4 Fundamental Theory of Dielectrophoresis (DEP)

Current research and development of plasmonic-based biosensors is often focused on the detection and identification of concentrated (> 10^5 CFU/mL) bacterial suspensions, with analytical studies conducted at concentrations as high as 10^8 CFU/mL.[42] These concentrated

samples fall well outside of the target sensitivity for bacterial biosensors, which can be as low as 10^3 CFU/mL for certain applications.[63, 64] For dilute suspensions, diffusion-limited mass transport of the bacterial cells to the SERS-active surface will result in undesirably long detection times.[51] Multiple strategies have been proposed to overcome diffusion-limited mass transport in bacterial biosensors including magnetic particles,[65, 66] microfluidic focusing,[67] and dielectrophoresis (DEP).[68] Of which, DEP has shown potential to reduce identification times of bacterial species by providing an externally applied force to overcome slow mass transport of the cells.[50, 69-73]

DEP is the motion of a particle due to the presence of a non-uniform electric field.[74] Unlike electrophoresis, DEP can be applied to both charged and neutral particles. The non-uniform field produces internal polarization of the particle and an associated dipole moment. Particle movement is dictated by the direction of the dipole, the dielectric properties of the particle and the surrounding medium, particle size, as well as the magnitude and frequency of the AC field. The time averaged dielectrophoretic force experienced by the particle can be described by:

$$\langle \vec{F}_{DEP} \rangle = 2\pi \cdot \varepsilon_m \cdot r^3 Re[f_{CM}(\omega)] \cdot \nabla \left| \vec{E} \right|^2 \qquad \text{Eq. 1.1}$$

where ε_m is the electric permittivity of the suspending medium, r^3 is the radius of the particle, $f_{CM}(\omega)$ is the frequency dependent Clausius-Mossotti (CM) factor, ω is the frequency of the applied AC field, and $\vec{E}$ is the electric field vector. The CM factor describes the relative polarizability of the particle with respect to the suspending medium, and for a homogeneous, spherical particle is defined as:

$$f_{CM}(\omega) = \frac{\varepsilon_p^* - \varepsilon_m^*}{\varepsilon_p^* + 2\varepsilon_m^*} \qquad \text{Eq. 1.2}$$

where ε_p^* and ε_m^* represent the frequency-dependent complex permittivities of the particle and suspending medium, respectively. Furthermore, for non-conductive particles the conductivity term can be broken down into surface and bulk components. The particle permittivity, media permittivity, and particle conductivity are defined as:[75]

$$\varepsilon_p^* = \varepsilon_p - j\frac{\sigma_p}{\omega} \quad \text{Eq. 1.3}$$

$$\varepsilon_m^* = \varepsilon_m - j\frac{\sigma_m}{\omega} \quad \text{Eq. 1.4}$$

$$\sigma_p = \sigma_b + \frac{2K_s}{r} \quad \text{Eq. 1.5}$$

where ε and σ denote the electrical permittivity and conductivity, respectively, σ_b is the particle bulk conductivity, K_s is the particle surface conductivity, r is the radius of the particle, and $j = \sqrt{-1}$.

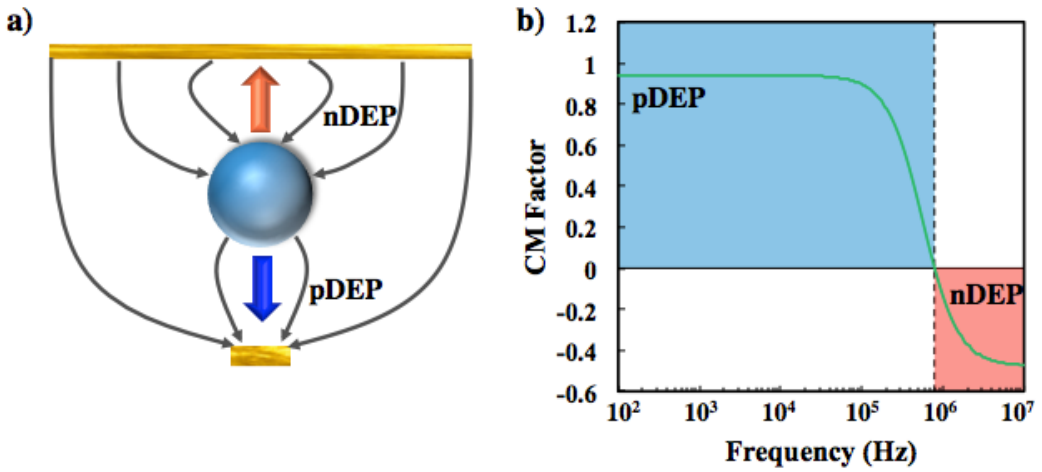

Figure 1.4. a) Schematic illustration of the movement of a spherical particle within a non-uniform electric field. b) Typical CM factor curve as a function of frequency. Regions in blue and red correspond to frequencies in which the particle experiences pDEP, and nDEP, respectively.

The CM factor determines whether the particle will be attracted to or repulsed by regions with large electric field gradients (Fig. 1.4).[76] A positive CM factor will induce positive DEP (pDEP) on the particle, and migration of the particle towards regions with large electric field

gradients. Conversely, a negative CM factor causes the particle to experience negative DEP (nDEP), and subsequent movement towards regions in the electric field where the gradient is at a minimum. Regions with high electric field gradients occur where there are abrupt changes in the local dielectric environment such as the electrode edge,[77] and thus the electrode arrangement is critically important to the performance of the device.[76]

1.5 Objectives and Goals

The overall goal of this work is to explore the incorporation of new plasmonic nanostructures, electrode configurations, and microfluidic approaches in plasmonic-based bacterial biosensors. The objectives of this research include:

1. Fundamentally understand the plasmonic modes of nanohole arrays in symmetric and asymmetrical dielectric environments, fabricate the newly developed devices through nanofabrication techniques, and test the SERS response of surface-bound and aqueous phase small molecules as a function of dielectric symmetry and distance from the nanohole arrays;
2. Study the mass transport effects of bacterial cells under diffusion-limited and DEP-enhanced regimes to lower the limit of detection and detection time in microfluidic SERS biosensors, and understand how application of DEP affects the bacterial SERS spectra;
3. Incorporate DEP electrodes into an SPR microfluidic device to enable sensitive, rapid, and selective detection of bacterial targets.

This thesis summarizes work conducted to reduce the readout time and limit of detection of SERS and SPR-based biosensors through plasmonic manipulation, and integration of DEP in microfluidic devices. Chapter 2 reviews finite-difference time-domain simulations of nanohole arrays embedded in asymmetrical and symmetrical dielectric environments to optimize SERS substrates, and understand the dielectric and geometric properties necessary to generate electric

field extension. Chapter 3 is an overview of the nanofabrication routes explored to resolve the optimized structures from Chapter 2. These processes include focused ion beam milling, electron beam lithography followed by gold etching, soft lithography followed by contact printing, and soft lithography followed by solvent-assisted molding. Solvent-assisted molding was found to be the most robust method, which allowed generation of highly uniform, large-area nanohole arrays. The SERS response of surface bound and aqueous phase small molecules are also presented in Chapter 3, which are in good agreement with the simulated plasmonic properties presented in Chapter 2.

The second half of the thesis, Chapters 4 – 6, focuses on the integration of DEP into SERS and SPR microfluidic devices. Chapter 4 describes the development of a SERS biosensor containing a dually functional electrode that is both DEP and SERS-active. The biosensor successfully trapped 2 μm polystyrene microparticles and *E. coli* cells in a 10^5 CFU/mL suspension. Furthermore, the effect of the external DEP field on the cellular structure was investigated. Over an applied frequency range of 500 Hz – 10 MHz, no change in the SERS spectra of Gram-positive and Gram-negative bacteria were observed. Chapter 5 reviews the development of dually functional interdigitated electrodes that sustain SPR, while enabling increased bacterial mass transport with DEP. The DEP-SPR strategy led to an improved limit of detection for *E. coli* of 3 x 10^2 CFU/mL, and selective detection over non-target bacteria with secondary antibody amplification. Chapter 6 expands upon the DEP-SERS work presented in Chapter 4, and focuses on future work to simultaneously separate and identify bacterial mixtures utilizing the DEP-SERS device. Finally, Chapter 7 reviews the main conclusions of the work, and gives an outlook for potential directions in which the work can be taken.

Chapter 2. FINITE-DIFFERENCE TIME-DOMAIN (FDTD) SIMULATIONS OF PLAMONIC NANOHOLE ARRAYS (NHAS) IN SYMMETRIC AND ASYMMETRIC DIELECTRIC ENVIRONMENTS

2.1 INTRODUCTION

Finite-difference time-domain (FDTD) simulations are used to study the optical response of an arbitrary structure to an external electromagnetic field.[78] Numerical methods are employed to solve curl of the steady-state Maxwell's Equations (SSME) within the FDTD simulation region. FDTD calculations are capable of simulating structures with a wide range of characteristic lengths from tens of meters to nanoscale dimensions. Plasmonic structures often contain length scales in the 10^{-6} – 10^{-9} m range, and can have complex geometries involving nanoscale apertures, arrays, or particle ensembles. Therefore, the simulation region is deconstructed into finite cells with sub-wavelength resolution, and the SSME are solved within each cell to give the optical response.

The Yee cell is the core construct used in most FDTD simulations.[79] In Cartesian coordinates, each Yee cell exists as a cubic cell that contains the electric and magnetic vector components (E_x, E_y, E_z, H_x, H_y, and H_z). Vector components are arranged such that magnetic components are centered on cubic faces, with electric components placed on the vertices. Conveniently, this vector arrangement effectively implements the integral form of the Faraday's and Ampere's Laws, which are essential components of the SSME. A central difference time

stepping algorithm is employed such that the new value of any given field component is only a function of its previous value and the previous value of adjacent unit cells. Because the electric and magnetic field components of entire simulation region are assumed to be zero at time-zero, construction of the FDTD region into Yee cells provides an effective route to the steady state electromagnetic field distributions and scattering profiles of plasmonic materials.

Electromagnetic field distributions and scattering profiles are essential to the design and fundamental understanding of plasmonic materials for SERS-based biosensing. The performance of SERS nanomaterials is primarily affected by LSPR generation, both in magnitude of the amplified electric field and in the wavelength at which the LSPR occurs.[34, 80] Therefore, FDTD simulations provide an effective route to design the SERS enhancing nanostructures prior to fabrication. SERS-active nanoparticles and nanostructured arrays have been designed with the FDTD method to tune geometric parameters for an optimized optical response. While simple structures such as homogenous nanoparticles or nanohole arrays have been simulated,[81] more complicated structures such as encapsulated and cores-shell nanoparticles[82] and quasi 3-dimension plasmonic nanostructured arrays[83] have been studied with FDTD simulations. These works demonstrate the wide range of capabilities FDTD simulations provide for the design and fundamental understanding of SERS-active nanostructures.

Furthermore, FDTD simulations have been used to fundamentally study the LR-SPR mode.[54] As described in Section 1.4, the unique LR-SPR mode is generated by transplasmon coupling on the opposite interfaces of metal films embedded in symmetrical dielectric environments. Generation of the LR-SPR mode provides beneficial electric field characteristics; the primary of which is a sustained intensity at further distances from the SERS enhancing nanostructure, which can be incorporated into SERS-based biosensors. The LR-SPR mode was

generated in the Kretschmann configuration on an ultrathin Ag film (~20 nm) embedded in a symmetrical environment.[53] The sensing system was made SERS-active by addition of Ag nanoparticles. FDTD simulations were used to study interactions between the Ag nanoparticles and symmetrically embedded film, and characterize the associated electric field distribution and scattering of the film.[54] The structure was compared to a control setup containing an Ag film in an asymmetrical dielectric environment. LR-SPR generation on the symmetrical Ag film resulted in an amplified field intensity ~3.8 times larger that the asymmetrical case.[54]

In this work, FDTD simulations were used to investigate the plasmonic response of SERS-active nanohole arrays (NHAs) in symmetrical and asymmetrical dielectric environments. We systematically investigated the resonant modes and electric field distributions of 2-dimensional, square-lattice NHAs of ultrathin gold films in three classes of layered substrates immersed an aqueous background. Conventional and pseudo long-range (PLR) substrates were used to study the response of the NHAs in asymmetrical and symmetrical dielectric conditions, respectively. A 'resonant mirror' was inserted between the glass/Cytop interface in PLR substrates to induce strong constructive interference on the surface of gold NHAs due to the formation of Fabry-Pérot optical cavity between the resonant mirror and NHA. The tri-layered, Fabry-Pérot containing structure is referred as the 'long-range' (LR) class of substrates. Optical and geometrical parameters were varied, and electric field extension was observed in the LR substrates.

2.2 Simulation Configuration

2.2.1 *Classifications of Simulated Devices*

NHAs were chosen as the SERS-active plasmonic nanomaterial to investigate the plasmonic response in asymmetric and symmetric dielectric environments. Compared to other

nanostructured arrays, NHAs offer a simplified geometry void of sharp edges that can complicate both the simulation setup and fabrication process. For all simulated structures, the plasmonically active Au film was fixed at 20 nm. Three distinct classes of NHAs were investigated in this work: conventional, pseudo long-range (PLR), and long-range (LR). The conventional structures were comprised of an Au NHA directly on a glass substrate (Fig. 2.1a). Conventional structures provided the baseline for the asymmetrical dielectric case, and enabled relative comparison of the electric field distributions and resonant wavelengths of the PLR and LR structures.

PLR structures were used to study the plasmonic response of the Au NHAs in symmetrical dielectric environments. PLR structures contained an interstitial Cytop layer between the Au NHA and glass substrate (Fig. 2.1b). Cytop has a refractive index in the visible range of n = 1.34, and was used to satisfy the symmetrical dielectric condition necessary for LR-SPR generation. Previous studies conducted on LR-SPR substrates demonstrated that leakage of light through the substrate could reduce both the efficiency of plasmon generation at the Au/H_2O interface, and the penetration depth of the evanescent field above the Au/H_2O interface.[44] To combat the light leakage, an optically opaque 'resonant mirror' was placed between the glass substrate and Cytop film to effectively prohibit light from passing through the substrate. The tri-layered, plasmonic architecture formed the basis of the LR structures (Fig. 2.1c).

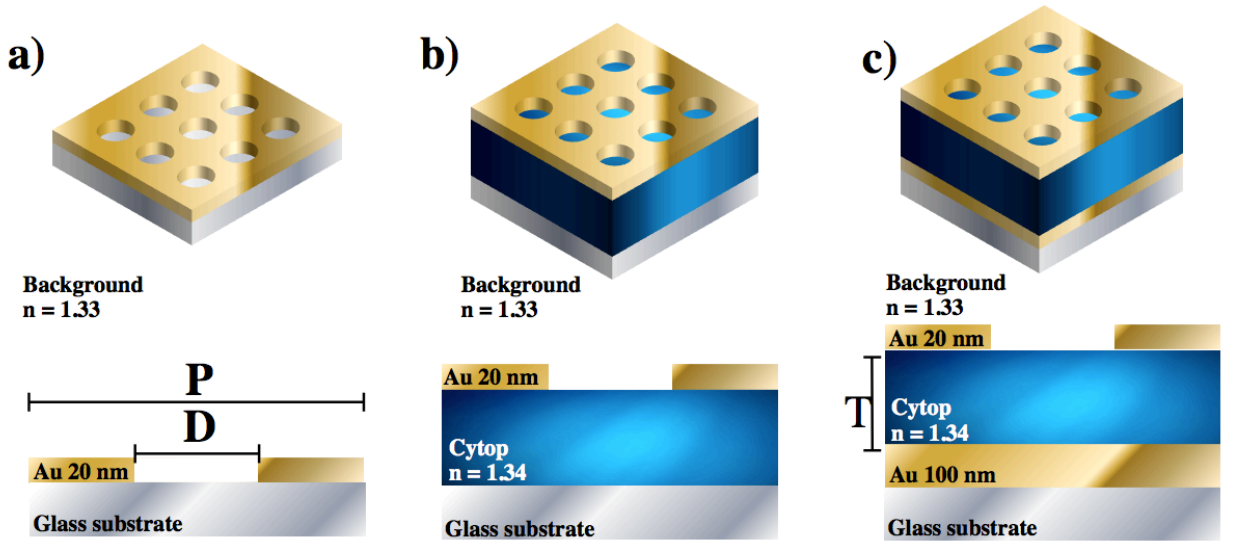

Figure 2.1. Perspective and unit cell schematics of the a) conventional, b) PLR, and c) LR structures.

The Cytop thicknesses of the PLR and LR structures and the nanohole diameter were varied to determine the optimal condition to most effectively generate LR-SPR. Theoretical calculations were used to predict the required pitch to generate LR-SPR on the NHAs, which was fixed throughout the simulations. Single nanoholes and arrays of nanoholes can act as point sources for the excitation of LSPR.[81] The theoretical pitch necessary to generate LSPR with light at normal incidence to a 2-D grating coupler can be predicted by:[84]

$$\frac{\lambda}{P}\sqrt{m_x^2+m_y^2} = \mathrm{Re}\left\{\sqrt{\frac{\varepsilon_d\,\varepsilon_m}{\varepsilon_d+\varepsilon_m}}\right\}+\Delta n_{ef} \qquad \text{Eq. 2.1}$$

where P is the pitch of neighboring nanostructures, m_x and m_y are integers corresponding to grating orders of the diffracted light, λ is the resonant wavelength of a surface plasmon, ε_d and ε_m are the relative permittivities of the surrounding dielectric medium and metal, respectively, and Δn_{ef} accounts for the difference in the propagation of the surface plasmon on a planar film relative to the grating. Additionally, Δn_{ef} accounts for the differences in the phase constants of single-interface (asymmetric) and long-range (symmetric) surface plasmons. It is commonly accepted that the optimal wavelength of LSPR (λ_{LSPR}) for SERS substrates exhibiting a

Lorentzian-shaped LSPR peak can be described by: $\lambda_{LSPR} = ½(\lambda_{RS} + \lambda_{Ex})$, where λ_{RS} and λ_{Ex} are the wavelengths of the Raman scattered photons and excitation source, respectively.[80] The validity of this equation holds for LSPRs that overlap with the wavelength of the Raman scattered photons, and the wavelength of excitation. Generally, this holds true so long as the three wavelengths of interest fall within a ~120 nm window of one another.[80] In this work, a 785 nm near infrared laser was used as an excitation source, and Raman shifted photons were collected in the range of 300 – 1800 cm^{-1}. Therefore, λ_{LSPR} should be tuned within the spectral window of 794 – 849 nm for the optimal SERS response. For this work, λ_{LSPR} = 800 nm was selected in order to determine the NHA pitch. Using Eq. 2.1, a pitch of 604 nm was predicted for a 20 nm Au film perforated with a 2-D NHA immersed in an aqueous medium (n_d = 1.33). Values for the relative permittivity of gold[85] and Δn_{ef}[84] were taken from the literature.

2.2.2 *Optical Properties of Materials*

The accuracy of FDTD calculations is highly dependent on the proper definition of the optical properties (i.e. refractive indexes, dielectric functions) of the materials used in the simulations. For non-dispersive materials such as DI H_2O, glass, and Cytop, a constant value can be assumed over the entire wavelength range. For all structures the simulated in this work values of n = 1.33 and 1.51 were assigned to the aqueous background and glass substrate, respectively. Ellipsiometery was used to measure the refractive index of Cytop, which has held constant at n = 1.34.

For dispersive materials such as Au, the index of refraction is wavelength dependent and complex, as described by $\bar{n} = n + i\kappa$, where $\bar{n}$ is the complex refractive index, n is the phase velocity, and κ is the extinction coefficient.[86] The phase velocities and extinction coefficients

for Au were taken from Johnson and Christy.[85] A multi coefficient model was used to fit the discrete n and k data, with a good fit in the simulated wavelength region of 700 – 950 nm.

2.2.3 *Definition of Simulation Region*

Cartesian coordinates defined the three dimensional simulation regions. Structures were oriented such that the NHAs were normal to the z-direction. Therefore, the span of the x and y directions were fixed at 604 nm in accordance with the pitch calculated from Eq. 2.1. Because the structures contained differing layers and layer thicknesses, the length of the simulation region in the z-direction changed from structure to structure. However, the distance from the NHA/H_2O interface to the positive z boundary was fixed at 500 nm to maintain consistency between the different classes of structures. In the negative z-direction, a 100 nm gap was maintained between the simulation boundary and the glass/NHA, glass/Cytop and glass/Au for the conventional, PLR, and LR structures, respectively.

FDTD boundary conditions and mesh refinement are necessary to ensure the scattered and injected electromagnetic energy can leave the simulation region without introducing interference.[79] A plane wave source light source in the wavelength range of 700 – 950 nm was injected at a distance of 400 nm from the NHA/H_2O interface, with the electric component polarized in the x-direction. Anti-symmetric and symmetric boundary conditions in the x and y directions, respectively, were used to take advantage of the two-fold symmetry of the structures. The perfectly matched layer (PML) boundary condition was used for both the positive and negative z boundaries. Mesh refinement was added around the nanostructures to account for abrupt changes in the local dielectric environment. The mesh refinement was 2 nm in all spatial directions, and spanned the entire xy plane and extended 50 nm from the NHA interfaces in the z-direction.

2.2.4 *Reflectance and Electric Field Monitors*

Reflectance and electric field monitors were added to the simulation region to obtain scattering spectra and steady-state electric field distributions, respectively. The reflectance monitors were placed 50 nm above the plane wave source. Reflectance monitors were normalized to the injected source, and gave insight into the wavelengths at which the discrete LSPR modes occur. Electric field monitors were placed at the NHA/H_2O interface, and at distances of 5, 10, 25, and 50 nm above the NHA/H_2O interface.

2.3 RESULTS AND DISCUSSIONS

FDTD simulations were carried out to investigate the resonant modes and electric field distributions of the three classes of plasmonic nanostructures. The three classes were characterized by the location of the LSPRs and the associated electric field enhancements. The intensity of the SERS signal (I_{SERS}) is directly related to the electromagnetic enhancement factor (EF_{EM}) through contributions of the amplified electric fields at the laser excitation frequency, and the frequency of the Raman shifted photons:[34]

$$I_{SERS} \propto EF_{EM} = \left|\frac{E(\omega_{Ex})}{E_0(\omega_{Ex})}\right|^2 \left|\frac{E(\omega_{RS})}{E_0(\omega_{RS})}\right|^2 \quad \text{Eq. 2.2}$$

where $E(\omega_{Ex})$ and $E(\omega_{RS})$ are the electric field intensities at the Au/H_2O interface at the laser excitation frequency, ω_{Ex}, and the Raman scattering frequency, ω_{RS}, respectively, $E_0(\omega_{Ex})$ and $E_0(\omega_{RS})$ are the incident light electric fields at ω_{Ex} and ω_{RS}, respectively,

To quantify the additional contributions of all inelastically scattered photons interacting with the plasmonic nanostructure, a quality factor (Q_F) was adapted from *Blaber et. al*.[87] The Q_F used in this work is defined as:

$$Q_F = \frac{1}{\beta} \int_{\omega_{RS}^{min}}^{\omega_{RS}^{max}} \left|\frac{E(\omega_{Ex})}{E_0(\omega_{Ex})}\right|^2 \left|\frac{E(\omega_{RS})}{E_0(\omega_{RS})}\right|^2 d\omega_{RS} \quad \text{Eq. 2.3}$$

where ω_{RS}^{min} and ω_{RS}^{max} correspond to the range of Raman shifted frequencies under investigation (300 – 1,800 cm^{-1}), and β is a normalization constant defined as $\beta \equiv \omega_{RS}^{max} - \omega_{RS}^{min}$.

2.3.1 *Conventional Structures*

In the conventional structure, the 2-D square lattice, diameter, and gold film thickness were fixed at 604, 150, and 20 nm, respectively, for the entirety of the simulations. Two resonant modes were observed at 712 and 892 nm for the conventional substrate as shown in the reflectance spectrum in Fig. 2.2a, which correspond to the propagating mode (P-mode) and localized mode (L-mode), respectively. Mode assignment was determined by the properties of the z-component of the electric field distribution (E_z) shown in Fig. 2.2b and c. The E_z polarity oscillation propagated along the two interfaces throughout the entire unit cell for the P-mode (Fig. 2.2b), while the oscillation was completely confined to the nanohole edges for the L-mode (Fig. 2.2c).

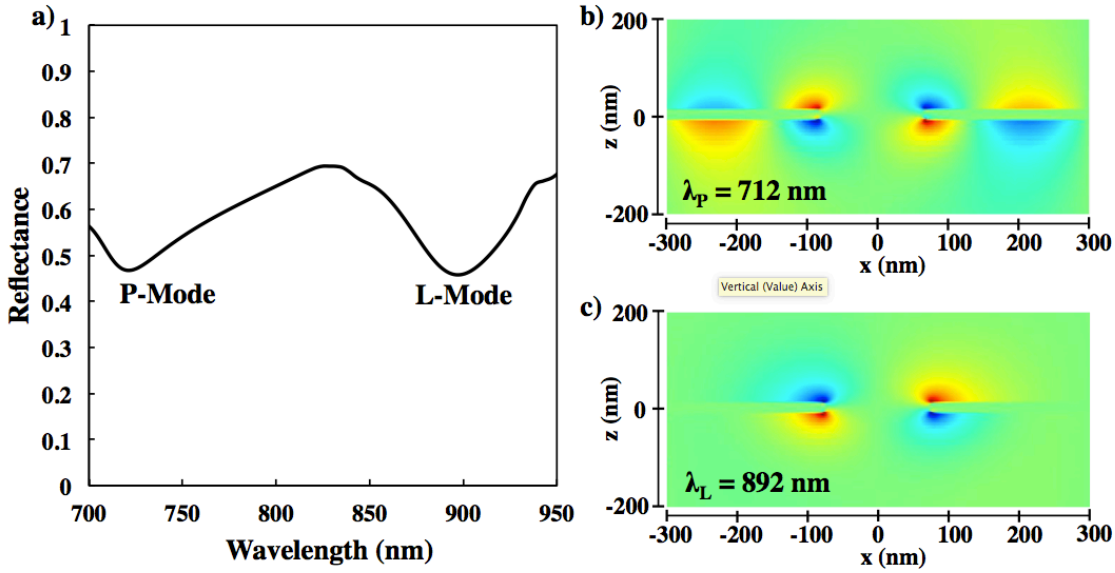

Figure 2.2. a) FDTD results for the reflectance spectra of the conventional structure that displayed two distinct resonances modes: the propagating mode (P-Mode), and localized mode (L-Mode). The E_z component of the electric field distribution for the b) P-Mode and c) L-Mode.

The two modes exhibited similar maximum electric field intensities of $|E_{max}/E_0|^2$ = ~2.1 x 10^2 at the Au/H_2O interface (Fig. 2.3a). Both resonance modes lie outside of the optimal range for SERS enhancement,[80] with the P-Mode blueshifted by 82 nm and the L-Mode redshifted by 43 nm outside of the desired range. Therefore, the L-Mode of the conventional structure was used as the baseline for which to compare the PLR and LR structures. The cross-sectional total electric field ($E_x^2 + E_y^2 + E_z^2$) distribution of the L-mode shows confinement of the electric fields at the nanohole edges (Fig. 2.3b).

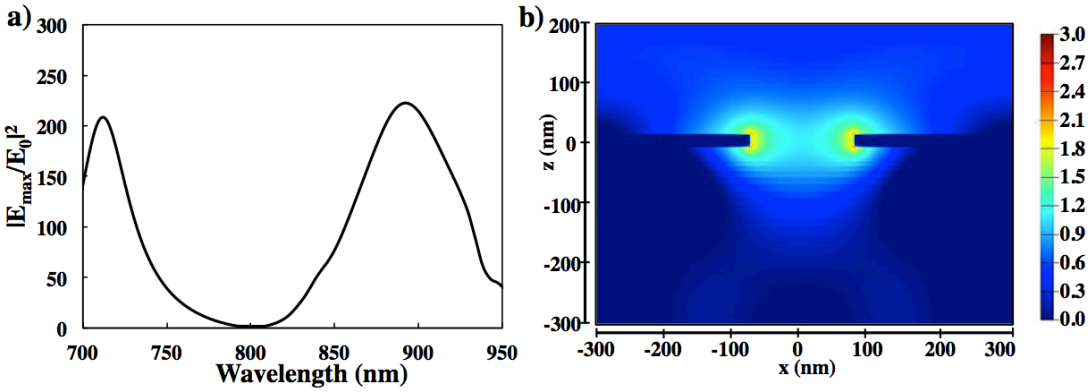

Figure 2.3. a) Maximum electric field intensity at the Au/H2O interface. b) Cross-sectional view (XZ plane) of the electric field distribution of the L-Mode. The scale bar represents $|E_{max}/E_0|^2$ on a log scale.

2.3.2 *Pseudo Long-Range Structures*

A refractive index-matched Cytop layer was inserted between the Au NHA film and glass substrate to incrementally change the dielectric environment surrounding the Au NHA from asymmetric to symmetric. It was expected that the resonances are dependent on the Cytop thickness. Therefore, the Cytop thickness of the interstitial layer was varied from 50 to 100, 250, and 500 nm. The reflectance spectra in Fig. 2.4a shows the L-mode blueshifted from 822 to 808 nm for Cytop thicknesses of 50 and 500 nm, respectively, while the P-mode blueshifted outside of the 700 nm spectral window minimum. Additionally, the L-mode generated by the PLR substrates exhibited a narrower reflectance dip compared to the L-mode of the conventional

substrate. The L-mode is comprised of two peaks, a strong peak, and slightly redshifted shoulder mode. The shoulder mode is much more pronounced for thinner Cytop films, and the two modes coalesced as the Cytop thickness was increased. The E_z distributions of the PLR substrates with these four Cytop thicknesses displayed the same confinement at the nanohole edges (Figs. 2.4 b-e), confirming the characteristics of the L-mode.

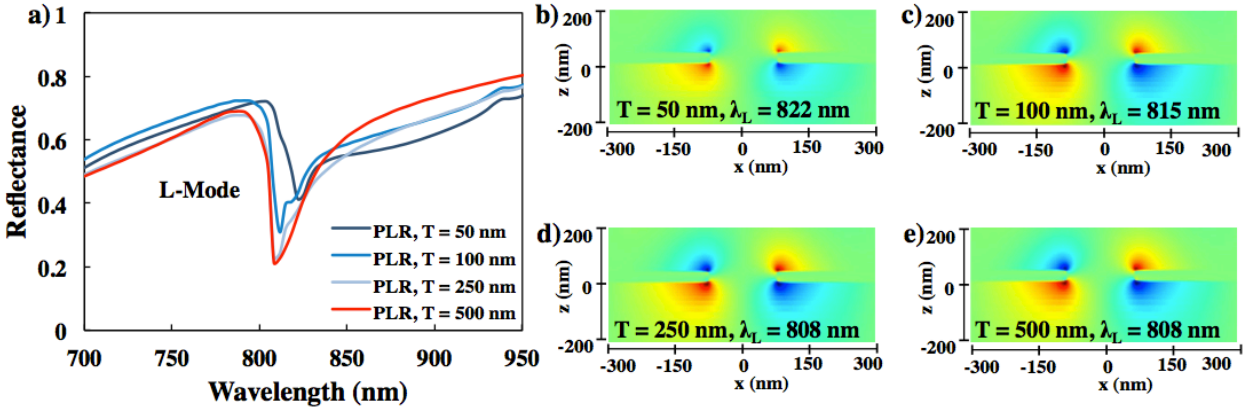

Figure 2.4. a) Reflectance spectra for PLR substrates with Cytop thicknesses of 50, 100, 250, and 500 nm, which show a single resonance mode. The E_z component of the electric field distribution for Cytop thicknesses of b) 50, c) 100, d) 250, and e) 500 nm.

The maximum electric field intensity at the Au/H_2O interface of L-modes increased from $|E_{max}/E_0|^2$ = 4.0 x 10^2, 7.6 x 10^2, 1.1 x 10^3 to 1.3 x 10^3 for Cytop thicknesses of 50, 100, 250 and 500 nm, respectively (Fig. 2.5a). The small increase of the maximum electric field intensity with the increase of the Cytop layer from 250 to 500 nm indicates that the Cytop layer was thick enough to attenuate the glass interference. Figure 2.5b shows the corresponding cross-sectional total electric field distribution of the L-mode for the PLR substrate with a Cytop thickness of 250 nm, indicating a much stronger electric field enhancement through effective plasmon coupling afforded by the symmetrical dielectric environment. For all Cytop thicknesses investigated the electric field distributions were confined to the nanohole edge (data not shown for the thicknesses of 50, 100, and 500 nm).

The Q_F was calculated using the FDTD simulated electric field intensities for the conventional and four PLR substrates, and plotted as a function of Cytop thickness in Fig. 2.5c. The Q_F experienced a sharp increase with respect to Cytop thickness, rising from 4.7 x 10^4 for the conventional substrate to 2.5 x 10^5 and 1.0 x 10^6 for the PLR substrates with 50 and 100 nm Cytop interstitial layers, respectively, and then a slow increase to 3.0 x 10^6 for Cytop thicknesses ≥ 250 nm, consistent with the observation of the surface maximum electric fields in Fig. 2.5b. The plateauing behavior held true for Cytop thicknesses up to 1 μm (data not shown). This, once again, suggests that for Cytop films > 250 nm the NHA can no longer 'feel' the underlying glass substrate, and can be considered embedded in a truly symmetric dielectric environment.

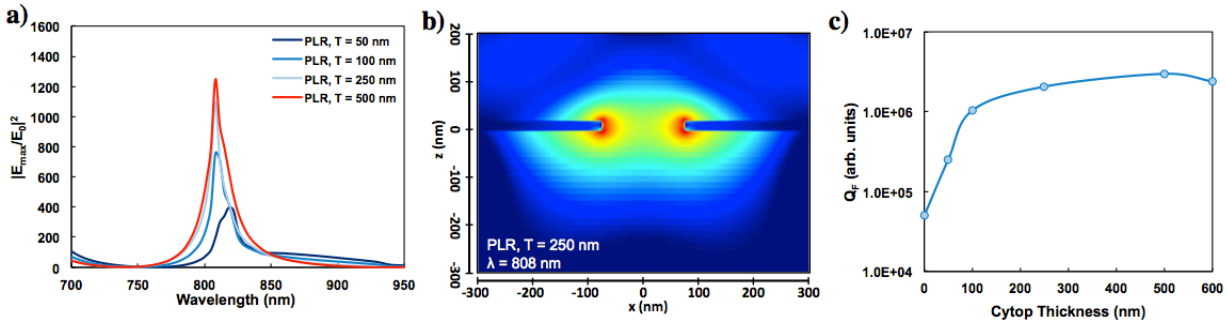

Figure 2.5. a) Maximum electric field intensities at the Au/H_2O interfaces for PLR substrates with Cytop thicknesses of 50, 100, 250, and 500 nm. b) Cross-sectional view (XZ plane) of the electric field distribution of the L-Mode for Cytop thickness of T = 250 nm. c) Quality factor of the PLR substrates.

2.3.3 *Long-Range Structures*

The plasmon resonances and the electric field distributions of LR-SERS substrates were firstly investigated as a function of nanohole diameter, with the Cytop thickness held constant. The thickness for the initial simulations was fixed at 250 nm as it was observed with PLR substrates that this thickness was sufficiently large for the gold NHA to completely decouple from the glass substrate. Figure 2.6 shows the reflectance spectra for three representative diameters (D = 150, 300, and 450 nm) of LR-SERS substrates. Three resonance modes are

observed. The mode around 800 nm is attributed to the localized mode, which is similar to that present in the PLR substrate (T = 250 nm) at λ_L = 808 nm.

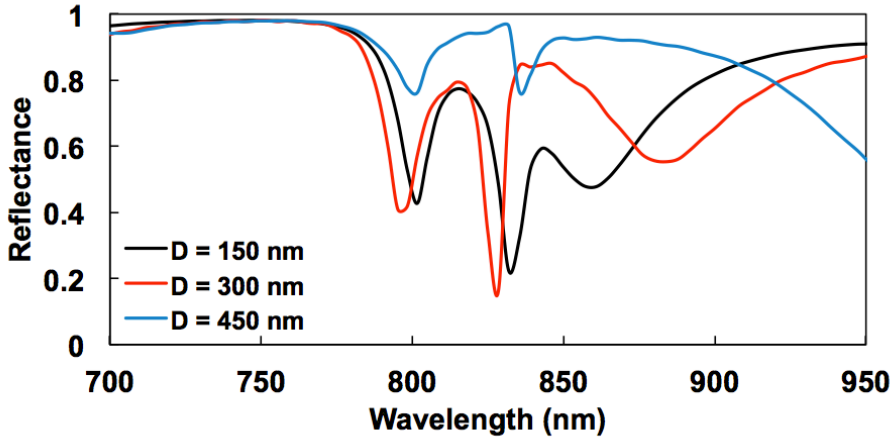

Figure 2.6. FDTD calculated reflectance spectra for LR structures with diameters of 150, 300, and 450 nm, and fixed Cytop thickness of T = 250 nm.

Figures 2.7a-i show the E_z polarity oscillation of the L-mode exhibited strong confinement at the nanohole edges, as observed for the conventional (Fig. 2.2c) and PLR substrates (Figs. 2.4 b-e). This L-mode was unaffected by the underlying gold film and independent of diameter. Additionally, two new modes are generated and attributed to the first and second order coupling between the gold NHAs and underlying gold film, which are termed C_I and C_{II}, respectively. The first order coupling can be seen in the E_z distributions (Figs. 2.7d-f). Polarity oscillation occurs not only laterally, but also vertically between the NHA and resonant mirror. For D = 300 nm, an in-phase oscillation is observed (Fig. 2.7e), whereas for D = 150 and 450 nm an out-of-phase oscillation is observed (Figs. 2.7d and f). Similar to the L-mode, the resonance wavelength of the first order coupled mode remained largely invariant with respect to diameter. The second order coupling displayed a similar coupling pattern to the first order mode (Figs. 2.7g-i). However, the resonance wavelength redshifted as the diameter was increased (Fig. 2.6).

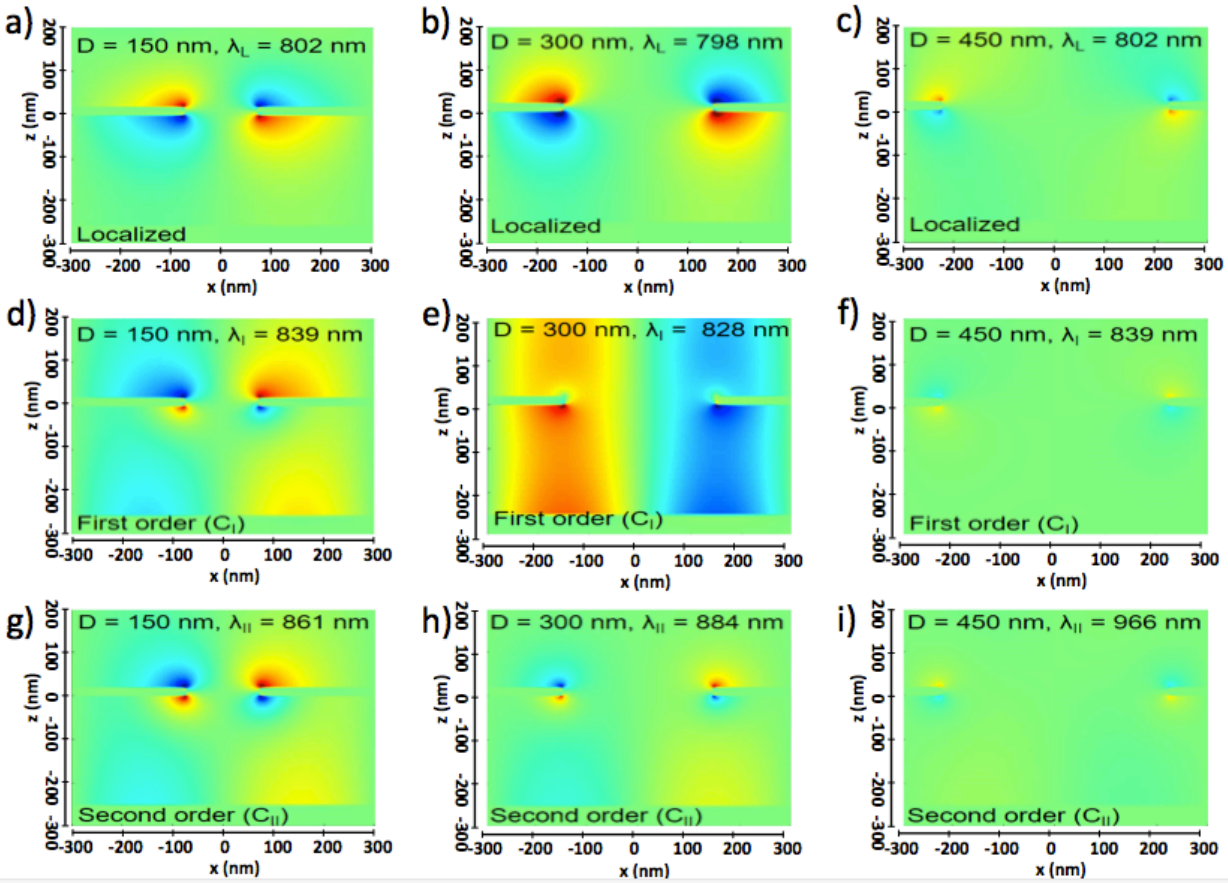

Figure 2.7. The E_z components for LR structures with diameters of 150, 300, and 450 nm, and fixed Cytop thickness of T = 250 nm.

Figure 2.8 shows $|E_{max}/E_0|^2$ at the Au/H_2O interface as a function of wavelength for the three substrates. With respect to the localized mode, $|E_{max}/E_0|^2$ at the Au/H_2O interface increased as the diameter was increased from 150 to 300 nm, and then decreased as the diameter was further increased to 450 nm. A maximum intensity of $|E_{max}/E_0|^2 = 1.51 \times 10^3$ for D = 300 nm was observed, while values of $|E_{max}/E_0|^2 = 1.11 \times 10^3$ and 7.43×10^2 were observed for diameters of 150 nm and 450 nm, respectively. Both coupled modes exhibited a decrease in $|E_{max}/E_0|^2$ as the diameter was increased. For a fixed diameter however, the coupled modes exhibited similar intensities.

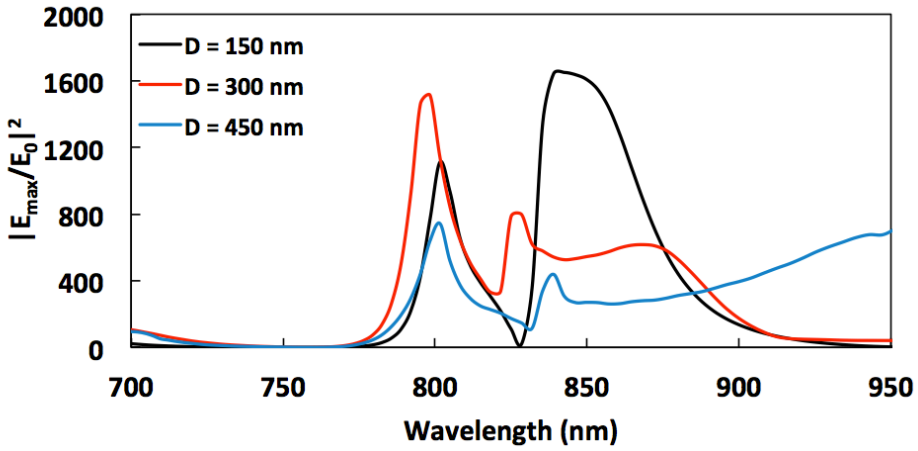

Figure 2.8. Maximum electric field intensities at the Au/H_2O interfaces for LR structures with diameters of 150, 300, and 450 nm, and fixed Cytop thickness of T = 250 nm.

Inspection of the cross-sectional total electric field profiles for the three modes can provide insight into the plasmonic nature of LR-SERS substrates, and how they can be tuned for optimal SERS based detection. Figures 2.9a-c show that the excitation of the L-mode produced two distinct hot-spots at the edges of the nanoholes, and negligible electric field density was located in the optical cavity between the NHA and resonant mirror. Intuitively, as the diameter was made larger, the two hot-spots became decoupled in the L-mode due to increased separation distance. Figures 2.9d-f show that the C_I-mode exhibited greater electric field density located in the optical cavity due to increased coupling between the NHA and underlying gold film. A smaller diameter (D = 150 nm) resulted in strong electric field localization above the Au/H_2O interface (Fig. 2.9d). With increased diameter (D = 300 and 450 nm), the electric field localization shifted below the Au/Cytop interface (Figs. 2.9e and f). The C_{II}-Mode exhibited the inverse behavior compared to the C_I-Mode, with electric field density localizing to the interstitial cavity as the diameter decreased (Figs. 2.9g-i). The highest $|E_{max}/E_0|^2$ value at the Au/H_2O interface was obtained for the case of D = 150 nm. Therefore, to further investigate the plasmonic response of LR-SERS substrates, the diameter was fixed at D = 150 nm, and the thickness of the Fabry-Pérot optical cavity on the plasmonic response was explored.

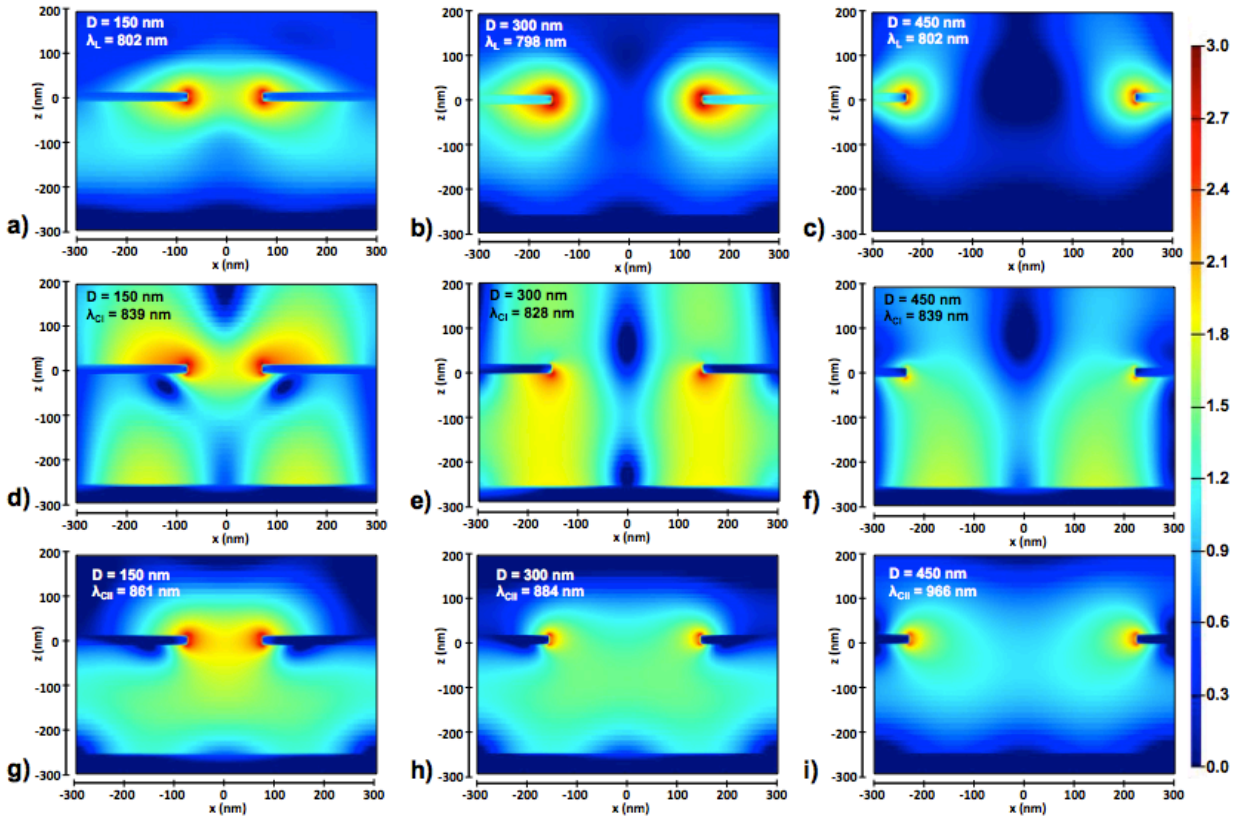

Figure 2.9. Electric field distributions for LR structures with diameters of 150, 300, and 450 nm, and fixed Cytop thickness of T = 250 nm for a-c) the localized mode (L-mode), d-e) coupled mode I (C_I), and g-i) coupled mode II (C_{II}) in the x-z plane. The scale bar represents $|E_{max}/E_0|^2$ on a log scale.

It is well known that the separation distance between two metal films in a Fabry-Pérot optical cavity can have profound effects on the resonant modes and the electric field distributions of plasmonic nanostructures.[88-91] Cytop thicknesses were varied from 50 to 500 nm by 50 nm increments and the Q_F was calculated from FDTD simulated electric field intensities at the Au/H_2O interface (d = 0 nm) and at d = 50 nm above the Au/H_2O interface. The plasmonic sensitivity to the cavity depth becomes apparent when comparing the Q_F as a function of Cytop thickness (Fig. 2.10a). The Q_F sharply increased as the Cytop film was increased from 50 nm to 200 nm, where the Q_F exhibits its maximum value. A local minimum was reached at T = 350 nm with a gradual increase in the Q_F as the Cytop film was further increased to 500 nm. The same oscillatory trend of the Q_F was observed at d = 50 nm, with a corresponding drop of

approximately two orders of magnitude in the Q_F. A detailed analysis was carried out on three representative thicknesses (T = 50, 200, and 350 nm) which encompassed the global maximum and minima in the Q_F at d = 0 and 50 nm.

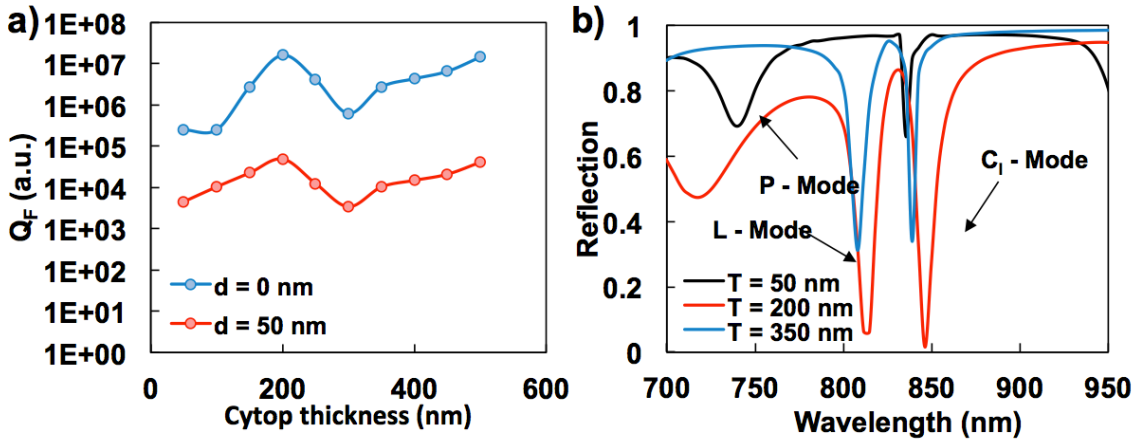

Figure 2.10. a) The Quality Factor (Q_F) was a function of Cytop thickness calculated at the Au/H2O interface and a distance of d= 50 nm above the interface. b) Reflectance spectra for LR structures with Cytop thicknesses of 50, 200, and 350 nm, and fixed diameter of 150 nm.

Figure 2.10b shows the reflectance spectra of LR-SERS substrates with Cytop thicknesses of T = 50, 200, and 350 nm. Two resonant modes are generated at 741 and 835 nm for T = 50 nm. The E_z distribution of the mode at 741 nm shown in Fig. 2.11a clearly displays the characteristics of the P-mode that was observed for the conventional and PLR substrates at shorter wavelengths. Although no L-mode was observed due to the shallow optical cavity, the first order coupled mode (C_I) appeared at λ_{CI} = 835 nm, which can be confirmed by the characteristics shown in the E_z distribution in Fig. 2.11d. As the Cytop thickness was increased to 200 nm, the L and C_I modes redshifted to λ_L = 811 nm and λ_{CI} = 846 nm, respectively, while the P-mode blueshifted to λ_P = 720 nm. The E_z distributions of the modes at 811 and 846 nm shown in Figs. 2.11b and e exhibited the characteristics of the L and C_I modes, respectively. The E_z distribution of the P-mode is not shown. As the Cytop thickness was further increased to 350 nm, both the L and C_I modes exhibited blueshifted resonances to λ_L = 808 nm and λ_{CI} = 839 nm,

respectively (Figs. 2.11c and f). The P-mode further blueshifted out of the spectral range governed by Eq. 1.2.

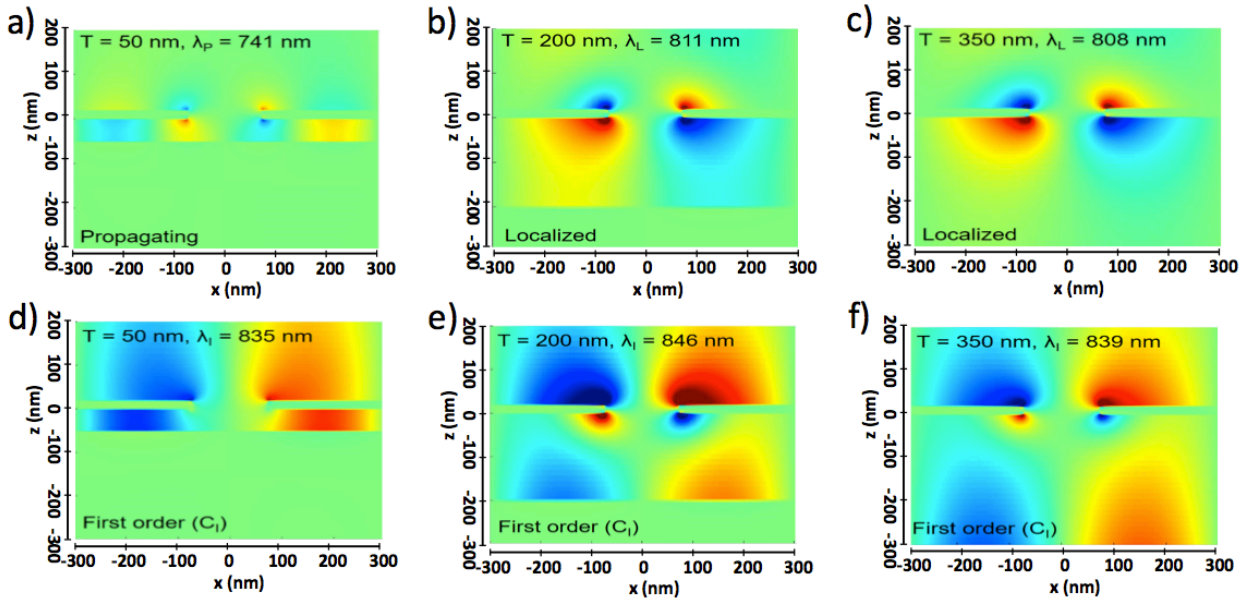

Figure 2.11. The E_z components for LR structures with fixed 150 nm diameters, and Cytop thicknesses of 50, 200, and 350 nm showing the a) propagating mode (P-Mode), b-c) localized mode (L-Mode), and d-f) first order coupled mode (C_I).

The complementary $|E_{max}/E_0|^2$ at the Au/H_2O interface for the three thicknesses are shown in Fig. 2.12. With T = 50 nm, both the P and C_I modes produced very weak intensities. Since the P-mode is out of the lower integral limit of Eq. 1.2, this mode does not contribute to the Q_F, nor the SERS signal. The substrates with thicker Cytop layers showed comparable values of $|E_{max}/E_0|^2 = 1.97 \times 10^3$ and 1.67×10^3 generated by the localized mode for T = 200 and 350 nm, respectively. The C_I-mode showed a drastic increase in $|E_{max}/E_0|^2$ for T = 200 nm with a value of $|E_{max}/E_0|^2 = 4.37 \times 10^3$ compared to $|E_{max}/E_0|^2 = 2.13 \times 10^3$ for T = 350 nm. Since both localized and C_I modes are within the integral limits of Eq. 2.3, the strong electric field makes Q_F a maximum at T = 200 nm (Fig. 2.10a).

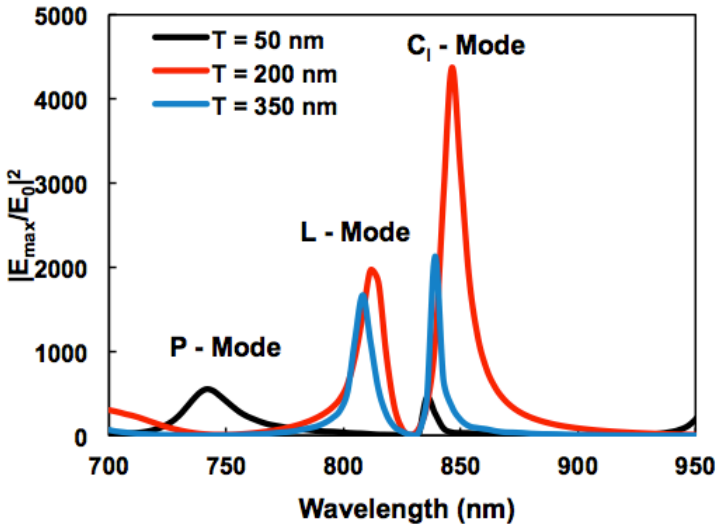

Figure 2.12. Electric field intensity at the Au/H2O interface for LR structures with fixed nanohole diameters of 150 nm, and Cytop thicknesses of 50, 200, and 350 nm.

Again, the cross-sectional electric field distributions are inspected to help elucidate the nature of the field enhancements. In contrast to the conventional and PLR substrates that exhibited the propagating mode bound to the Au/H_2O interface (Figs. 2.2c and 2.4b-e), the propagating mode displayed by the LR-SERS substrate with T = 50 nm showed stronger polarity oscillation bound to the cavity between the NHA and resonant mirror (Fig. 2.11a). Although, polarity oscillation was observed at the Au/H_2O interface for the LR-SERS substrate (T = 50 nm), the intensity of which was weaker than that of the interstitial cavity. Proximity of the NHA to the resonant mirror allowed for increased coupling efficiency, and enhancement of the electric field in the cavity (Fig. 2.13a). With the Cytop thickness increased from T = 200 to 350 nm, the coupling between the NHA and resonant mirror was weakened, and the electric field distribution of the localized mode became more confined to the nanohole edges as shown in Figs. 2.13b and c, respectively. Comparing the electric field distributions of the C_l-mode for the three thicknesses in Figs. 2.13d-f, for T = 200 nm, the electric field was not only strongly enhanced at the Au/H_2O interface as exhibited by $|E_{max}/E_0|^2$ in Fig. 2.13a, but most importantly, the strong

electric field was extended to further distances above the Au/H_2O interface. Therefore, it is expected that the LR-SERS substrate with D = 150 nm and T = 200 nm will yield the long-range behavior.

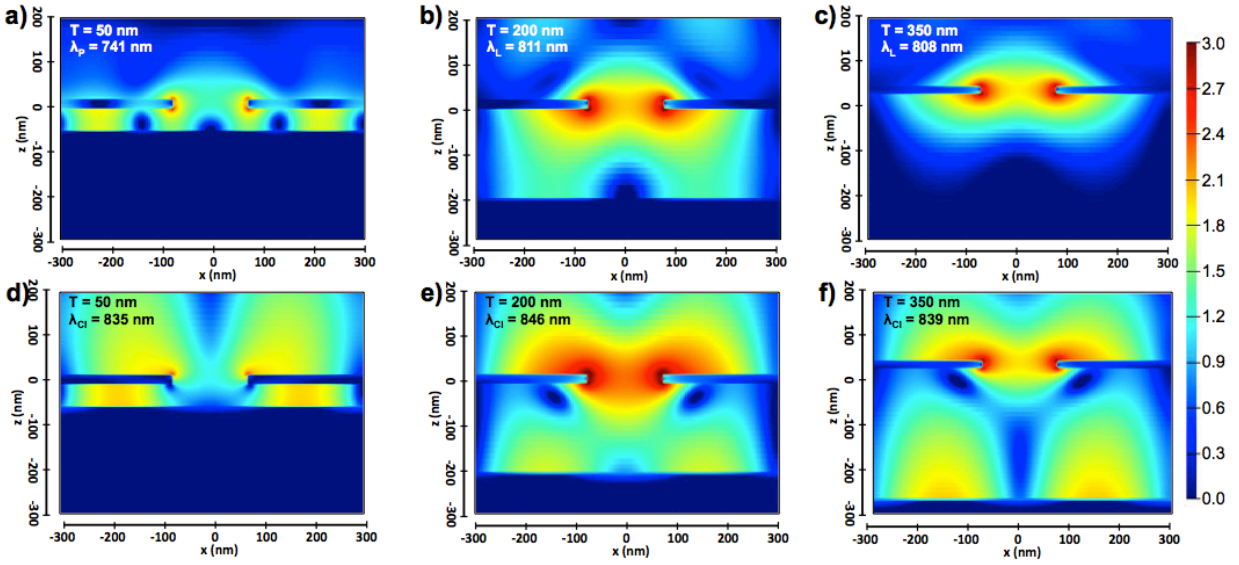

Figure 2.13. The electric field distributions for LR structures with fixed 150 nm diameters, and Cytop thicknesses of 50, 200, and 350 nm showing the a) propagating mode (P-Mode), b-c) localized mode (L-Mode), and d-f) first order coupled mode (C_1).

2.4 CONCLUSIONS

FDTD modeling was performed to investigate the effects of the substrate and geometric parameters of the nanohole arrays in asymmetric and symmetric aqueous, dielectric environments. The electric field distribution and resonant modes were studied as the nanohole array was incrementally separated from the glass substrate by a Cytop layer. Electric field enhancements increased as the nanohole arrays transitioned from the asymmetric to the symmetric condition. Addition of a resonant mirror in between the glass/Cytop interface lead to a further increase in the electric field enhancement. The increase was attributed to the prevention of light leakage through the structure, and induction of coupled modes between the nanohole array and resonant mirror.

Chapter 3. FABRICATION AND CHARACTERIZATION OF NHAS IN SYMMETRIC AND ASYMMERIC DIELECTRIC ENVIRONMENTS

3.1 INTRODUCTION

Effective bacterial biosensing requires stability and reproducibility of the transduction signal regardless of the SERS-active material employed in the biosensor (i.e. nanoparticle or structured surface). Without reproducible signals, quantitative measurements of bacterial suspensions are unfeasible. Signal stability in the SERS biosensor has been a primary driving force in SERS biosensing research, with the overarching goal to develop large-area surfaces reaching a high degree of sensitivity. Numerous fabrication routes and nanostructures have been purposed in both the nanoparticle and structured surface categories to achieve reproducibility in SERS-based biosensors.

Plasmonic nanoparticles, while offering a simple, one-pot synthetic route to SERS-active nanomaterials, have problems with signal stability in bacterial biosensing.[92] Typically, the nanoparticles are composed of Ag or Au, and are in the range of 5 – 80 nm.[93] For homogeneous, spherical nanoparticles, the LSPR is easily controlled by alteration of the nanoparticle diameter.[94] However, the SERS signals generated from nanoparticles can suffer from a lack of reproducibility. Primarily, the fluctuations in the SERS signal are a result of the non-uniform particle distribution in the colloidal solution, or if immobilization is employed, on the planar surface. Irregular particle distribution leads to variance in the local strength of the amplified electric fields (hot-spots), and SERS enhancement factors that are spatially dependent.

Nanohole arrays (NHAs) have well-defined, periodic structures, and therefore eliminate the spatial dependence on the SERS enhancement.[95] The LSPR of NHAs can be altered by controlling the three primary geometric parameters of the array: pitch, diameter, and packing arrangement.[96] The resonance properties of NHAs are complicated due to a complex interplay of localized and propagating plasmons.[81] Therefore, modification of any of the geometric parameters can lead to an LSPR shift and/or change in the strength of the amplified electric fields. The potential for the use of NHAs for biosensing has led to the development of numerous fabrication routes to achieve ordered, large-area arrays.

Recent technological advancements have allowed for the use of top-down nanofabrication routes such as electron beam lithography (EBL) and focused ion beam (FIB) systems to generate high resolution NHAs.[97] FIB systems use low energy ion beams to bombard the sample surface, and through collision remove material from the sample in a direct-write configuration. NHAs were first fabricated by FIB lithography to study the interaction of surface plasmons with the nanoaperatures.[98] Silver films (~200 nm thick) were milled with an FIB system, and resolved NHAs in a square lattice with varied diameters and pitches in the range of 150 nm to 1 μm and 0.6 to 1.8 μm, respectively.

EBL is the electron-based analog of FIB lithography. A focused beam of electrons is impinged upon a photosensitive polymer that decreases (negative photoresist) or increases (positive photoresist) in solubility in the developer solution. Following development and metallization, NHAs can be generated with a high degree of precision. While EBL is fully capable of resolving NHAs with diameters and pitches of less than 100 nm, features as small as ~5 nm have been resolved.[99] However, both electron beam and focused ion beam lithographies require the use of sophisticated equipment in a high vacuum environment, leading to high

costs.[100] Unconventional nanofabrication routes have been developed to mitigate these high costs by partially or completely eliminating the need for the expensive EBL and FIB equipment.

Nanosphere lithography (NSL) can resolve NHAs at low cost with large areas of defect-free domains (~100 μm^2).[101, 102] In NSL, polystyrene nanospheres are immobilized on an appropriate substrate that self-assemble into hexagonal close-packed arrays. The colloidal mask is then exposed to plasma to reduce the diameter of the nanospheres, metal is deposited, and the polystyrene spheres are removed. The resulting NHAs are effective generators of propagating and localized surface plasmons, and can be used as an active surface for biosensing applications. The resonance of the NHAs fabricated by NSL can be tuned by proper selection and etching time of the polystyrene nanoparticles. The benefits of NSL (i.e. low-cost, large-area arrays) are hindered by the inflexibility of hexagonally packed arrays.

Soft lithography represents a balance between the top-down and unconventional fabrication routes to NHAs described thus far.[103] Generally, soft lithography involves casting an elastomeric stamp from a rigid master mold, such as silicon or quartz, which has been patterned by EBL and etching. Because EBL is first used to generate the master mold, soft lithography is not limited to hexagonally arranged NHAs as in NSL. Composite h-PDMS/PDMS replicate stamps are cast from the master, which can achieve nanometer-scale resolution. The replicate stamps can then be metalized to generate plasmonically active nanostructures, or be used to transfer the nanopattern to a secondary resist. Nanoimprint lithography (NIL),[104] nanotransfer lithography,[105] and solvent-assisted molding[106] represent variants of soft lithography to resolve NHAs.

In this chapter, the attempts to resolve NHAs in asymmetrical and symmetrical dielectric environments are described for four distinct nanofabrication routes including: soft lithography of

alkanethiols followed by gold etching, FIB milling of gold films, EBL patterning followed by gold etching, and solvent-assisted nanomolding. The experimental procedures for each process are given in detail. Scanning electron microscopy (SEM) was used to assess the fidelity of the NHAs produced by each fabrication route. Patterning of alkanethiols with subsequent gold etching was found to give the lowest quality NHAs. The mechanism of failure is discussed. FIB milling, EBL followed by gold etching, and solvent-assisted nanomolding were used to successfully produce NHAs. Successful fabrication routes were compared, and solvent-assisted nanomolding provided the most efficient route to high-resolution NHAs.

NHAs fabricated via solvent-assisted nanomolding in asymmetrical and symmetrical dielectric environments were characterized by SERS measurements of surface-bound and aqueous phase analytes. The SERS intensity of 4-mercaptobenzoic acid (4-MBA) was shown to increase by a factor of ~4.7 as the local dielectric environment transitioned from an asymmetrical (conventional structure in Chapter 2) to symmetrical (PLR structure) dielectric environment. Addition of a plasmonic resonant mirror (LR structure) resulted in a further increase by a factor of ~9.8 of the 4-MBA signals by prohibiting leakage of light through the structure. The LR structure was further classified by modifying the local dielectric environment from asymmetrical of the NHA and measuring the SERS signal of 4-MBA. Finally, aqueous phase rhodamine 6G (R6G) was used to compare the distance dependence of the conventional and LR structures. While both structures generated clearly discernable R6G signals at the NHA surface, only the LR structure was able to produce SERS signals of R6G 10 nm above the NHA surface. The plasmonic structures described here represent a new class of SERS-active nanomaterials.

3.2 EXPERIMENTAL

3.2.1 *Plasmonic Nanostructure Fabrication*

Focused Ion Beam Lithography:

Conventional structures were fabricated by focused ion beam (FIB) lithography. Glass substrates were cut into 1 cm x 1 cm chips, and cleaned in a three-stage liquid phase process. The chips were loaded into a Teflon substrate holder and placed in clean 250 mL beaker. The beaker was sequentially filled with the following cleaning solutions: soapy DI H_2O, acetone, and isopropyl alcohol, and placed in a sonicator for 20 min each. The chips were dried in a stream of air, and placed in a UV-O_3 cleaner for 20 min. Gold films, 20 nm in thickness, were deposited on the cleaned glass chips by thermal evaporation. The thermal evaporator (Edwards Auto 306) was evacuated to a chamber pressure of ~2.0 x 10^{-6} mbar before deposition was allowed to occur. Deposition was monitored by a quartz crystal microbalance (QCM), and the film thicknesses were verified with ellipsiometery (JA Wollam), and profilometry (Tencor, Alpha Step 500).

Pristine chips were loaded into the FIB system (FEI XL830). NHAs in a square lattice were written using the PS Convert software to have approximate diameters and pitches of 300 nm, and 600 nm, respectively. The gallium source was heated, and a 30 kV potential at 2.2 μA accelerated the ion beam. The pattern resolution was optimized by varying the milling current, milling time, and dwell time.

Electron Beam Lithography and Gold Etching:

Electron beam lithography (EBL) followed by gold etching was used to resolve long-range (LR) structures. A 4in Si wafer, coated with ~5 nm of Cr and ~95 nm of Au, was cleaned following the liquid and plasma cleaning process described in the preceding section. A Cytop (Asahi, Tokyo, Japan) film of 310 nm thickness was spun cast on the clean surface. The Cytop-

coated substrate was then placed in an O_2 plasma cleaner for 90 s (Diener, Femto). Ambient air was used as the flow gas at 5 sccm, and used to etch and increase the surface energy of the Cytop film. The activated Cytop-coated substrate was loaded into a thermal evaporator, and a 20 nm Au film was deposited using the same process as described in the previous section.

Poly(methyl methacrylate) (PMMA) was then spun cast on the 20 nm Au film with an approximate thickness of 70 nm, and annealed for 90s on a hot plate set to 180^{o}C. NHAs were directly written into the PMMA film with the JEOL JBX-6300FS EBL system. The NHAs, 604 nm in pitch and 150 nm in diameter in a square lattice, had a total area of 50 μm x 50 μm, and the individual arrays were separated 1 cm in the vertical and horizontal directions. The entire substrate was placed in a 3:1 mixture of methyl isobutyl ketone and isopropyl alcohol to develop the NHAs in the PMMA film.

Exposed gold (i.e. gold uncovered by the PMMA NHA film) was chemically etched following a previously reported method to realize the final LR structures.[107] The etching solution was comprised of 0.1 M potassium thiosulfate ($K_2S_2O_3$), 1.0 M potassium hydroxide (KOH), 0.01 M potassium ferricyanide [$K_3Fe(CN)_6$], and 0.001 M potassium ferrocyanide [$K_4Fe(CN)_6$]. Individual 1 cm x 1 cm chips were cleaved from the original silicon substrate, and completely immersed in the etching solution. The etching time was varied from 5 to 15 min to obtain high resolution NHAs. NHAs were then inspected via SEM.

Solvent-Assisted Molding of NHAs:

Gold NHAs were fabricated using solvent-assisted molding. A silicon master mold with 100 μm x 100 μm nanopillar arrays was fabricated using electron beam lithography and reactive ion etching. The nanopillar arrays were defined by a pitch of 604 nm, height of 150 nm, and diameter of 300 nm. h-PDMS/PDMS composite stamps containing nanoholes were cast from the

silicon master. All substrates were fabricated using the same composite stamp to form the nanostructures.

For the conventional structures, glass substrates (1 cm^2) were sequentially cleaned by ultra-sonication in soapy DI H_2O, DI H_2O, acetone and IPA for 20 min each at 40^o C, and were placed in a UV-O_3 cleaner for 20 min. An adhesion promoter (3-MPTMS) was formed by placing the cleaned substrates in a vacuum desiccator with a drop of 50 µL of 3-MPTMS for 2 hr. A 3% by weight solution of PMMA in anisole was immediately spun cast at 4000 RPM for 40 s, and baked on a hot plate at 180^o C for 90 s to form a uniform film of ~100 nm. A 14 µl drop of acetone was placed on the stamp. The PMMA-coated substrate was then brought into contact with the composite stamp on a hot plate at 60^o C for 5 min to form PMMA nanopillars. To remove residual PMMA between nanopillars, the substrate was then placed in an oxygen plasma cleaner with air as the flowgas for 90 s. It is important to note that both solvent-assisted molding and plasma etching shrink the diameter of the PMMA nanopillars from 300 nm to 150 nm. Finally, 20 nm gold films were thermally evaporated (Edwards Auto306) onto the substrates at a rate of 0.02 nm/s with a base pressure of 2 x 10^{-6} mbar. The fabrication of the conventional substrates was completed by removal of PMMA nanopillars capped with gold nanodisks through a lift-off process consisting of tape striping and rinsing with copious amounts of acetone.

PLR substrates were fabricated by spin coating Cytop films directly onto the cleaned glass substrates and annealing on a hot plate at 100, 150, and 200^o C for 60, 30, and 30 min, respectively. Cytop films were exposed to oxygen plasma for 30 s prior to spinning 3% PMMA in order to increase the surface energy of Cytop to make smooth, strongly adhered PMMA films. The gold NHAs were fabricated following the same steps as described for the conventional substrates

LR substrates were fabricated by firstly forming a 3-MPTMS adhesion promoter on clean glass substrates following the same procedures as with the conventional substrates. An optically opaque gold film (100 nm) was then thermally evaporated. The adhesion robustness of the Au films on the glass substrates was qualitatively assessed by 'Scotch tape' and unltrasonication tests. Control substrates that lacked the 3-MPTMS promoter were found to completely delaminate after both tests, whereas the substrates that contained the 3-MPTMS promoter were found to create stable films that remained adhered to the glass substrates. Cytop was immediately spun cast onto the gold film, and annealed with the same recipe as the PLR substrates. Then, the gold NHAs were fabricated following the same steps as described for the conventional substrates. Fabricated NHAs on conventional, PLR, and LR substrates were characterized using scanning electron microscopy (Sirion XL30, FEI).

Soft Lithography of Alkane Thiols and Gold Etching:

Attempts were made to resolve NHAs via soft lithography and subsequent gold etching. h-PDMS/PDMS composite stamps were cast from the same silicon wafer and process as described in the preceding section. Similarly, 20 nm Au films were prepared on clean glass substrates as previously described. An 18 μL aliquot of a 1 mM ethanolic solution of octadecane thiol was dropped onto the composite stamp, and brought in contact with the 20 nm Au film. The Au film and composite stamp were allowed to remain in contact for 20s. The thiolated Au film was then placed into the gold etching solution that was described earlier.

3.2.2 *SERS Measurements*

SERS Measurements on Conventional and PLR Substrates:

Monolayers of 4-MBA were formed on conventional and PLR substrates. Firstly, substrates were cleaned via UV-O3 exposure for 20 min. 4-MBA was dissolved in a 10%

ethanol:DI H_2O (by volume) solution to a concentration of 1 mM. The conventional and PLR substrates were immersed in the 4-MBA solution for 6 hr, rinsed thoroughly with ethanol and DI H_2O, and dried in air. SERS measurements were immediately conducted. The substrates were immersed in DI H_2O in a home-built Teflon container, and covered with a microscope slide to prevent water evaporation while collecting the SERS spectra. The distance from the NHA surface to the coverslip was ~500 μm. All SERS measurements were carried out using a Renishaw inVia Raman spectroscope connected to a Leica upright DMLM microscope. A 785 nm near-infrared laser was focused with a 50x objective (N.A. 0.8, W.D. 0.5 mm) to form a laser spot size of ~2 μm x 20 μm, which allowed for multiple measurements to be taken from different locations on the nanohole array. The laser power was measured with a handheld laser power meter (Edmund Optics) in the focal plane of the substrates to be 2.4 mW. The acquisition time was set to 10 s and a single accumulation. The raw data was acquired by the Wire 2.0 software (Renishaw). All spectra were analyzed and baseline corrected using MATLAB.

Distance Dependence of LR and Conventional Substrates:

LR and conventional substrates were cleaned by UV-O3 exposure for 20 min. Aqueous solutions of R6G (1 mM) were then dropped on the substrates in 200 μL aliquots, and remained for 30 min to allow R6G adsorption. The R6G solution was then removed from the substrates. The substrates were dried and placed in the Teflon holder. The Teflon holder was then filled with DI H_2O (200 μL), and covered with a microscope slide. SERS spectra of R6G were acquired immediately with a single 10 s accumulation time, using the same setup described in the previous section. Cytop capping layers of ~10 nm were spun cast on freshly fabricated LR and conventional substrates by diluting the stock Cytop solution with CT-180 SOLV in a 20:1 ratio (v:v) at 3,000 RPM for 40 s. All film thicknesses were measured by ellipsometry (α-SE, J.A.

Woollam) and profilometry (Alpha-Step 500, KLA Tencor). R6G (1 mM) was again allowed to adsorb to the surface for 30 min before removal, and subsequent immersion in DI H_2O. SERS spectra were immediately acquired and processed as previously described.

3.3 Results and Discussions

3.3.1 *Comparison of NHA Fabrication Routes*

The optimized NHAs, determined by FDTD simulations (Chapter 2), consisted of 150 nm diameter nanoholes in a square lattice of 604 nm. Large area NHAs of 100 μm x 100 μm were desired for optical and SERS measurements. Attempts to fabricate the NHAs in asymmetrical and symmetrical dielectric environments were conducted using FIB lithography, EBL followed by Au etch, soft lithography followed by contact printing, and soft lithography followed by solvent-assisted molding.

NHAs resolved by FIB lithography suffered from low resolution, film sputtering, and small area arrays. Attempts to optimize the NHAs were focused primarily by controlling the mill time and mill current. The dwell time, which refers to how long the ion beam is focused in a particular location, was set to 50 μs. The mill time is the total time in which the sample is exposed to the ion beam. Increasing the mill time leads to an increase in the number of passes the ion beam makes over the patterned area. Together, the dwell and mill time define how long and at what interval any discretized location in the pattern area will be exposed to the ion beam. The mill current is a measure of the energy of the gallium ions from the source filament when they reach the sample surface. It was hypothesized that fine-tuning the mill time and mill current could lead to high-resolution NHAs without damage to the underlying layer (i.e. glass or Cytop).

The effect of the mill current on the resolution of NHAs was investigated. The dwell and mill times were fixed at 50 μs and 20 s, respectively. A higher mill current emits more ions per

unit time, and therefore the rate of removal of sample material is increased. Low (< 70 pA) mill currents are typically employed for resolution of sub-micron features. Figures 3.1 a and b show the ion beam and SEM images, respectively, for a mill current of ~3 pA. Incomplete removal of Au from the nanoholes was observed, and additional, irregular removal of the Au film outside of the NHA patterned area. Removal of Au from the nanoholes and overall NHA resolution increased when the mill current was increased to ~7 pA (Figs. 3.1 c and d). However, the larger mill current led to additional irregular removal from the bulk Au film, and over development of the NHA with numerous discontinuities in the connective Au regions of the NHA. Because the mill current could not be further tuned in between 3 and 7 pA, the mill current was fixed at ~3 pA to investigate the effect of total mill time on the NHA fidelity.

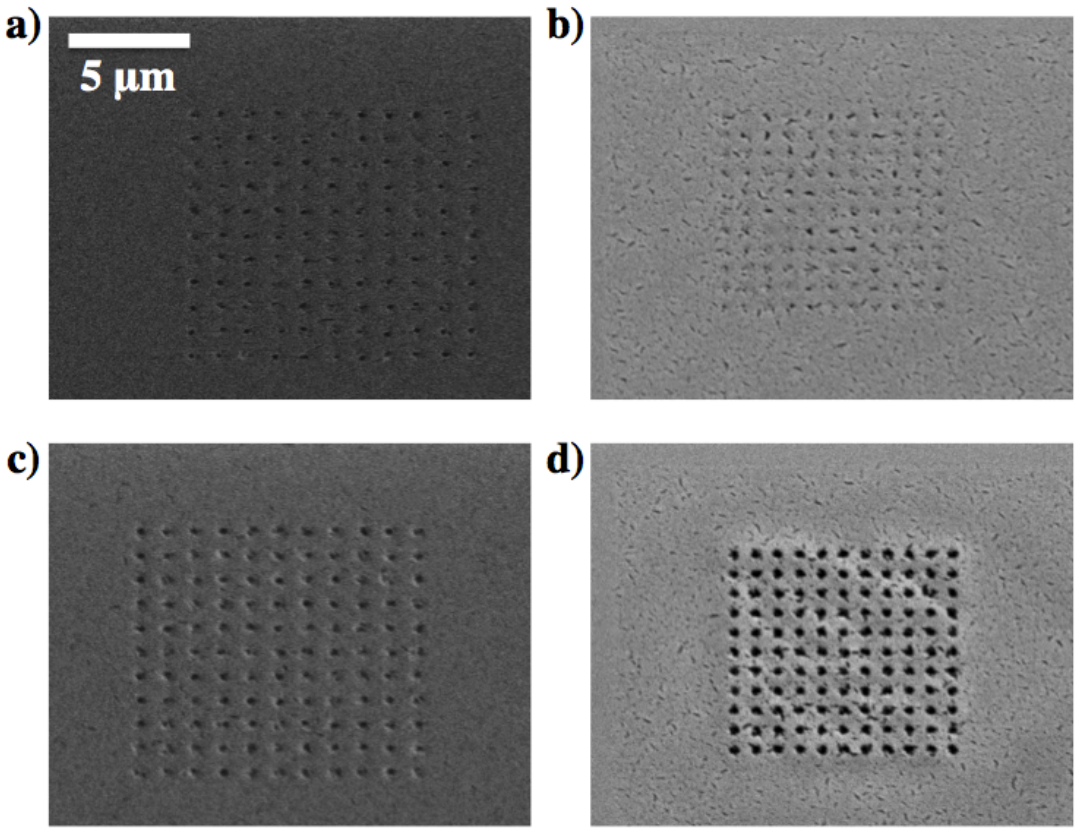

Figure 3.1. a,c) Ion beam and b,d) SEM images of NHAs resolved by FIB. The dwell and mill times were fixed at 50 and 20 s, respectively. The mill currents were a,b) ~3 pA, and c,d) ~7 pA.

A low mill current with an optimized mill time led to high resolution NHAs. The effect of total mill time on NHA resolution was investigated with a fixed dwell time and beam current of 50 μs and 3 pA, respectively. The mill time was increased from 2 to 30 s. Negligible amounts of Au material were removed from the bulk film for a 2 s mill time, as the NHA was completely unresolved (Fig. 3.2a). The NHA milled with a 10 s total mill time showed increased resolution compared to the 2 s mill time, but Au material was incompletely removed from the nanoholes (Fig. 3.2b). Complete removal of Au to resolve the NHA was observed for a 30 s mill time (Fig. 3.2c). A magnified SEM micrograph of the NHA shows that the ion beam was able to reach the underlying glass substrate, with successful production of periodic nanoholes (Fig. 3.2d).

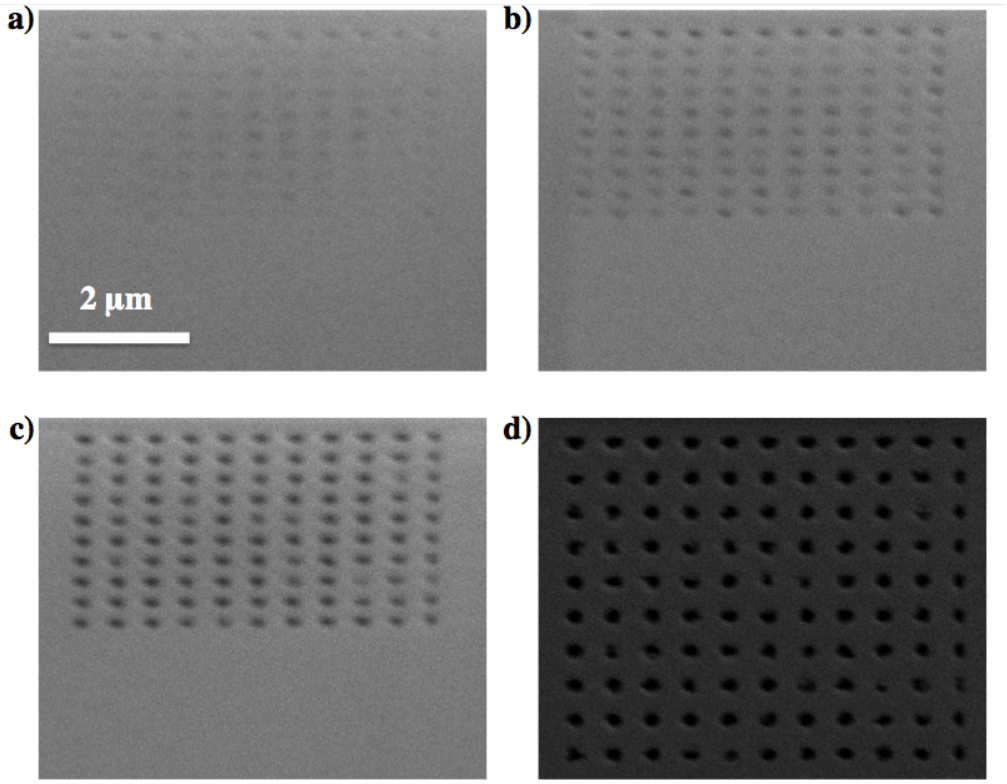

Figure 3.2. SEM micrographs taken at a-c) an incident angle of 52° relative to normal and d) normal incidence of NHAs milled with FIB for increasing times. Total mill times were 2, 10, and 30 s for a), b), and c-d), respectively. The dwell time and mill current for fixed at 50 s and 3 pA, respectively. All micrographs are on the same scale.

While NHAs were resolved by optimization of critical FIB lithography parameters, the FIB route to NHAs was not without drawbacks. FIB lithography is a low throughput technique that requires beam alignment for each individual substrate, making it time-consuming and costly. The resolution of the system was not fine enough to resolve the required features. Due to limitations of the software features could only be resolved within a 0.1 μm resolution, meaning that nanoholes with the required 150 nm diameter could not be resolved. Furthermore, software limitations allowed for a maximum array size of 10 μm x 10 μm, rendering further optical and SERS measurements impractical. Therefore, alternate routes to NHA fabrication were investigated.

EBL, with high-resolution capabilities, was investigated as a possible alternative route to fabricate NHAs in the LR structure. Following EBL patterning of NHAs in PMMA, the underlying and exposed Au areas were chemically etched to transfer the NHA pattern to the Au film. Incomplete etching of the exposed Au was observed for times < 7 min (Fig. 3.3a), and magnification of the image revealed approximately 50% of the Au remained on the surface (Fig. 3.3b). Minimal and substantial over etching was observed for development times of 10 and 12 min, respectively. While the NHA was nearly completely intact for the 10 min etch and exhibited a small degree of degradation (Fig. 3.3c), the 12 min etch had effectively removed all the Au from the array area (Fig. 3.3d).

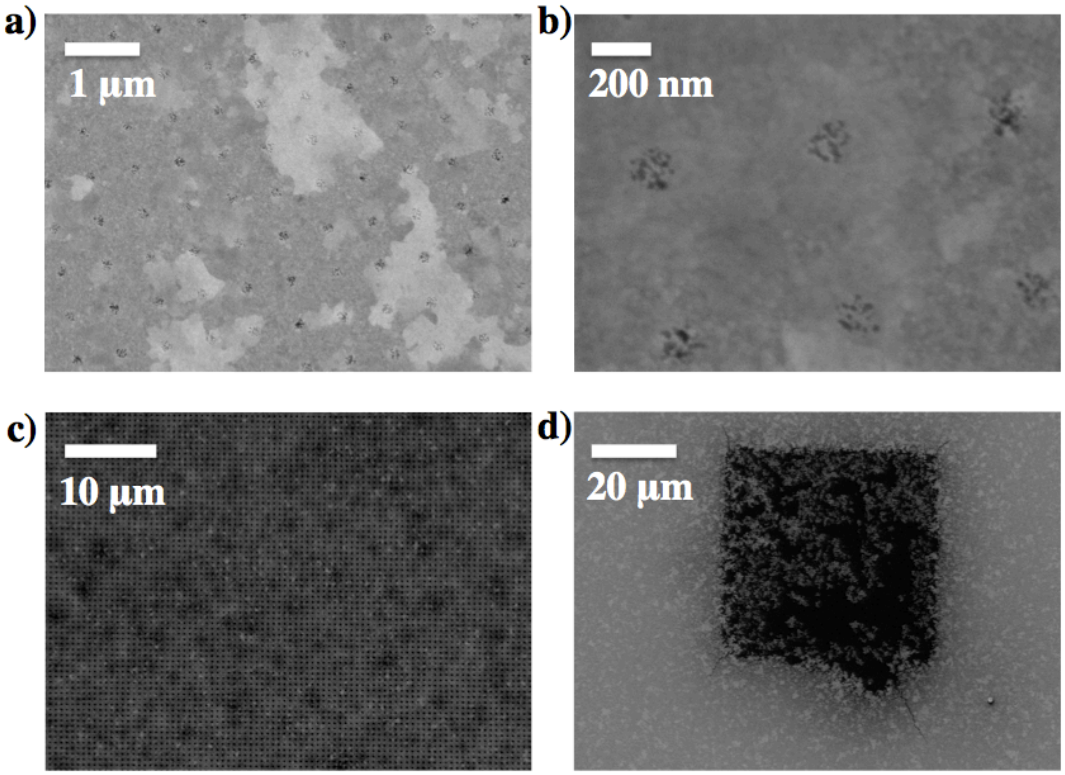

Figure 3.3. SEM micrographs of a, b) under etched and c, d) over etched NHAs prepared by EBL followed by chemical etching. The etching times were a-b) 5, c) 10, and d) 12 min.

Optimal development of the NHAs was observed for an etch time of 7 min. Uniform, large-area arrays (50 µm x 50 µm) were resolved (Fig. 3.4a). Close examination revealed that the nanoholes had been completely removed without undercutting the bulk Au film (Fig. 3.4b). This was confirmed with atomic force microscopy (AFM), which shows nanoholes with an approximate depth of 20 nm (Fig. 3.4c). Although, the NHAs developed with the optimal 7 min etching time displayed roughness around the edges of nanoholes (Fig. 3.4b). The roughness is attributed difference in the etching rates along the Au grain boundaries.

EBL followed by chemical etching proved to be an impractical route for fabrication of the NHAs. While the fabrication time was reduced relative to FIB lithography, EBL does not allow for modification of the Cytop layer. Similar to FIB, substrates with differing thicknesses need to be separately processed with EBL, reducing the throughput of this method. Furthermore,

it is unclear if exposing Cytop to the electron beam has any effect on the dielectric properties of Cytop. As the desired LR mode is highly sensitive to the local dielectric environment, any change in the optical properties of the Cytop layer could lead to poor device performance. With these considerations, a method capable of substrate-to-substrate modifications without the use of high-vacuum, low throughput equipment was sought out.

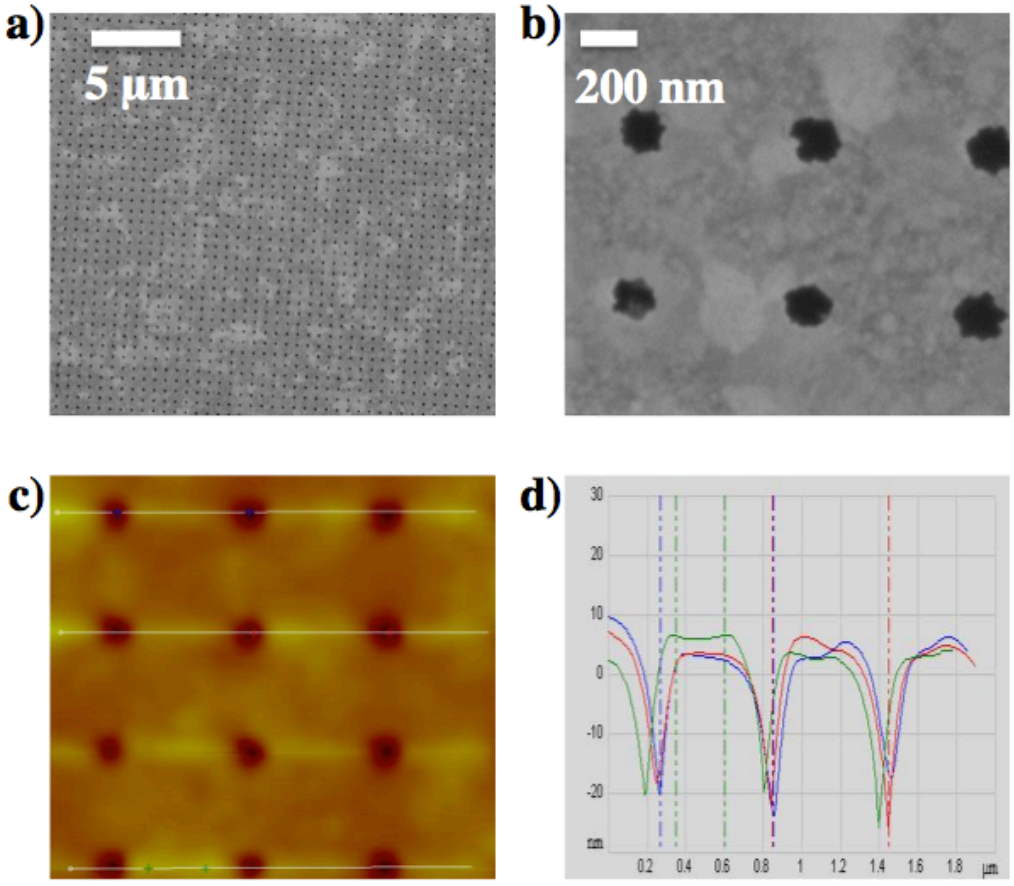

Figure 3.4. SEM micrographs of a) large-area and b) high-magnification NHAs resolved with EBL and chemical etching. c) AFM image of the NHAs, and d) corresponding trace showing the NHAs had an approximate depth of 20 nm.

Soft lithography offers a low-cost route to NHA fabrication without the need to develop individual substrates in electron or focused ion beam systems. While EBL is required initially for soft lithography to create the 'master' mold, subsequent substrates are replicated from the master without the further use of EBL. The general process of soft lithography consists of three

steps: construction of the silicon master mold, casting replicate molds of elastomeric material, and transfer of the pattern from the elastomeric mold to the device substrate. Here, the silicon master mold was fabricated by EBL and reactive ion etching (RIE). Figure 3.5 shows an SEM image of the master mold used in this work. The silicon nanopillars were designed with diameters, pitches, and heights of 300, 604, and 150 nm, respectively.

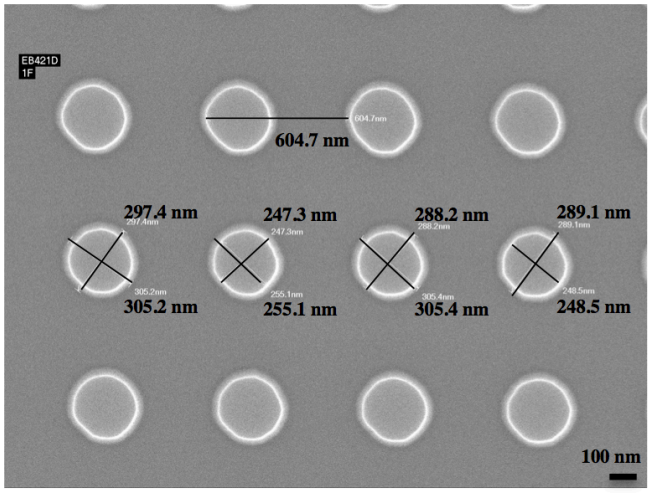

Figure 3.5. SEM micrograph of silicon nanopillars developed by EBL and RIE.

The pitch of the nanopillars was optimized by finite-difference time-domain (FDTD) as discussed in Chapter 2. Although the optimal diameter for the NHAs was determined to be 150 nm, the nanopillar diameter of the silicon master was fixed at 300 nm to allow for reduction of the nanopillars in subsequent processing steps. Change in the nanopillar diameter during the fabrication process occurred during a required O_2 plasma treatment step, and will be described in detail shortly. To provide structural stability, the nanopillar height was set to 150 nm. The aspect ratio, defined by the ratio of the nanopillar height to diameter (H/D), should be constrained to $0.1 < H/D < 5$ to maintain structural integrity of the elastomeric stamp. For PDMS stamps, sagging or deformation will occur if the aspect ratio falls outside of these bounds.[103]

Unsuccessful attempts were made to employ microcontact printing (μCP) as a possible alternative fabrication route to the desired NHAs. In μCP, a patterned self-assembled monolayer (SAM) is used to protect regions of the bulk Au film from the chemical etchant.[108] The exposed areas are removed by the etchant thereby facilitating transfer the pattern from the elastomeric stamp to the Au film. SAMs of octadecane thiol (ODT) were transferred to the 20 nm Au film using the cast PDMS stamps. The PDMS stamps were resolved with high fidelity over the entire 100 μm x 100 μm are (Fig. 3.6a). Visible cracks on the surface in Fig. 3.6b are attributed to low adhesion of the ~50 nm Au film that was deposited on the stamp to create a conductive surface for SEM imaging.

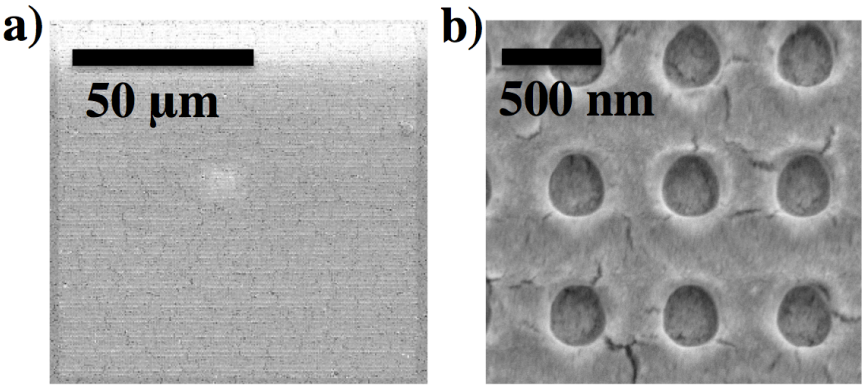

Figure 3.6. SEM micrographs showing a) large-area, and b) high-magnification of the h-PDMS/PDMS composite stamps cast from the silicon master mold shown in Fig. 3.5.

NHAs on the 20 nm Au film were not resolved. The ODT concentration, contact time of the stamp with the substrate, and emersion time in the gold etchant were varied. However, NHAs were not resolved in the 20 nm Au film, and the film remained continuous and unaffected by the etchant. While the mechanism of failure is unknown, it is postulated that diffusion of the ODT molecules on the Au film led to complete coverage by the ODT SAM, and thus resistance to the etchant. To reduce migration of surface bound ODT molecules methods have been presented to exploit the hydrophobicity of ODT. Submerged μCP is preformed by complete

emersion of the substrate in DI H_2O prior to substrate-stamp contact.[109] It is purposed that ODT will be confined to the stamp-H_2O interface, which will reduce diffusion of ODT molecules and produce high resolve features. Submerged μCP was attempted, but similar to conventional μCP no NHAs were resolved and the gold film remained unaffected by the etching solution. An alternate fabrication route was necessitated to develop NHAs through soft lithography.

Solvent-assisted nanomolding (SANM) successfully resolved NHAs in the conventional, pseudo long-range (PLR), and long-range (LR) structures by controlling the surface energy of the Cytop films. SAMN is used to transfer the master pattern to a substrate by molding a polymer film with a suitable solvent. Figure 3.7 shows a schematic illustration for the process developed in this work. The PDMS stamp was brought in contact with a PMMA-coated substrate, and acetone was used as the solvent. For PLR and LR structures, it was found necessary to increase the surface energy of the Cytop film by exposure to O_2 plasma. Without exposure spin coating of PMMA on Cytop was not possible, as centrifugal forces removed all PMMA during the spin coating process.

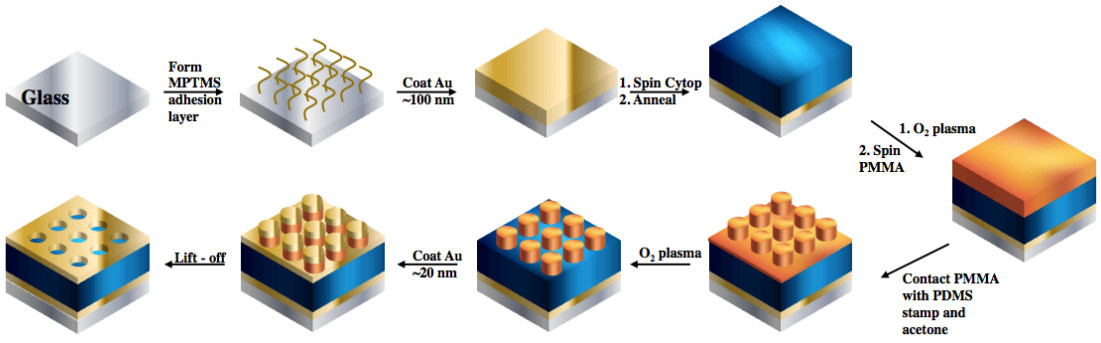

Figure 3.7. SANM process developed in this work used to generate NHAs in conventional, PLR, and LR structures.

Additionally, oxygen plasma treatment was found to be critical in production of densely packed, ultrathin Au films on Cytop. Ultrathin Au films with thicknesses < 20 nm can suffer from three-dimensional 'nanoislands' during the initial stages of film deposition on a range of

substrates.[110] As deposition continues, the void spaces are filled, and a continuous film is generated as the thickness approaches ~30 nm. The nanoscale roughness can lead to deviation of the dielectric properties of the Au film from the bulk properties, and thus an altered plasmonic response.[111] Surface energies for fluoropolymers are intrinsically low, which further pronounce the nanoisland effect. While the Cytop used in this work is formulated to promote metal adhesion, the nanoisland effect was observed (Fig. 3.8a). However, densely packed, ultrathin Au films were generated on oxygen plasma treated Cytop films. The nanoisland effect was partially mitigated by a 45 s O_2 exposure (Fig. 3.8b), and a clear reduction in void space is observed compared to the untreated substrate. A longer 90s O_2 exposure time led to continuous Au films (Fig. 3.8c). Using the ImageJ image processing software the Au surface coverage on the Cytop films for the untreated, 45 s exposure, and 90 s exposure times were approximated to be 81.9%, 90.6%, and 99.8%, respectively.

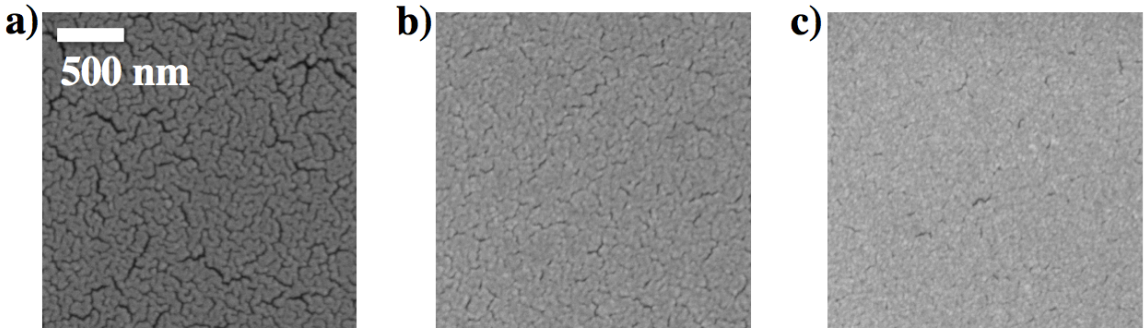

Figure 3.8. SEM micrographs of planar, Au films deposited on Cytop-coated glass substrates that had been exposed to oxygen plasma for a) 0 s, b) 45 s, and c) 90 s. All micrographs are on the same scale.

NHAs, were resolved in the conventional, PLR, and LR structures through layer-by-layer optimization. The finalized NHAs in the conventional and LR configuration are shown in Fig. 3.9. Transfer of the pattern from the PDMS stamp to the PMMA layer resulted in nanopillars with widths of 300 nm. After the 90 s O_2 plasma treatment, to remove residual PMMA and

activate the Cytop film, the diameter of the nanopillars was reduced to the desired 150 nm. The arrays displayed highly uniform features over the 100 μm x 100 μm area.

The optimized NHA fabrication route by SANM offered numerous advantages over the previous methods discussed. The use of specialized equipment such as EBL or FIB systems for individual substrate fabrication was completely eliminated. Instead, a one-time use of EBL enabled to fabrication of all subsequent devices. Fabrication capacity was increased as the SANM process enabled the three structure configurations, conventional, PLR, and LR, to be made from the same stamp. Furthermore, elimination of substrate-to-substrate variation due to user interference with the EBL of FIB systems, such as beam alignment, astigmatism correction, etc., led to highly reproducible NHAs in all three configurations. Optimized NHAs in the conventional, PLR, and LR configurations were then characterized based on their SERS response of surface-bound and solution phase small molecules.

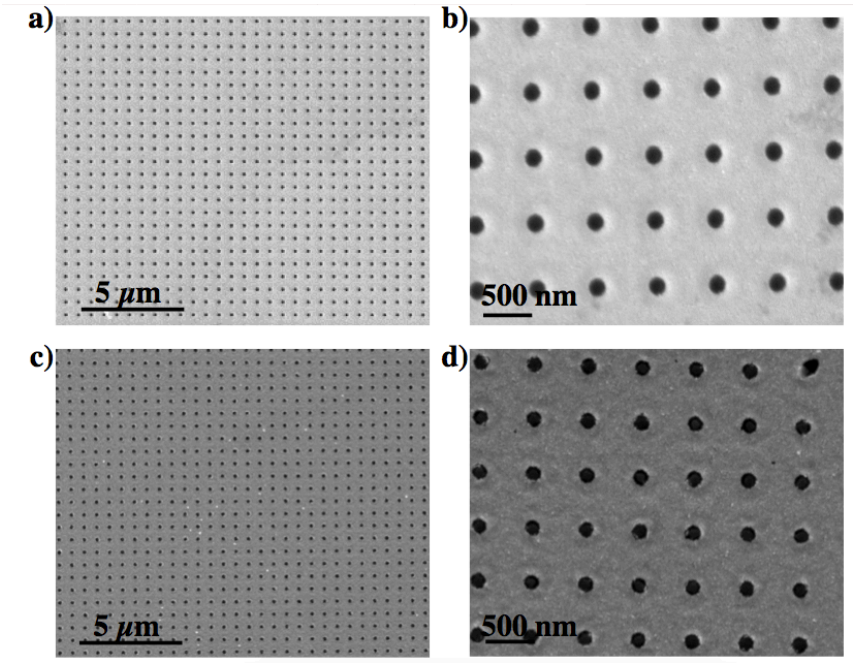

Figure 3.9. SEM micrographs of a, b) conventional and c, d) LR structures generated using the optimized SAMN process.

3.3.2 *SERS of Surface Bound Analytes*

The correlation between SERS performance and the electric field intensity of plasmonic nanostructures has been demonstrated in our previous studies.[41, 83, 90, 91] Here, we conducted a series of SERS experiments on conventional and PLR substrates with the gold NHAs fabricated via solvent-assisted molding.[103, 106] The NHAs had P = 604 nm, D = 148 ± 8 nm, and gold film thickness of 19 ± 2 nm. Conventional substrates were fabricated with gold NHAs directly on glass, while the PLR structures contained interstitial Cytop layers between the gold NHAs and glass substrate with thicknesses of 152 ± 6 nm and 580 ± 4 nm. Monolayers of 4-mercaptobenzoic acid (4-MBA) were immobilized on the NHAs. The substrates were then loaded in a homemade Teflon holder, filled with deionized water, and covered with a glass coverslip. Immersion of the substrates in water was necessary to fulfill dielectric symmetry. As discussed in the Chapter 2, the NHAs no longer 'feel' the underlying glass substrate when separated by Cytop cladding layers ≥ 250nm. Because the depth of the water separating the substrates and glass coverslips is ~500 μm, it can be assumed that the NHAs do not sense the presence of the coverslips, and thus should not deteriorate the desired dielectric symmetry.

Figure 3.10a shows representative SERS spectra of 4-MBA monolayers collected from the conventional and PLR substrates. Several prominent vibrational modes are observed, with the most notable being the bands at 525, 1077, and 1590 cm^{-1} which correspond to the C-S stretching mode, the in-plane benzene ring breathing mode, and totally symmetric benzene ring breathing mode, respectively.[112, 113] The SERS intensity increased from the conventional to the PLR substrate with Cytop thickness of 152 ± 6 nm, and further for the PLR substrate with a Cytop thickness of 580 ± 4 nm. Because the chemical enhancements of adsorbed 4-MBA can be assumed to be the same on all substrates, the increase in the SERS intensity is attributed only to

the coupling of LSPRs at opposite interfaces of the NHAs from the PLR substrates, and consequent electromagnetic enhancement. The experimentally measured peak intensity of the 1077 cm^{-1} band increased from 243 counts · s^{-1} · mW^{-1} for the conventional substrate, to 619 and 1147 counts · s^{-1} · mW^{-1} for the PLR substrates with Cytop thicknesses of 152 ± 6 and 580 ± 4 nm, respectively (Fig. 3.10b). The experimentally measured SERS intensities follow the same trend as a function of Cytop thickness as predicted by the FDTD calculated Q_F (Fig. 2.11a).

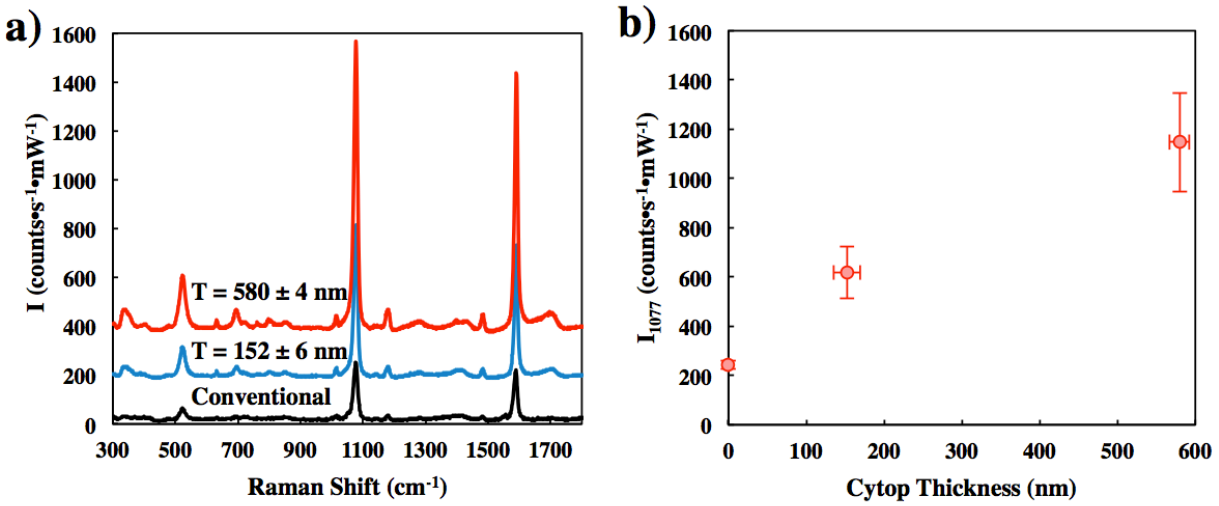

Figure 3.10. a) SERS spectra of 4-mercaptobenzoic acid (4-MBA) SAMs on SERS substrates in the conventional and PLR configurations. b) Intensity of the 1078 cm^{-1} vibrational mode from the 4-MBA SAMs as a function of Cytop thickness. Error bars represent three standard deviations from SERS and profilometry measurements collected from different locations on the individual 100 µm x 100 µm arrays.

3.3.3 *SERS on NHAs in Asymmetric and Symmetric Dielectric Environments*

LR-SERS substrates were fabricated with the optimized geometrical configurations obtained by the FDTD simulations to verify the extended field profile. We first verified the influence of the symmetry of dielectric media on the surface electric field intensity, that is, the SERS signals of molecules on the NHA surfaces. We formed monolayers of 4-MBA on freshly prepared LR-SERS substrates. To create dielectric symmetry on both sides of the NHA of the LR-SERS substrate, a 500 nm Cytop film was spun cast on top of the NHA with a 4-MBA

monolayer. The SERS spectrum was collected and is shown in Fig. 3.11a. To break dielectric symmetry, the SERS spectrum of 4-MBA on the freshly made LR-SERS substrate was collected directly in air (n = 1). The refractive index difference between air and Cytop creates an asymmetric dielectric environment, which leads to a reduction in the SERS signal as shown in Fig. 5a. Comparison of the 1077 cm^{-1} benzene ring breathing bands show an intensity of I_{1077} = 6.69 x 10^3 and 1.12 x 10^4 counts·s^{-1}·mW^{-1} for the SERS spectra collected on bare and Cytop-coated LR-SERS substrates, respectively.

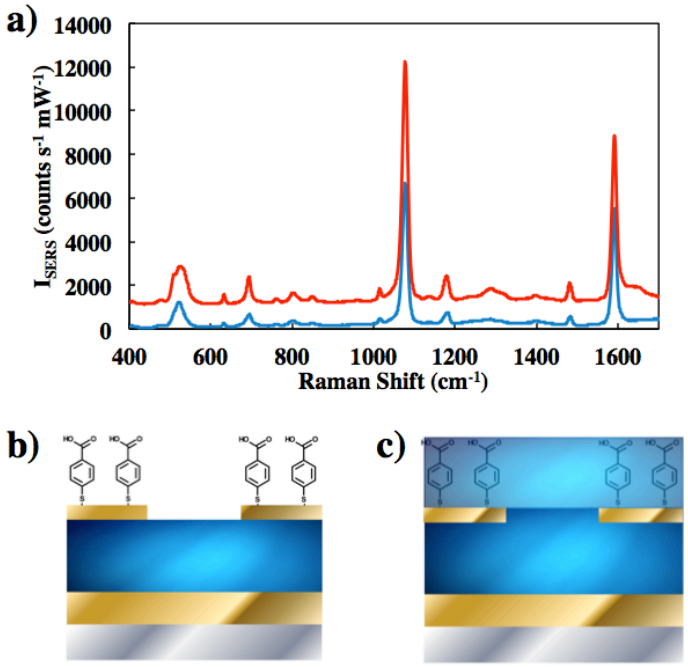

Figure 3.11. a) SERS spectra of 4-MBA SAMs collected on LR substrates in ambient air (blue trace) and with an additional 500 nm Cytop layer (red trace). Schematics for the b) ambient air and c) Cytop-coated configurations.

3.3.4 *Distance Dependent SERS Measurements*

The distance dependence of SERS signals on LR-SERS substrates was then investigated and compared to the conventional substrates. Ultrathin Cytop cladding layers were used to control the distance of the Raman reporter molecule, rhodamine 6G (R6G), from the gold NHA surfaces while maintaining the dielectric symmetry. A 10 nm Cytop cladding layer was spun

cast on the gold NHA surfaces of LR-SERS and conventional substrates. Even though the spin casting method cannot control the thickness precisely, nor offer many different thicknesses with a high resolution as the atomic layer deposition (ALD) technique provides,[114] it offers a quick, easy way to maintain the dielectric symmetry with Cytop. SERS spectra were collected with R6G on LR-SERS and conventional substrates with bare gold NHA surfaces and 10 nm Cytop-coated surfaces. To do so, the substrates were exposed to a 1 mM R6G aqueous solution for 30 min, air-dried, and then backfilled with DI H_2O in the Teflon holder. Figure 3.12a shows the SERS spectra of R6G at the gold NHA surfaces of the LR-SERS and conventional substrates. The LR-SERS substrate generated much stronger signals of the characteristic bands at 614, 770, 1197, 1314, 1365, and 1511 cm^{-1}, corresponding to the in-plane bending, C-H out-of-plane bending, and xanthene and phenyl ring breathing, respectively.[115, 116] Using the 1365 cm^{-1} band as an indicator, the peak intensities are 2.0 x 10^3 and 1.5 x 10^2 counts·cm^{-1}·mW^{-1} for the LR-SERS and conventional substrates, respectively. The SERS spectra of R6G collected from the 10 nm Cytop-coated surfaces of the LR-SERS and conventional substrates are shown in Fig. 3.12b.

The LR-SERS substrate still displayed prominent R6G characteristic bands while none were observed in the conventional substrate, confirming the presence of the extended electric fields predicted by the FDTD simulations. The peak height of the 1365 cm^{-1} band for the 10 nm Cytop-coated LR-SERS substrates was found to be 9.0 x 10^1 counts·cm^{-1}·mW^{-1} compared to 2.4 x 10^3 counts·cm^{-1}·mW^{-1} for the bare gold, LR-SERS substrate. Addition of the 10 nm Cytop cladding layer resulted in a signal intensity conservation of 4% compared to the bare gold LR-SERS substrate. The decrease of the SERS signal could be due to three factors: the decay of the electric field (the electromagnetic enhancement mechanism), the absence of possible charge

transfer between R6G and gold (the chemical enhancement mechanism), and the difference of R6G adsorption on Cytop and gold surfaces.

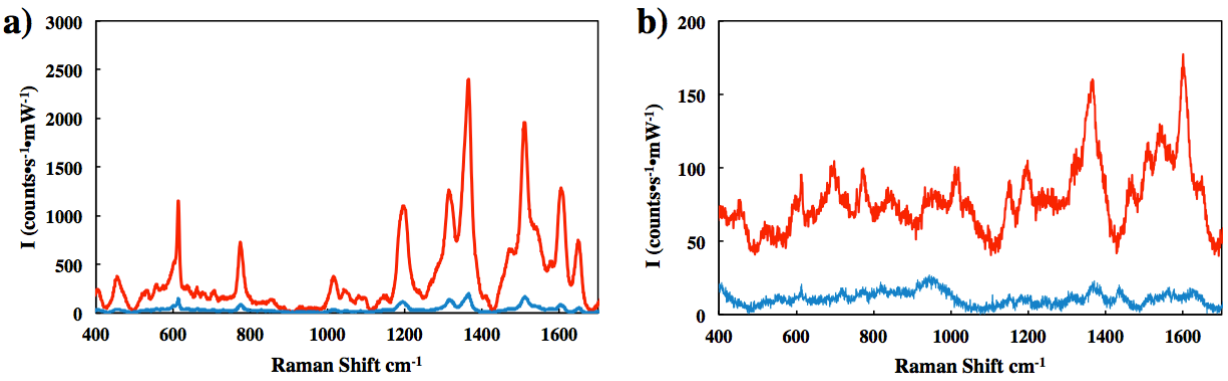

Figure 3.12. SERS spectra of 1 mM R6G collected on conventional (blue trace) and optimized LR (red traces) structures with a) no additional Cytop cladding layer, and b) a 10 nm Cytop cladding layer.

3.4 CONCLUSIONS

In conclusion, we investigated FIB, EBL followed by Au etching, and soft lithography with contact printing and solvent-assisted molding to develop NHAs in asymmetric and symmetric dielectric environments. FIB suffered from low-resolution (0.1 μm) of the NHAs and additional sputtering of the planar Au film regions. While EBL followed by Au etching generated NHAs, anisotropic etching of the Au film led to roughly defined nanoholes. Both FIB and EBL proved to be low-throughput processes that were incompatible of large-scale production of conventional, PLR, and LR devices, and flexibility of Cytop thickness modulation within the PLR and LR classes of devices. Therefore, soft lithographic routes were investigated. Diffusion of alkanethiol molecules on the Au film prevented development of NHA production by contact printing. Solvent-assisted nanomolding proved to be the most robust of the methods explored. Conventional, PLR, and LR devices were successfully resolved providing a high throughput route to parallel processing and modulation of Au and Cytop layers.

Additionally, we have observed long-range behavior in plasmonically engineered SERS substrates. This was accomplished by capitalizing on the benefits afforded by long-range surface plasmon resonance through incorporation of nanohole arrays into a symmetrical dielectric environment. Symmetrical dielectric environments were shown to increase the SERS intensity of the Raman label, 4-mercaptobenzoic acid. An increase of 170% was observed for the symmetrical LR-SERS substrate relative to the asymmetrical substrate. Importantly, distance dependence measurements showed that the LR-SERS substrates were capable of R6G detection with a separation distance of 10 nm between the SERS-active surface and Raman reporter. The LR-SERS substrates describe here represent an interesting class of SERS substrates that can fundamentally expanded to include other plasmonic nanostructures, or applied to SERS applications requiring an extended probing depth.

Chapter 4. ENRICHMENT AND CHARACTERIZATION OF BACTERIA WITH COMBINED DIELECTROPHORESIS AND SURFACE-ENHANCED RAMAN SCATTERING IN A MICROFLUIDIC SYSTEM

4.1 INTRODUCTION

Global bacterial infections continue to rise with increasing instances of antibiotic resistance. In the United States alone, antibiotic resistant bacterial infections are responsible for over 2 million hospitalizations annually, costing an estimated $20 billion.[117] Increased occurrences of antibiotic resistant bacterial strains stems from both societal and technological inadequacies. The exact cause of antibiotic resistance is uncertain; in general however, it is believed to occur due to under regulation of antibiotics in developing countries and over prescription of wide-spectrum antibiotics in the developed world.[118-120] The use of wide-spectrum antibiotics is the result of bacterial identification lag time after initial sample collection. Currently, the gold standard for bacterial identification employ culture-based techniques that take ~48 hr for successful identification. Technologies enabling faster bacterial identification would allow clinicians to prescribe narrow-spectrum antibiotics, in turn lessening the evolutionary pressure for the genesis of further antibiotic resistance mechanisms.

To overcome identification lag time of bacterial samples, numerous biosensing technologies have been developed including electrochemical, genetic (i.e. PCR), and optical biosensors.[2, 3, 121] Optical biosensors based on surface-enhanced Raman scattering (SERS) are uniquely suited for bacterial sensing. SERS-based biosensors are inherently sensitive (single

molecule detection), do not require reagents, and produce distinctive bacterial "biochemical fingerprints" that enable rapid bacterial identification.[40, 122, 123]

SERS, a vibrational form of spectroscopy, is generated by a two-part mechanism consisting of a chemical enhancement element[35] and an electromagnetic enhancement element,[36] with the electromagnetic component dominating the enhancement process.[34] The electromagnetic enhancement, also referred to as localized surface plasmon resonance (LSPR), is caused by amplification of electric fields on the nanostructured surface through coupling of the electric-field component of incident light to the conduction electrons on the metal surface. SERS is a near-field effect that requires proximity of the target analyte within ~2 nm of the SERS-active surface for successful detection.[48] The nanoscale sensing region can lead to long detection times and lower the detection sensitivity attributed to diffusion-limited mass transport in the device.[124]

Multiple strategies have been proposed to overcome the diffusion-limited mass transport of target analytes in SERS devices. The objective of each strategy is to intimately contact the cell with the SERS-active surface in a simple, timely manner. Example strategies to achieve this goal have incorporated core-shell magnetic nanoparticles,[65, 66] functionalized coatings,[125] microfluidic focusing,[67] and dielectrophoresis (DEP)[68] into the SERS sensing routine. Of these strategies, DEP has proved to be a viable option for SERS-based bacterial biosensing.[50, 71, 72, 126-128]

DEP is particle movement in the presence of asymmetrical alternating current (AC) electrical fields.[129] The direction of particle movement is dependent on the complex permittivities of the particle and suspending medium, particle size, and local electric field gradient. Particles that migrate towards regions of maximum and minimum local electric field

gradients experience positive DEP (pDEP) and negative DEP (nDEP), respectively. Furthermore, the frequency dependence of the complex permittivities of the particle and suspending medium can be exploited to induce pDEP or nDEP on the particle. Micron-scale bacterial cells are highly amenable to dielectrophoretic manipulation, enabling confinement of large numbers of cells in the sensing region.[130]

Combined DEP and SERS has been used for successful detection of bacteria using both SERS-active nanostructured surfaces[126-128] and nanoparticles.[50, 71, 72] DEP-SERS bacterial biosensing requires the use of various trapping frequencies from several hundred to several millions of hertz. To achieve specific, quantitative analysis and detection of bacteria using DEP-SERS, it is essential to understand whether bacterial cells undergo changes and/or the LSPR of SERS-active substrates are influenced by the externally applied electric fields.

Here, we developed a SERS-based microfluidic biosensor combined with DEP utilizing a point-and-plate DEP electrode configuration with indium-tin oxide (ITO) coated glass as a DEP plate electrode and quasi-3-dimensional (Q3D) plasmonic gold nanostructure arrays to act as both a DEP point electrode and SERS-active substrate. The device allowed for the investigation of bacterial trapping via DEP, SERS signal enhancement, and the effect of applied DEP frequency on the bacterial SERS spectra. The device successfully demonstrated the DEP function by trapping 2 μm polystyrene microparticles and *E. coli* cells, with frequency dependencies in good agreement with theoretical calculations. An improved SERS performance was shown using DEP-enhanced mass transport of bacterial cells compared to diffusion-limited mass transport. Furthermore, the dependence of the applied DEP frequency on the SERS spectra of Gram-negative (*E. coli*) and Gram-positive (*Staphylococcus epidermidis*) bacteria were investigated through statistical analysis. Principal component analysis (PCA), k-nearest

neighbor (kNN), linear discriminant analysis (LDA), and support vector machine (SVM) multivariate statistical analyses were conducted to quantify the difference in observed variance of the SERS spectra under different DEP conditions. No statistically relevant differences were observed in the SERS spectra of *E. coli* or *S. epidermidis* in the applied DEP frequency range of 500 Hz – 10 MHz.

4.2 EXPERIMENTAL

4.2.1 *Materials and Reagents*

Poly(methyl methacrylate) (PMMA) was purchased from Microchem (Westborough, MA). Polystyrene (PS) microspheres (d = 2 μm) were purchased from Thermo Scientific (Fremont, CA). Sodium chloride, tryptone, and yeast extract for cell culture were purchased from Sigma-Aldrich (St. Louis, MO). *Escherichia coli* (ATCC 25922) and *Staphylococcus epidermidis* (ATCC 14990) were purchased from American Type Culture Collection (Manassas, VA). Gold shot was obtained from DHF Technical Products (Rio Rancho, NM). Indium-tin oxide (ITO)-coated glass was purchased from Colorado Coating Concepts (Loveland, CO). All materials were used as received.

4.2.2 *Fabrication of DEP-SERS Substrates and Microfluidic System*

The schematic illustration of the fabrication of a DEP point electrode with Q3D plasmonic gold nanostructured arrays is illustrated in Fig. 4.1a. A 300 nm PMMA film was spun cast onto a 4 in silicon wafer. The nanohole arrays, 400 nm in diameter and 500 nm in pitch, were resolved via electron beam lithography. Four individual arrays, which measured 50 μm x 50 μm each, were developed per 1 cm^2 substrate, and were arranged in a square grid with a 200 μm spacing in the center of each substrate. SEM and AFM images of the Q3D arrays are shown

in Figs. 4.1b and c, respectively. The gold deposition mask with a 500 µm x 0.6 cm opening were made with a CO_2 laser cutter (Universal Laser Systems, Scottsdale, AZ), which allowed complete gold coverage of the four Q3D arrays and simultaneous produced the 'point' electrode for DEP experiments. A 50 nm gold layer was deposited by thermal evaporation (Edwards Auto 306). The as-fabricated point electrode on a l cm x 1 cm silicon chip was placed in a homemade Teflon holder. Copper wires (24 gauge) were electrically connected to the gold SERS electrode and an ITO-coated glass, respectively, with silver paint (Ted Pella, Redding, CA), and the other leads were connected to the function generator (GW Instek, AFG-2250). A polyethylene terephthalate (PET) gasket with a height, width, and length of 90 µm, 500 µm, and 1.4 cm, respectively, was attached to the ITO glass, and used to define the microchannel and electrode gap. A schematic for the device is shown in Fig. 4.2a.

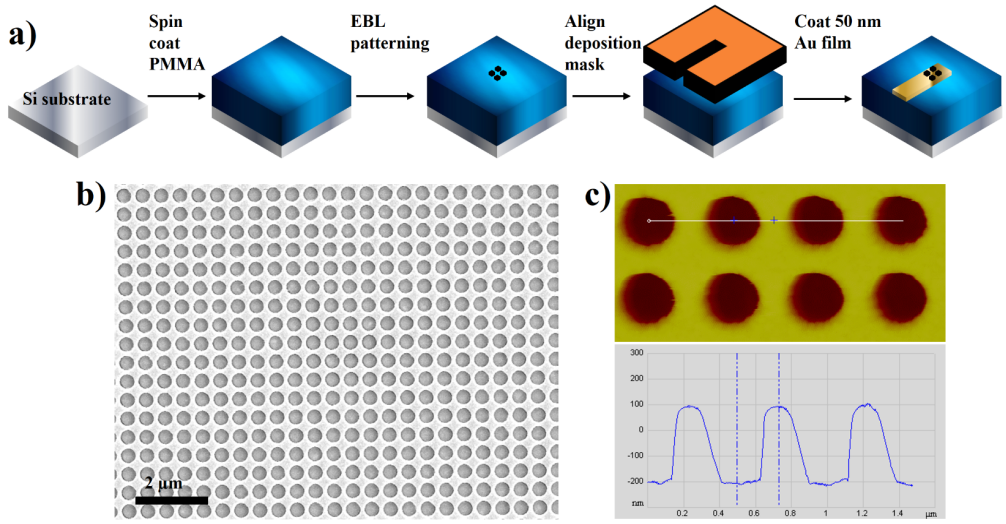

Figure 4.1. a) Schematic illustration demonstrating the process flow to fabricate the Q3D plasmonic nanostructured point electrodes. b) Scanning electron microscopy image of the Q3D plasmonic nanostructured arrays. The diameter and pitch of the nanoholes are 400 and 500 nm, respectively. c) Atomic force microscopy image of the Q3D plasmonic nanostructured arrays that show a nanohole depth of ~300 nm.

4.2.3 *Bacterial Culture*

The bacterial samples were received as a freeze-dried pellets and used to make glycerol cell stocks. Cell stocks were stored at -80^{o}C, and used for the entirety of the experiments. Single plates were streaked from the cell stock to isolate single colonies. Colonies were transferred to 5 mL of Lysogeny broth (LB) in a sterilized culture tube, and placed in a warm room (37^{o}C) for 16 h on an orbital shaker at 250 RPM. The inoculate was then added to 45 mL of LB in an autoclaved 250 mL Erlenmeyer flask, and placed back into the warm room on the orbital shaker. The bacteria were grown to an OD_{600} of 0.6. The bacteria were harvested, and washed by three successive centrifugation (15,000 x g) and resuspension steps in deionized (DI) water. The bacterial suspensions were diluted to 10^8 CFU/mL, and immediately used in the SERS experiments.

4.2.4 *DEP Trapping of Particles in Microfluidic Conditions*

Particles (PS spheres or *E. coli* cells) suspended in DI H_2O were introduced into the device via a syringe pump (Chemyx, Fusion 200). Fresh solutions were prepared immediately before trapping experiments to minimize changes in the solution conductivity or pH. For the PS microspheres, the frequency of the applied AC signal, flowrate, and applied peak-to-peak potential were varied from 500 Hz to 10 MHz, 1 – 50 μL/min, and 5 and 10 V_{pp}, respectively. The trapping experiments for *E. coli* were conducted at 1 μL/min with a 5 V_{pp} applied potential, and the frequency was varied between 500 Hz to 10 MHz. The ImageJ software package was used to process the images collected through a 10x objective to determine the number of PS microspheres and *E. coli* cells that have been trapped under different conditions.

4.2.5 *Dynamic Detection of E. coli Under Microfluidic Conditions*

Flow experiments were carried out with the same microfluidic device described above, with the volumetric flowrate fixed at 1 μL/min. The Renishaw inVia Raman microscope, equipped with a 785 nm NeHe laser and 1200 l/mm grating, was used to collect the SERS spectra. The rectangular laser beam was focused through a 50x objective (W.D. 0.5 mm, N.A. 0.8) with an approximate beam size of 2 μm x 20 μm. All SERS spectra were collected at 1% laser power (1.2 mW) and 2 accumulations, with 20 s total exposure time in the 700 – 1700 cm^{-1} spectral window. The temporal SERS signals were collected for *E. coli* concentrations of 10^5, 10^7, and 10^8 CFU/mL with and without the application of DEP. The 10^5 CFU/mL suspension was allowed to pass through the device for ~40 min without the application of DEP, after which the function generator was used to apply a 5 V_{pp} potential at 500 Hz to the device for ~20 min. The applied potential was re moved, and the 10^7 CFU/mL solution was flowed through the device for ~20 min without DEP, followed by another ~20 min with DEP. The concentration was increased to 10^8 CFU/mL and the ~20 min DEP on-off cycle was repeated.

4.2.6 *Frequency Dependence of Bacterial SERS Spectra*

The microchannel was filled with *E. coli* or *S. epidermidis* suspensions (10^8 CFU/mL), and allowed to incubate for 20 min. The incubation step allowed settling of bacterial cells to the Q3D plasmonic nanostructured surface. A function generator varied the frequency from 500 Hz to 10 MHz with a constant peak-to-peak potential of 5 V_{pp}. SERS spectra were collected using the protocol described above. A total of 10 and 19 spectra were collected at each frequency in the *S. epidermidis* and *E. coli* measurements, respectively.

4.2.7 *Chemometrics Methods*

All SERS spectra were collected with the Renishaw Wire 3.0 software, and further processed with Matlab. Prior to statistical analysis, individual spectra were preprocessed via a three-step procedure: baseline subtraction with the asymmetric truncated quadratic routine (6^{th} order), noise filtering with Savitzky-Golay (5^{th} order), and standard normalized. For PCA, the entire *E. coli* and *S. epidermidis* datasets were independently analyzed, and sequentially combined to validate the identification performance. Three classifiers (kNN, SVM, and LDA) were used to quantify the similarity of the individual datasets. A 90/10 split was used for the training/predicting datasets of the bacterial SERS spectra at different frequencies. The applied DEP frequency was used as the predictors for the classifiers. The accuracy of the individual classifiers was defined by the number of correctly identified SERS spectra to the total number of SERS spectra.

4.3 RESULTS AND DISCUSSIONS

4.3.1 *Design of the DEP-SERS Device and Microfluidic Systems*

The design of the DEP-active electrode is critical to the performance of the DEP-SERS microfluidic biosensor. Previous electrode arrangements used in SERS studies have implemented in-plane[131] and point-and-plate[132] configurations. In-plane electrodes are directly patterned on the substrate (i.e. glass slide), and typically adopt a quadrupole or interdigitated arrangement.[76] In the point-and-plate configuration, electrodes with differing surface areas are vertically displaced, and the electrode asymmetry results a large electric field gradient near the point electrode. Both configurations can produce large electric field gradients at either the edge of the in-plane electrodes or at the point electrode, and have been incorporated into microfluidic

devices. However, for microfluidic applications, the point-and-plate configuration has the added advantage that all particles experience the DEP force, which thus enhances the trapping efficiency. Therefore, the point-and-plate configuration was chosen in this work for the DEP-SERS microfluidic biosensor.

Figure 4.2a depicts a schematic representation of the DEP-SERS microfluidic biosensor. The microchannel was defined by a PET gasket with a height, width, and length of 90 μm, 500 μm, and 1.4 cm, respectively. Additionally, the PET gasket fixed gap (90 μm) between the four Q3D plasmonic nanostructured arrays and ITO-glass, which acted as the point and plate electrodes, respectively. Previous finite element simulations showed that the DEP force increases as the gap between the nanostructured electrode and ITO electrode decreased.[124] However, for a fixed volumetric flowrate, the decreased electrode gap results in an increased drag force on the particle, and thus necessitates a larger DEP force for efficient cell transport to the sensing surface as illustrated in Fig. 4.2b. While previous point-and-plate configurations maintained electrode gaps in the range of 20 – 40 μm,[124, 126, 132] the 90 μm spacing used here balanced a large electric field gradient against unnecessarily high drag forces. For similar nanohole array-based point electrodes, the electric field gradient was shown to decrease by a factor of 5 when comparing gaps of 40 μm and 90 μm.[124]

Convection, diffusion, and adsorption occur simultaneously in microfluidic channels, with diffusion typically being the limiting process.[51] The laminar flow common to microfluidics does not facilitate efficient mixing leading a maximal cellular concentration in the center of the channel.[133] For efficient sensing, the externally applied DEP force is necessary to promote cellular migration from the channel center to the Q3D sensing surface. The Q3D plasmonic nanostructured arrays can induce the largest electric field gradient in the immediate vicinity of

the Q3D point electrode. Therefore, under pDEP conditions bacterial cells are transported to the SERS-active point electrode where detection can occur.

Figure 4.2c shows the structure of the Q3D plasmonic nanostructured arrays, which have nanohole diameters of ~400 nm and gap widths of ~100 nm in a square lattice. SEM and AFM images of the Q3D arrays are shown in Figs. 4.1b and c, respectively. The Q3D plasmonic nanostructured arrays have been extensively studied and characterized, and have shown remarkable plasmonic properties[90, 91] as well as applications for detection in complex media with unique surface functionalizations. [41, 134-137] The Q3D nanostructures in the DEP-SERS device were tuned such that the strongest local electric fields (i.e., 'hot spots') occur at the edges of the 100 nm gaps between neighboring nanoholes on the top gold layer, making the 'hot-spot' accessible to large analytes such as bacterial cells.[83]

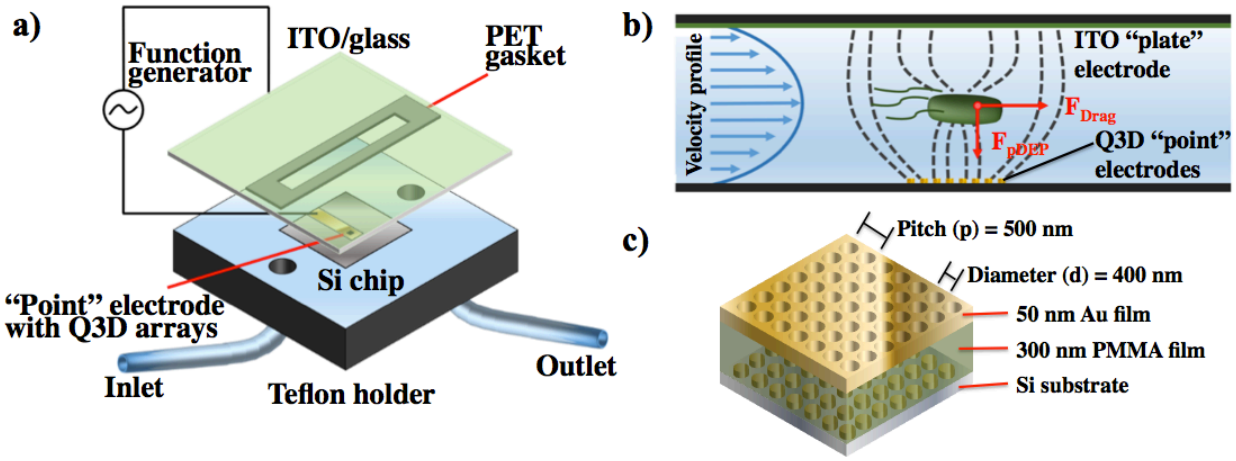

Figure 4.2. a) Schematic representation of the overall configuration of the DEP-SERS. microfluidic biosensor. The 1 cm^2 silicon chip with four Q3D plasmonic nanostructured arrays (50 µm x 50 µm each) on a 500 µm x 0.6 cm gold electrode, which acted as a DEP point electrode, was nested in a homemade Teflon holder. The microchannel is defined by a PET gasket (height x width x length = 90 µm x 500 µm x 1.4 cm) that determined the gap (90 µm) between the point-electrode with Q3D plasmonic nanostructured arrays and ITO-coated glass plate-electrode. Each electrode was connected to a function generator to control the input AC signal. The flowrate was controlled by a syringe pump. b) Drag force acts on the bacterial cell caused by a laminar, parabolic flow while a positive dielectrophoretic force attracts the bacterial cell towards the point electrode with Q3D plasmonic nanostructured array as it traverses the

microchannel. c) Perspective of the Q3D plasmonic nanostructures. The gold thickness, PMMA thickness, nanohole diameter, and nanohole gap are 50, 300, 400, and 100 nm, respectively.

4.3.2 *Particle and Cell Trapping with the DEP-SERS Device*

The trapping abilities of the DEP-SERS device were first examined using 2 μm PS microspheres. Particle directional movement by DEP is determined by the CM factor. Positive CM values lead to pDEP, and particle movement towards regions with high electric field gradients. Likewise, a negative CM value will result in nDEP, and particle migration towards regions with low electric field gradients. For a homogeneous, spherical particle, the CM factor is given by Eqs. 1.4 -1.7.

The CM factor versus frequency for the PS microspheres suspended in DI H_2O (ε_m = 78.5, $\sigma_m = 10^{-4}$ S/m) was calculated (Fig. 4.3a). Positive DEP is predicted for low frequencies, with a single crossover frequency (COF) observed at 7.93×10^5 Hz. Frequencies higher than the COF are expected to induce nDEP on the PS microspheres. To verify the DEP trapping of PS microspheres in our DEP-SERS device, initial flow experiments were conducted in the frequency range of 500 Hz to 10 MHz with fixed applied potential, flowrate, and particle concentration of 5 V_{pp}, 1 μL/min, and 10^7 particles/mL, respectively. Microsphere adsorption on the entire gold point-electrode was viewed via optical microscopy, and the collected images were processed with a particle counting routine in the ImageJ software to determine the number of trapped PS microspheres. An image was collected at time-zero for each of the applied frequencies, and the number of particles present in the image was subtracted from subsequent images. Thus the images have been normalized to account for fluctuations in number of particles present in the time-zero images at different frequencies. The trapping efficiency was monitored as a function of time for a range of applied frequencies.

Frequencies below ~100 kHz display positive, near-unity CM factors ranging from ~0.9 to ~0.94 (Fig. 4.3a), which indicate similar pDEP forces are exerted on the PS microspheres. For low applied frequencies of 500 Hz and 1 kHz, in which particle trapping was recorded for 210 and 300 s, respectively, a linear response was observed (Fig. 4.3b). As the frequency was further increased to 10 and 100 kHz, effective microsphere trapping was still observed. Direct comparison at the 120 s time point in the low frequency regime revealed that 207, 190, 227, and 246 microspheres were trapped by applied frequencies of 0.5, 1, 10, and 100 kHz, respectively. For applied frequencies above the COF, 1 and 10 MHz, no particles were trapped after a 120 s application of the 5 V_{pp} potential. The results are in good agreement with the theoretical predictions, which indicate successful implementation of pDEP and nDEP on the PS microspheres by the DEP-SERS device.

A larger flowrate can lead to increased SERS detection performance of small molecules due to the increased analyte flux through the microchannel.[138] For a micron-sized particle however, the increased flowrate results in a larger drag force exerted on the particle by the fluid, and consequently, a reduction in the trapping efficiency. Therefore, we investigated, for a fixed 500 Hz frequency, the trapping dependence on volumetric flowrate (Fig. 4.3c). Flowrates of 1, 5, 10, and 50 μL/min were chosen for a fixed particle concentration of 10^7 particles/mL and an applied potential of 5 V_{pp}. No particle trapping was observed at flowrates of 10 and 50 μL/min, and a maximum of 35 microspheres were trapped at 5 μL/min. The drag force on the microspheres was too large at 5 μL/min to be overcome by the DEP force, and no continual increase in the amount of trapped particles was observed on the point electrode. However, a flowrate reduction to 1 μL/min led to substantial particle trapping, with over 515 particles trapped after application of DEP for 300 s. With a 1 μL/min flowrate, the DEP force is greater

than the drag force, and microspheres are effectively trapped on the point electrode as evidenced by the linear increase in the amount of microspheres trapped with time. The dependence of trapping efficiency on applied potential was investigated. The potential was varied from 5 to 10 V_{pp} with fixed flowrate, concentration, and frequency of 1 μL/min, 10^7 particles/mL, and 500 Hz, respectively. Within the first 30 s of applied DEP, the higher voltage resulted in more particle adsorption, with 127 compared to 281 microspheres trapped by applied potentials of 5 and 10 V_{pp}, respectively (Fig. 4.3d). The 10 V_{pp} applied potential resulted in a particle adsorption plateau, with an increase to ~370 adsorbed particles at t = 90 s, to a final adsorption of ~400 particles at t = 210 s. Comparatively, the 5 V_{pp} potential showed a linear particle adsorption trend, with a total of 350 microspheres trapped on the point electrode after DEP application for 210 s.

The DEP force scales with the square of the electric field gradient (Eq. 1.3). Therefore it is expected that larger applied voltages will lead to more efficient particle trapping. However, the effect of the applied potential on the bacterial cell with respect to the frequency must also be considered. At low frequencies bacterial cells tend to act as non-conducting spheres, with the potential drop occurring in the outermost membrane of the cell.[139] Yet at higher frequencies, the applied field is able to penetrate through the entire cell. Furthermore, molecular structures, such as cellular membranes, can undergo reorganization in strong electrical fields.[140] Therefore, to minimalize transmembrane stress on the *E. coli* cells, a 5 V_{pp} potential was chosen to explore the trapping capabilities of the DEP-SERS device.

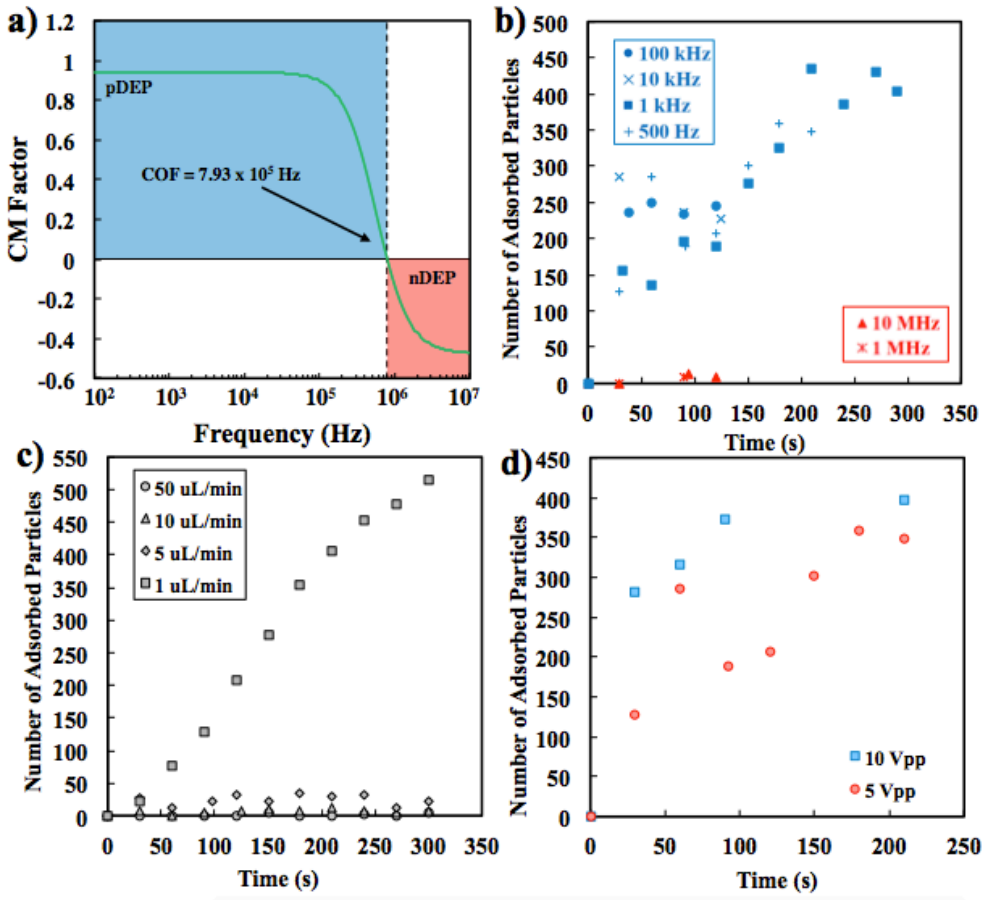

Figure 4.3. a) Calculated Clausius-Mossotti (CM) factor for a 2 µm polystyrene microsphere as a function of frequency that shows a single crossover frequency (COF) at 7.93 x 10^5 Hz. The microsphere is subjected to pDEP at frequencies below the COF, and nDEP for frequencies above the COF. Experimentally observed number of polystyrene particles trapped as a function of time for b) frequencies in the range of 500 Hz – 10 MHz with a 1 µL/min flowrate and 5 V_{pp} applied potential, and c) flowrates of 1, 5, 10, and 50 µL/min with a 5 V_{pp} applied potential at 500 Hz.

Gram-negative bacteria, such as *E. coli*, contain a characteristic dual-layered membrane structure that encapsulates the cytoplasmic space. A two-shell model was employed to account for different dielectric properties of the cell cytoplasm, membrane, and wall, as well as the oblong shape.[141] *E. coli* was modeled as an oblate particle, 2 µm in length and 500 nm in diameter, in a three-layer structure consisting of a cytoplasm, cell membrane (10 nm in thickness), and cell wall (40 nm in thickness). The permittivity and conductivity of each layer were taken from previously reported values.[142] Unlike the polystyrene microsphere or *S.*

epidermidis cell, the oblong shape of *E. coli* requires the CM factor to be calculated along its three principal axes (x, y, z):[141]

$$\text{CM}(\omega) = \frac{1}{3} \sum_{j=x,y,z} \frac{1}{3} \left(\frac{\varepsilon^*_{1j} - \varepsilon^*_m}{\varepsilon^*_m + (\varepsilon^*_{1j} - \varepsilon^*_m) A_{0j}} \right) \quad \text{Eq. 4.1}$$

where ε^*_{1j} and A_{ij} (i = 1, 2, 3) are defined as:

$$\varepsilon^*_{1j} = \varepsilon^*_{wall} \frac{\varepsilon^*_{wall} + (\varepsilon^*_{2j} - \varepsilon^*_{wall}) A_{1j} + \lambda_1 (\varepsilon^*_{2j} - \varepsilon^*_{wall})(1 - A_{0j})}{\varepsilon^*_{wall} + (\varepsilon^*_{2j} - \varepsilon^*_{wall}) A_{1j} - \lambda_1 (\varepsilon^*_{2j} - \varepsilon^*_{wall})(1 - A_{0j})} \quad \text{Eq. 4.2}$$

$$A_{ix} = \frac{q_i}{(q_i^2 - 1)^{3/2}} \ln\left[q_i + (q_i^2 - 1)^{1/2}\right] - \frac{1}{q_i^2 - 1} \quad \text{Eq. 4.3}$$

$$A_{iy} = A_{iz} = \frac{1}{2}(1 - A_{ix}) \quad \text{Eq. 4.4}$$

and ε^*_{2j}, q_i, λ_1, and λ_2 are defined as:

$$\varepsilon^*_{2j} = \varepsilon^*_{mem} \frac{\varepsilon^*_{mem} + (\varepsilon^*_{cyto} - \varepsilon^*_{mem}) A_{2j} + \lambda_2 (\varepsilon^*_{cyto} - \varepsilon^*_{mem})(1 - A_{1j})}{\varepsilon^*_{mem} + (\varepsilon^*_{cyto} - \varepsilon^*_{mem}) A_{2j} - \lambda_2 (\varepsilon^*_{cyto} - \varepsilon^*_{mem}) A_{1j}} \quad \text{Eq. 4.5}$$

$$q_i = \frac{a_i}{b_i}, \lambda_1 = \frac{a_1 b_1 c_1}{a_0 b_0 c_0}, \text{ and } \lambda_2 = \frac{a_2 b_2 c_3}{a_1 b_1 c_1} \quad \text{Eqs. 4.6-4.8}$$

where a_i, b_i, and c_i correspond to the thicknesses of the cytoplasm, cell membrane, and cell wall along each principal axis (x, y, z). The conductivity of the suspending medium was varied from 1 x 10^{-4} (DI H_2O) to 2 S/m (0.01 M phosphate buffered saline; NaCl 0.138 M, KCl 0.0027 M). The CM factor as a function of frequency for *E. coli* in different media is shown in Fig. 4.4a. Bacterial cells experience pDEP only in low media conductivity (10^{-4} to 10^{-2} S/m), as no COFs are displayed in the frequency range of 10^2 to 10^7 Hz (100 Hz to 10 MHz). When the media conductivity is increased to 0.1 S/m, a single COF at 8.31 x 10^5 Hz is observed, indicating that *E. coli* cells can be subjected to either pDEP or nDEP in the low or high frequency regimes, respectively. In further increasing the media conductivity to a level such as PBS buffer (σ_m = 1 – 2 S/m) however, only the nDEP regime is accessible to *E. coli* cells as no COFs are displayed in the frequency range of 10^2 to 10^7 Hz (100 Hz to 10 MHz). Therefore, the DEP-SERS device can

generate pDEP or nDEP on *E. coli* cells with proper manipulation of the media conductivity (Fig. 4.4a).

To test the trapping ability of the DEP-SERS device on *E. coli* cells, similar flow experiments were conducted as described for the PS microspheres. *E. coli* cells were injected into the DEP-SERS device with a concentration of 10^5 CFU/mL suspended in DI H_2O at a fixed flowrate of 1 μL/min and 5 V_{pp} applied potential, while the frequency was varied from 500 Hz – 10 MHz. DEP was applied for 5 min at each frequency, and the number of cells collected on the point electrode was monitored. Figure 4.4b shows the number of trapped *E. coli* cells as a function of frequency plotted with the theoretical CM factor. Approximately 500 bacterial cells traverse the microchannel during the 5 min collection. The applied 500 Hz frequency trapped the highest of any of the frequencies tested, with an 18.2% trapping efficiency. As can be seen in Fig. 4.4b, the number of trapped cells follows the same trend as predicted by the theoretical CM factor (ε_m = 78.5, $\sigma_m = 10^{-4}$ S/m). The number of adsorbed cells decreased as the applied frequency increased. The largest applied frequency, 10 MHz, achieved a 3.0% trapping efficiency. In this experimental setup, the applied frequency, and thus the value of the CM factor, led to different trapping efficiencies due do reduction in the DEP force. Excellent agreement was observed between the theoretical predictions and experimental results, indicating successful imposition of pDEP on the *E. coli* cells in the DEP-SERS device.

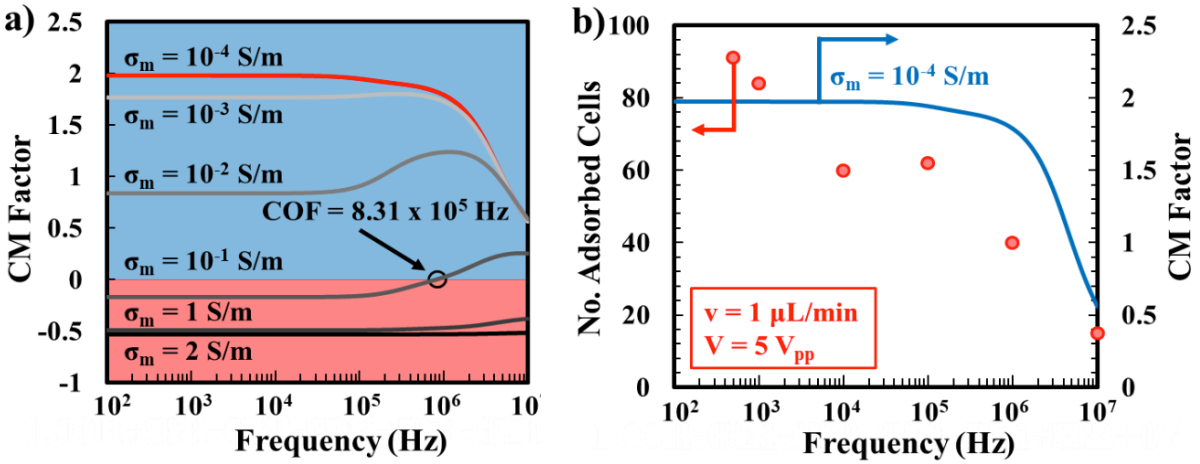

Figure 4.4. a) CM factors as a function of frequency for an *E. coli* cell in media of different conductivities. The media conductivities from top to bottom are as follows: 1 x 10^{-4} (DI H_2O), 1 x 10^{-3}, 1 x 10^{-2}, 1 x 10^{-1}, 1, and 2 (PBS buffer) S/m. b) Number of *E. coli* cells trapped and CM factor versus frequency. Cells were suspended in DI water (10^5 CFU/mL) at a 1 µL/min flowrate, and subjected to a 5 V_{pp} with an applied frequency that ranged 500 Hz – 10 MHz.

4.3.3 *Dynamic Detection of E. coli Under Diffusion-Limited and DEP-Enhanced Microfluidic Conditions*

The temporal SERS response of diffusion-limited transport (i.e. no external DEP) was compared to the response of DEP-enhanced transport of *E. coli* cells conducted in the DEP-SERS microfluidic biosensor. SERS signals were dynamically collected as bacterial suspensions were introduced in the microfluidic channel. Throughout collection, the 785 nm laser was held in a fixed location on the Q3D array. The intensity of the 752 cm^{-1} band, is plotted in Fig. 4.5a as a function of time, and the representative SERS spectra are shown in Fig. 4.5b. The 752 cm^{-1} is assigned to the phospholipid bilayer that encapsulates Gram-negative bacteria such as *E. coli*.[41, 143] Initially, the *E. coli* suspension (10^5 CFU/mL in DI H_2O) was injected at 1 µL/min without the application of DEP for 40 min, and ~2 x 10^3 cells traversed the microfluidic channel. In this regime, diffusion governs mass transport of cells to the Q3D plasmonic nanostructured arrays located at the bottom plate of the microfluidic channel. As can be seen in Fig. 4.3a, the SERS intensities are weak, and show no noticeable increase during the 40 min time period. This

suggests a lack of cellular adsorption on the Q3D arrays due to the relatively low cell concentration, and confinement of bacterial cells in the center of the microchannel. Optical imaging confirmed the lack of cellular adsorption after the 40 min diffusion-limited window (Fig. 4.6). In previous work utilizing Q3D substrates for bacterial analysis, it had been shown that bacteria concentrations of 10^8 CFU/mL in static (i.e. no fluidic flow) Q3D measurements are easily collected due to high cell adsorption after a 20 min incubation.[83] However, when the concentration was reduced to 10^5 CFU/mL, SERS measurements were unsuccessful due to the lack of cell adsorption on the Q3D array,[41] which is in good agreement with the resulted observed here.

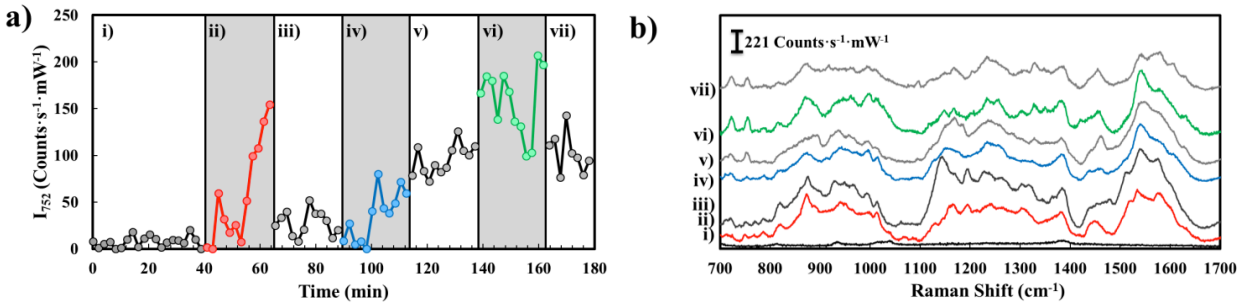

Figure 4.5. a) Temporal response of the 752 cm^{-1} band of *E. coli* suspended in DI H_2O with 10^5, 10^7, and 10^8 CFU/mL at a constant flowrate of 1 µL/min with and without the application of DEP at 500 Hz and 5 V_{pp}. b) Representative SERS spectra from each segment of the temporal response. The conditions for the seven segments are as follows: i) DEP-off, DI H_2O; ii) DEP-on, 10^5 CFU/mL; iii) DEP-off, DI H_2O; iv) DEP-on, 10^7 CFU/mL; v) DEP-off, DI H_2O; vi) DEP-on 10^8 CFU/mL; vii) DEP-off, DI H_2O.

A 5 V_{pp} potential at 500 Hz was applied to the DEP-SERS device after the 40 min diffusion-limited time period. This time period is shown as the red segment in Fig. 4.5a, with increasing of the intensity of the 752 cm^{-1} band. Immediate cellular adsorption (Fig. 4.6b) and intensity increase were observed, and the SERS intensity increased until the 60 min time point when the applied potential was removed. The bacterial concentration was increased to 10^7 and 10^8 CFU/mL, and allowed to flow through the device for ~20 min without the application of DEP and then 20 min with the application of DEP in sequence. It can be seen in Fig. 4.5a that the

average intensities of the 752 cm^{-1} band in the DEP regions for each concentration are higher than those without DEP, indicating that pDEP forces act on *E. coli* cells and enrich cells on the SERS-active substrates on the point electrode. We also noticed that the average intensity of the 752 cm^{-1} band increased with increasing concentration of bacteria. This is mainly due to the enhanced mass diffusion at higher concentrations. Turning off DEP and continue flowing 10^8 CFU/mL *E. coli* aqueous solution, the average intensity of the 752 cm^{-1} band returned to the similar level as first flowing of the same concentration bacterial solution, which further demonstrates the trapping of *E. coli* cells on the point electrode due to pDEP forces. Because the laser spot area (2 μm x 25 μm) was smaller than the Q3D array (50 μm x 50 μm) and held in a fixed location, it is possible that the number of bacterial cells within the laser spot differed from the rest of the array and varied with time, leading to fluctuations of the SERS intensity with respect to bacterial concentration.

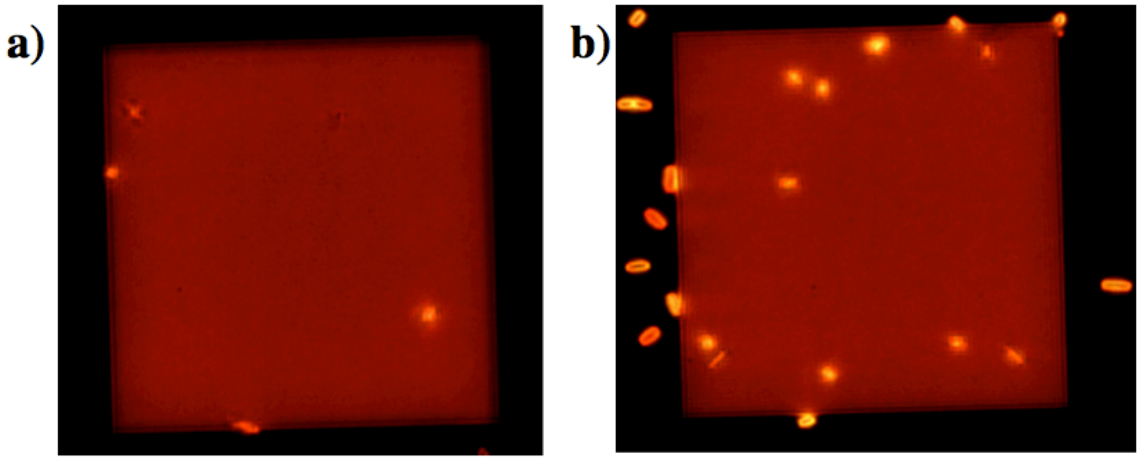

Figure 4.6. High-resolution images of a single Q3D after a) 40 min without application of DEP and b) 1 min application of DEP at 500 Hz and 5 V_{pp}. The bacterial suspension was 10^5 CFU/mL in DI H_2O, and was introduced into the DEP-SERS microfluidic biosensor at 1 μL/min.

4.3.4 *Effect of Applied DEP Frequency on Bacterial SERS Spectra*

In order to investigate the effect of the applied DEP frequency on bacterial cells, the SERS spectra of *E. coli* and *S. epidermidis* were collected at frequencies ranging from 500 Hz to

10 MHz, and statistically analyzed with principal component analysis (PCA). *E. coli* and *S. epidermidis* were chosen due to the differences in their biochemical makeup. *S. epidermidis* is a Gram-positive, spherical bacterium with a cell wall composed primarily of teichoic acids covalently bonded to a thick peptidoglycan layer.[144] The Gram-negative *E. coli* is rod-shaped with a cell wall that is comprised of lipopolysaccharides. Concentrated *E. coli* or *S. epidermidis* suspensions (10^8 CFU/mL) in DI H_2O were flowed to completely fill the microchannel chamber, and incubated for 20 min to allow settling of the bacterial cells to the surface. SERS spectra were collected with no applied DEP and in the frequency range of 500 Hz – 10 MHz at 5 V_{pp}. In DI H_2O (σ_m = 10^{-4} S/m), *S. epidermidis* will experience pDEP only (Fig. 4.7). Therefore, the entire frequency range (500 Hz – 10 MHz) was available to collect SERS spectra of *S. epidermidis*, as the *S. epidermidis* cells were attracted to the point electrode through pDEP. The averaged SERS spectra of *E. coli* and *S. epidermidis* without DEP and with DEP under different frequencies are shown Fig. 4.8a and b, respectively. Clear spectral differences are observed for the bacterial species.

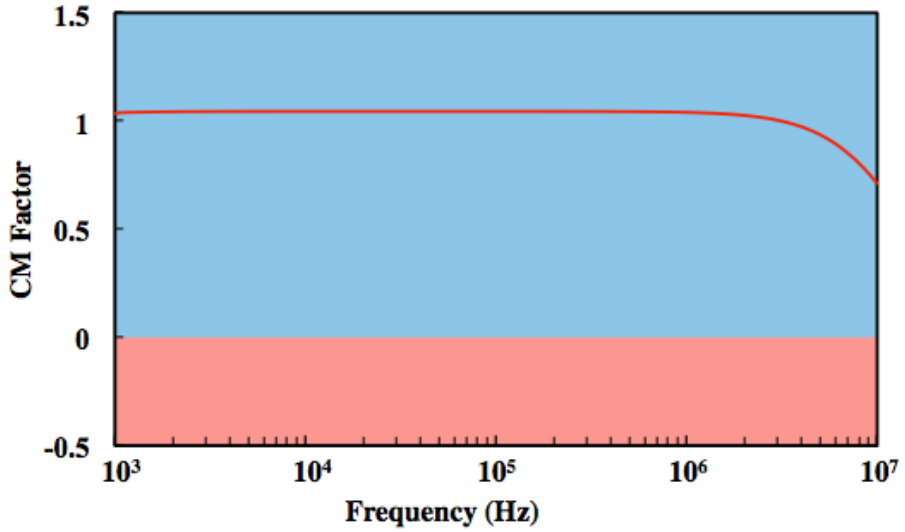

Figure 4.7. Clausius-Mossotti factor for an *S. epidermidis* bacterial cell suspended in a background medium with conductivity of 10^{-4} S/m (DI H_2O).

The near-field effect of SERS results in vibrational information from the peripheral layers of the bacterial cells. The SERS spectra of *E. coli* exhibited Raman bands at 752, 845, 1125, 1216, 1349, 1444, and 1609 cm^{-1} (Fig. 4.8a). Strong peaks in the *S. epidermidis* SERS spectra are observed at 736, 928, 1147, and 1609 cm^{-1}, with weaker bands at 855, 1322, 1345, and 1454 cm^{-1} (Fig. 4.8b). SERS band assignments are summarized in Tables 4.1 and 4.2 for *E. coli* and *S. epidermidis*, respectively. Principal component analysis was employed to determine if application of DEP induced frequency-dependent variation in the bacterial SERS spectra.

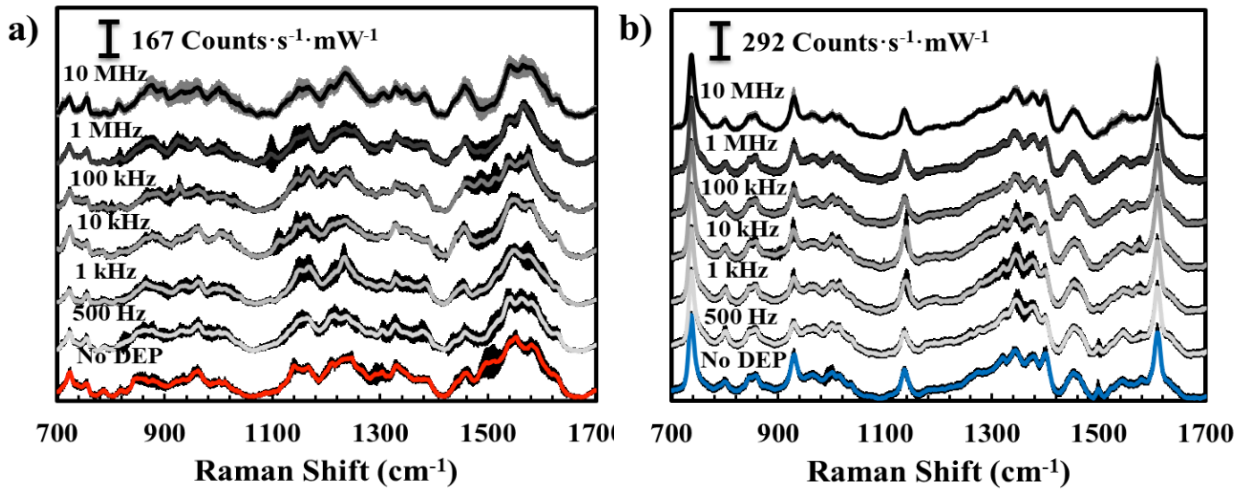

Figure 4.8. Baseline subtracted and normalized SERS spectra of a) *E. coli* and b) *S. epidermidis*. Spectra were collected with 2 accumulations and a 10 s exposure with a 785 nm NIR laser focused through a 50x objective (0.5 mm WD, 0.8 NA) forming a 2 μm x 25 μm spot on the Q3D plasmonic nanostructured array and laser power of 1.2 mW. Each trace is an average of 19 individual collections for *E. coli* and 10 for *S. epidermidis*. Bacterial suspensions (1 x 10^8 CFU/mL) were introduced in the DEP-SERS microfluidic biosensor, and DEP was applied at 5 V_{pp} for frequencies in the range of 500 Hz to 10 MHz. SERS spectra were collected from different spatial locations to generate averaged bacterial signals over the surface of the Q3D array.

The PCA results of the *E. coli* dataset are shown in Fig. 4.9a for the frequency dependent SERS measurements. Contained within this dataset are 133 spectra collected at 7 distinct DEP frequencies. The first PC was able to account for 23% of the variance, with 12% of the variance explained by the second PC. Figure 4.8a exhibits no identifiable 'clustering' of data points with

respect to the applied DEP frequency, suggesting the SERS spectra for *E. coli* are independent of the applied DEP frequency. The PCA revealed that 15 principal components are required to account for 81% of the variance in the data (Fig. 4.9d). The PCA for *S. epidermidis* exhibited non-clustering PC scores with respect to frequency as shown in Fig. 4.9b. Here, 33% of the variance was explained by PC1 and 11% by PC2, with 15 PCs accounting for 76% of the variance (Fig. 4.9d).

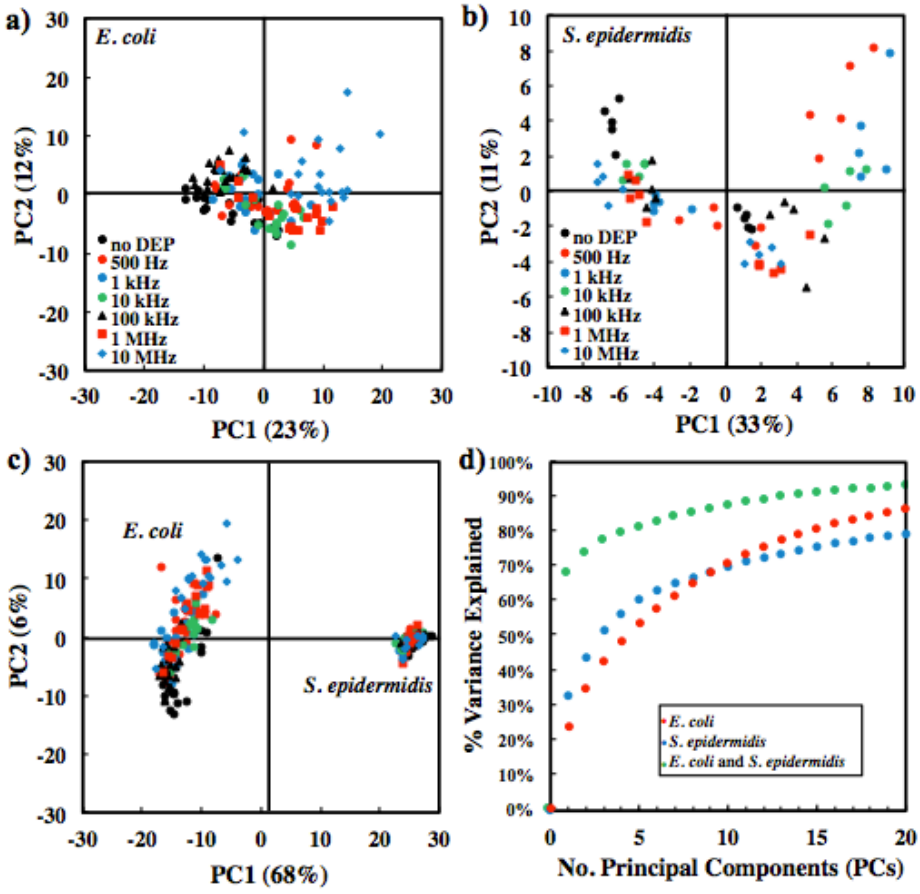

Figure 4.9. Principal component analysis of *E. coli* and *S. epidermidis* SERS spectra collected on Q3D plasmonic nanostructured arrays at different DEP frequencies. Two-dimensional PCA plots produced using the entire SERS spectrum for a) 19 spectra for each frequency for *E. coli*, b) 10 spectra for each frequency for *S. epidermidis*, and c) the combined *E. coli* and *S. epidermidis* datasets. d) Scree plots showing the percentage of the variance explained for each dataset.

Figures 4.9a and b suggest that the SERS spectra of bacterial cells, whether Gram-positive or Gram-negative, are not influenced by the presence of the external DEP field in the

DEP-SERS microfluidic biosensor. The spectral invariance would indicate that the cellular structure was unaffected by the application of DEP. Long DEP exposure times were shown to decrease cell viability in the Gram-positive bacterium, *Listeria monocytogenes*.[140] Exposure times of < 1 h did not decrease cell viability, and decreased cell viability was only observed in *L. monocytogenes* for exposure times ≥ 4 h. Large voltage potentials (20 V_{pp}) in highly conductive media decreased cell viability by ~90%.[140] The application of DEP used here (5 V_{pp}, in DI H_2O) for timescales < 20 min, should avoid the detrimental effects on cellular viability. Furthermore, large spectral differences in the SERS signatures would be expected if the application of DEP used in this study led to cell death.[145]

Table 4.1. SERS band assignments for *E. coli*.

Band	Assignment	Ref
752	ν O-P-O	1
845	ν CC, tyrosine	1,2
1125	ν CC (lipids) ν CN (proteins)	1,3
1216	amide III	1-4
1349	amide III	4
1444	δ CH_2 (proteins)	1-4
1609	phenylalanine	1,2

δ: deformation vibration, ν: stretching vibration, ρ: rocking vibration

Table 4.2. SERS band assignments for *S. epidermidis*.

Band	Assignment	Ref
736	ρ (CH_2)	5
855	ν CC (ring breathing) ν CC (1,4-glycosidic link)	5
928	ν CC (proteins)	1
1147	ν CN (proteins) ν COC (symmetric glycosidic link)	1,5
1322	δ CH (proteins)	5
1345	δ CH (proteins)	5
1454	δ CH_2 (scissoring)	5

1609	phenylalanine	1,2

δ: deformation vibration, ν: stretching vibration, ρ: rocking vibration

The SERS spectra are readily identified when PCA is applied to the combined dataset that contains spectra from both *E. coli* and *S. epidermidis* (Fig. 4.9c). The PC scores for *E. coli* and *S. epidermidis* produced a high degree of clustering, with 68% of the variance explained by PC1 (Fig. 4.9d). No clustering from the distinct DEP frequency conditions were observed within the species-level clusters, which are in good agreement with the PC plots in Figs. 4.9a and b.

Multivariate classifiers were employed to further investigate the influence of the applied DEP frequency on the SERS spectra. Three classifiers, kNN, LDA, and SVM, were trained using DEP collection frequencies as predictors. The SERS datasets of *E. coli* and *S. epidermidis* were split 90/10 into training and predicting sets, respectively. The accuracies of the classifiers were defined as the percentage of SERS spectra correctly identified at a given frequency. The results of the multivariate classification analysis for the bacterial cells are given in Table 4.3.

Table 4.3. Summary of the multivariate analysis with kNN, LDA, and SVM classifiers. The reported accuracies are defined as the number of correctly classified SERS spectra divided by the total number of SERS spectra attempted to classify. The total number of spectra collected at each frequency were 19 and 10 for *E. coli* and *S. epidermidis*, respectively. A 90/10 split was used for the training and classifying datasets, respectively.

Classifier	**4-MPBA**	***E. coli***	***S. epidermidis***	**Combined**
kNN	42.86%	87.50%	57.14%	100.00%
LDA	0%	50.00%	71.43%	100.00%
SVM	9.82%	68.75%	42.86%	100.00%

The most accurate classification was performed by kNN analysis on the *E. coli* dataset, with an 87.5% accuracy. kNN and SVM analyses more accurately predicted the *E. coli* datasets over the *S. epidermidis* datasets, whereas LDA was more accurate for *S. epidermidis*. These classifiers have been shown to differentiate SERS spectra of bacterial samples with minute differences with accuracies as high as 95%.[146] Therefore, the classification analysis can

reinforce the PCA to demonstrate the SERS spectral independent with respect to applied DEP frequency. As a control, the datasets were combined, and the bacterial strains (regardless of applied DEP frequency) were used as predictors for the classifiers. All three classifiers were able to predict the unknown spectra with 100% accuracy due to the inherent uniqueness of the SERS spectra of *E. coli* and *S. epidermidis* (Table 4.3).

An ideally independent correlation between the applied DEP frequency and SERS spectra would result in prediction accuracies of 0%. However, the prediction accuracy ranges of 50.0 – 87.5 and 42.9 – 71.4% for *E. coli* and *S. epidermidis*, respectively, are much lower than previous reports. Furthermore, it is believed that some of the spectral variation leading to higher prediction accuracies is attributable to temporal processes by the cells. It is well known that SERS spectra of bacteria change with time due to excretion of intracellular molecules and/or subtle changes to the cell wall.[143] Therefore, it is believed that these processes contributed to increased prediction accuracy. The higher metabolic rate of *E. coli* therefore resulted in a higher accuracy compared to the less metabolically active *S. epidermidis*.

A self-assembled monolayer of 4-mercaptophenyl boronic acid (4-MPBA) was formed on the Q3D surface in order to decouple the temporal fluctuations of the cellular processes from the influence of the applied DEP frequency. This experiment can also assess the influence of the applied DEP frequency on the electromagnetic enhancement induced by LSPR on plasmonic nanostructures. SERS spectra were then collected under no DEP and applied DEP with 5 V_{pp} and frequency raged from 500 Hz – 10 MHz. The spectra are shown in Fig. 4.10a. PCA revealed no clustering of the SERS spectra with respect to the applied DEP frequency (Fig. 4.10b). The first and second PCs were found to account for 32 and 13% of the variance present in the data, respectively, and 15 PCs accounted for 71% of the variance (Fig. 4.10c). Successful

identification rates of 4-MPBA SERS spectra at different applied DEP frequencies of 42.86, 0, and 9.82% were obtained for the kNN, LDA, and SVM classifiers, respectively (Table 4.3). Therefore, the spectral invariance with respect to the applied DEP frequency displayed by the DEP-SERS revealed that DEP does not induce the complication of 'floating' SERS signals (i.e. SERS spectra that change with respect to the applied DEP frequency).

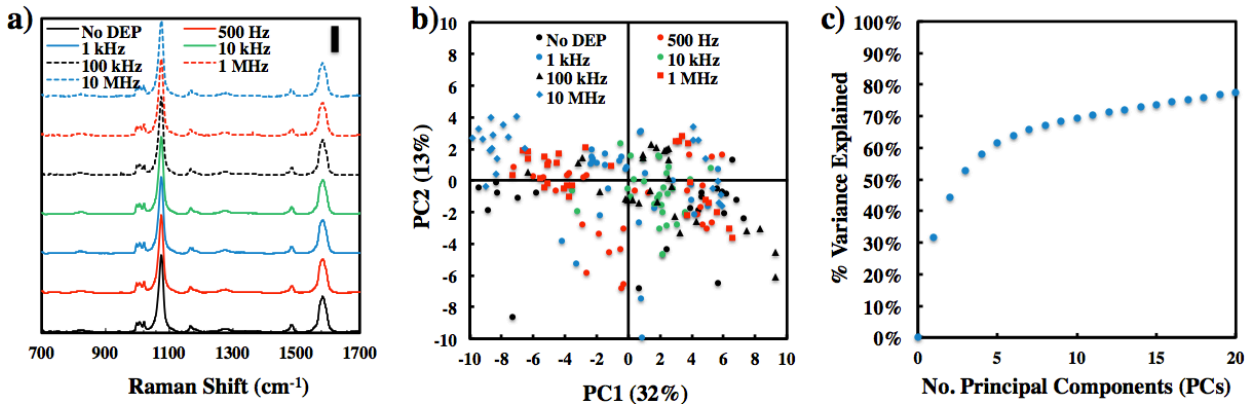

Figure 4.10. a) Normalized SERS spectra of 4-MPBA SAM on the Au surface of Q3D plasmonic nanostructured arrays collected at discrete DEP frequencies. The scale bar represents 750 counts s^{-1} mW^{-1}. b) Principal component analysis of the SERS spectra of 4-MPBA SAM collected on Q3D plasmonic nanostructured arrays at discrete frequencies. c) Variance accounted for as a function of the number of principal components.

4.4 CONCLUSIONS

In summary, we present the development of a SERS-based, microfluidic biosensor that utilizes DEP to promote cellular migration to the sensing surface at the bottom of the microchannel. The DEP-SERS microfluidic biosensor was found to trap PS microspheres and *E. coli* cells with a frequency dependence in good agreement with the theoretically calculated CM factors. The temporal response of the SERS signal of *E. coli* was studied in microfluidic flow conditions, and the responses of the diffusion-limited and DEP-enhanced regimes were compared. Moreover, the SERS spectral dependence on the applied frequency for the Gram-positive and Gram-negative bacteria was investigated with multivariate analysis. PCA displayed no clustering patterns of either category of bacteria with respect to the applied DEP frequency.

Furthermore, successful identification rates ranging from 42.9 – 87.5% were observed for kNN, LDA, and SVM classifiers. Combined the multivariate analyses suggest that SERS spectral characteristics and 'hot-spot' intensities are unaffected by the application of external DEP electrical fields. The strategy developed here could enable rapid, label-free detection of bacteria, while eliminating the need for time-consuming plate culturing detection methods.

Chapter 5. IMPROVED MASS TRANSPORT IN SURFACE PLASMON RESONANCE (SPR) BACTERIAL DETECTION VIA DIELECTROPHORETIC ENHANCEMENT

5.1 INTRODUCTION

Bacterial infections are commonplace worldwide. The increased prevalence of bacterial infections has resulted in the over prescription of wide-spectrum antibiotics, and a dramatic decrease in the efficiency of antibiotic treatment.[118, 120] In the United States alone, ~2 million cases of bacterial infections exhibiting some degree of antibiotic resistance are reported annually, resulting in ~23,000 deaths.[117, 147, 148] Diagnosis of bacterial infections is predominately performed by time-consuming and expensive plate culturing methods. The development of novel technologies is required to reduce diagnosis times, and thus alleviate antibiotic pressure on bacteria leading to resistance.

Surface plasmon resonance (SPR) is one such biosensing technology that is well suited for bacterial detection. SPR-based biosensing capitalizes on the coupling of incident light to surface plasmons (SPs) on metal/dielectric interfaces.[39] SPs are generated when the momentum of the electric component of incident light matches that of the free electron plasma of the metal. Two critical lengths define the SPs, and how they interact with the surrounding dielectric environment: the propagation length, which is the average distance SPs propagate along the metal/dielectric interface, and the penetration depth, the distance above the metal/dielectric interface at which the SP electric field intensity decays by a factor of 1/*e*. While both characteristic lengths are dependent on the specific excitation wavelength, metal film properties, and dielectric medium, typical ranges for the propagation length and penetration depth in the 650 – 830 nm spectral window are 3 – 20 μm and 162 – 400 nm, respectively.[18] SPs are sensitive to

the dielectric environment near the interface. Local changes in the refractive index of the medium directly above the metal/dielectric interface induce shifts in the SPR wavelength, and with proper experimental setup, the SPR wavelength shift can indicate a specific biorecognition event (e.g. adsorption of bacteria on the surface). The magnitude of the shift can be used to quantify the concentration and identify the target bacteria.

The performance of SPR bacterial biosensors is directly related to the efficiency at which bacterial cells are brought into the effective sensing volume of the SP evanescent wave. SPR biosensing can suffer from undesirably high limits of detection (LOD) due to inherent performance limitations originating from: (1) the ~300 nm penetration depth, and (2) diffusion-limited mass transport of bacterial cells to the metal/dielectric interface. Multiple strategies have been explored to improve the LOD in SPR-based bacterial detection. Sandwich-type assays provide secondary amplification of the SPR signal through further alteration of the local dielectric environment, and have been shown to improve the LOD.[149-151] Long-range SPR (LR-SPR) biosensors were developed to extend the penetration depth from ~300 nm to approximately the diameter of bacterial cells (~1 μm).[61, 152, 153] Increased coverage of the bacterial cells by the LR-SPR evanescent wave led to 5.5-fold increase in SPR response for detection of *E. coli* HB101P.[61] However, most SPR bacterial biosensing is performed in microfluidic channels with a critical channel height of ~50 μm. Therefore, the majority of the microchannel, and thus bacterial cells, remain inaccessible to the SP evanescent wave; further hindering detection performance.

SPR bacterial biosensors are often operated in the diffusion-limited regime, which can further limit device performance. Of the key kinetic processes that bacterial cells experience in the microchannel which include convection through the length of the microchannel, diffusion from the bulk fluid to the sensing surface, and reaction at the sensing surface, diffusion is often

the slowest process.[51] For dilute suspensions in the clinically relevant range (< 10^5 CFU/mL), the majority of target cells transverse the microchannel without adsorption on the sensor surface. Therefore, it is desired to increase mass transport of bacterial cells to the metal/dielectric interface for efficient detection. Magnetic nanoparticles (MNPs) have been the predominant mechanism explored in SPR biosensing to increase bacterial mass transport.[44, 154, 155] MNPs are typically functionalized with antibodies or aptamers to selectively bind the target cells, and application of an externally applied magnetic field drives mass transport of MNP-bacteria complexes to the sensing surface. One unexplored avenue that holds potential to overcome diffusion-limited mass transport and improve the LOD performance in SPR bacterial detection is dielectrophoresis (DEP).

DEP is the movement of dielectric particles (i.e. bacterial cells) in the presence of an asymmetrical electric field.[156] The dielectrophoretic force exerted on the particle is dependent on the size of the particle, conductivity of the suspending medium, square electric field gradient, and the frequency of the applied AC potential.[129] In the presence of inhomogeneous electric fields, particles will migrate towards regions where the electric field gradient is maximized or minimized in positive DEP (pDEP) and negative DEP (nDEP), respectively. Properly designed DEP-active electrodes can therefore lead to biosensing signal enhancement through spatial modulation of bacterial cells. DEP has been successfully incorporated into various bacterial biosensing strategies including electrochemical impedance spectroscopy,[157-160] fluorescence microscopy,[161-163] Raman spectroscopy,[130, 164, 165] and surface-enhanced Raman scattering.[71, 126, 127, 166]

Therefore, we speculated that DEP could be incorporated into the SPR sensing strategy to overcome diffusion-limited mass transport, and increase detection efficiency of bacteria. In this

work, we report the development of a DEP-SPR bacterial detection technique with dually functional interdigitated electrodes (IDEs) on SPR chips, henceforth referred to as interdigitated-SPR chips or "iSPR chips". The iSPR chips were optimized to sustain strong SPR, while simultaneously providing increased mass transport of bacterial cells to the sensing surface through DEP. SP generation was found to be dependent on electrode width, with efficient SP generation occurring on IDEs with widths larger than the SP propagation length. The inherent sensitivity to bulk changes in the refractive index of the sensing medium for the iSPR chip was compared against a conventional (i.e. continuous, Au film) SPR chip. The two types of SPR chips generated nearly identical SPR shifts for changes in refractive index of 0.00125 RIU. Conventional and iSPR chip surfaces were functionalized with mannose to target the FimH adhesin of *E. coli*, and increase cellular adhesion. The DEP-SPR method enabled a nearly five orders of magnitude improvement in the LOD for *E. coli* suspensions compared to the conventional SPR biosensor, improving the LOD from 1.0 x 10^7 CFU/mL to ~3.0 x 10^2 CFU/mL. Furthermore, selective detection of target *E. coli* over non-target *S. epidermidis* bacteria was enabled through secondary antibody amplification. The results presented here indicate a great potential of the incorporation of DEP into SPR biosensors for rapid, sensitive, and specific detection of bacteria with broad applications in the areas of biomedical diagnostics, environmental monitoring, food safety, and homeland security.

5.2 EXPERIMENTAL

5.2.1 *Materials and Reagents*

Potassium hydroxide, potassium thiosulfate, potassium ferricyanide, potassium ferrocyanide, octadecane thiol (ODT), 11-mercaptoundecanoic acid (MUA), sodium chloride, tryptone, yeast extract, trichloro (1H, 1H, 2H, 2H-perfluorooctyl) silane (TCPFOS), 1-ethyl-3-[3-

dimethylaminopropyl]carbodiimide HCl (EDC), N-hydroxysuccinimide (NHS), and bovine serum albumin (BSA) were purchased from Sigma-Aldrich (St. Louis, MO). 1-deoxy-1-aminomannopyranoside (DAMP) was purchased from Santa Cruz Biotechnology. Sylgard 184 polydimethylsiloxane (PDMS) and curing agent elastomer kit were purchased from Dow Corning (Midland, MI). *Escherichia coli* (ATCC 25922) and *Staphylococcus epidermidis* (ATCC 14990) were purchased from American Type Culture Collection (Manassas, VA). Rabbit anti-*E. coli* polyclonal antibodies (PA1-7213) were purchased from Invitrogen. All chemicals were used as received.

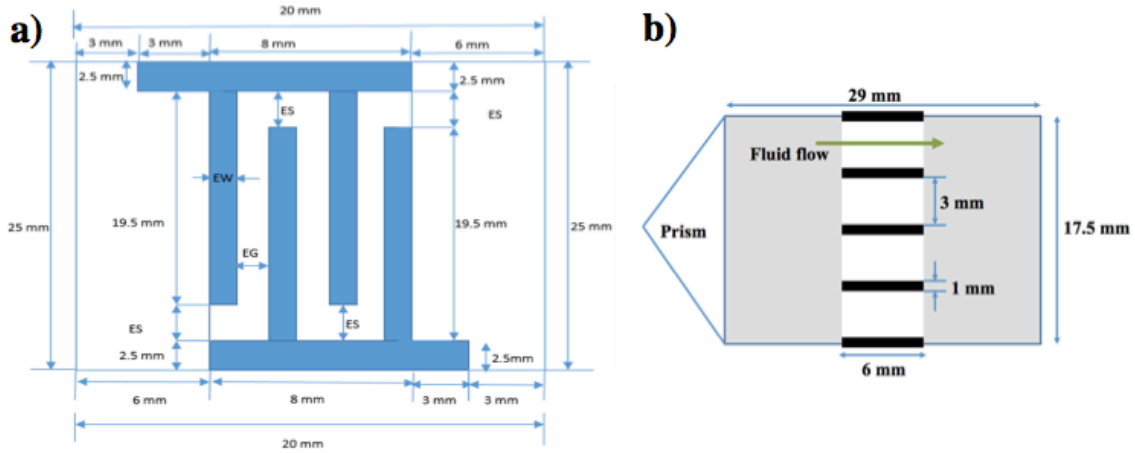

Figure 5.1. Detailed dimensions of the a) IDEs and b) microfluidic channels used in the present study. a) The electrode spacing (E_S) and electrode gap (E_G) were held constant at 500 and 5 µm, respectively. The electrode widths (E_W) used in this study were 10, 20, and 100 µm. IDEs were oriented such that the 19.5 mm electrode arms were perpendicular to the fluid flow. b) The Mylar gasket (black) defined the dimensions of the microchannels with length, width, and height of 6 mm, 3 mm, and ~50 µm, respectively. The total width (8 mm) and length (19 mm) of IDEs are longer than the channel length (6 mm) and total width (15 mm) of four channels to ensure the entire fluid channels experienced DEP.

5.2.2 *Fabrication of Interdigitated Electrodes on SPR (iSPR) Chips*

iSPR chips were fabricated through a series of photolithography, soft lithography, and chemical etching steps. IDE patterns were first developed into a ~3 µm SU-8 film on a silicon wafer using photolithography. Three patterns were resolved on the SU-8 master mold with a fixed electrode gap (E_G) of 5 µm and electrode widths (E_W) = 10, 20, and 100 µm. A detailed

schematic for the electrode configurations can be seen in Fig. S1. Prior to PDMS casting, the master mold was desiccated with TCPFOS for 1 h. PDMS and curing agent were mixed in a 10:1 ratio, poured over the master mold, and allowed to cure at 60°C for 4 h. The PDMS replicates were then peeled from the master mold and diced into individual stamps. The stamps were coated in a 2 mM ethanolic ODT solution, and brought in contact with the Au surfaces of SPR chips (2 nm Cr, 48 nm Au on glass substrates) for ~15 s; leaving a patterned self-assembled monolayer (SAM) of ODT. The SPR chips were then immersed in a previously described[103] Au etching solution consisting of 1 M KOH, 0.1 M $K_2S_2O_3$, 0.01 M $K_3Fe(CN)_6$, and 0.001 M $K_4Fe(CN)_6$ for 20 min to remove regions of the Cr/Au film unprotected by the ODT SAM. The etching reaction was quenched by immersion of the SPR chips in fresh DI H_2O. A representative schematic for the fabrication process is given in Fig. 5.2.

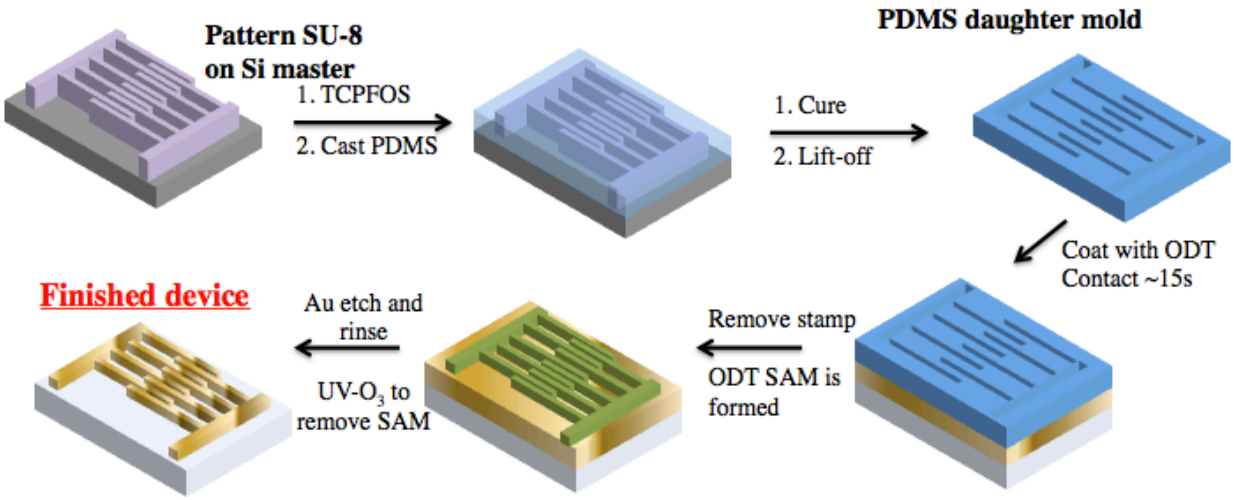

Figure 5.2. Schematic illustration for the fabrication protocol used to resolve Au IDEs on glass substrates.

5.2.3 *SPR Resolution of iSPR Chips*

All SPR experiments were performed with a custom-built, four-channel device that has been previously described.[167] Briefly, the prism-coupled instrument was constructed in the Kretschmann configuration to provide attenuated total reflection, and operated with wavelength

modulation. A broadband, halogen-lamp light source (Ocean Optics, HL-2000) was collimated, polarized, and passed through a BK7 glass prism before collection into four separate optical fibers coupled to a spectrophotometer. The illumination area was approximately 1 mm x 17.5 mm. The sensor had a wavelength resolution of 0.001 nm.[168] The four microfluidic channels were defined by a Mylar gasket to have lengths, widths, and heights of 6 mm, 3 mm, and 50 μm, respectively, with the IDEs on iSPR chips oriented perpendicular to the direction of fluid flow (Fig. S1). Fluid volumetric flowrates were controlled by a peristaltic pump (Ismatec, C.P. 78001-00), and were varied from 5 – 50 μL/min. The length of the inlet tubing were ~22 in, causing a delay of ~5 min for the solutions to reach the sensor surface at a flowrate of 10 μL/min. A temperature controller (ILX Lightwave, LDT-5525) was integrated into the SPR device to maintain accurate temperature control in the range of 25 – 40^{o}C.

Conventional and iSPR chips were cleaned with UV-O_3 plasma treatment, and fresh ODT SAMs were formed on the surfaces. The chips were mounted in the SPR instrument with the iSPR chips mounted such that the electrode arms were perpendicular to the direction of fluid flow and the propagation of SPs (Fig. S1b). DI H_2O was introduced into the fluid chamber with a 10 μL/min flowrate. Reflectivity spectra were collected using the optical path described in the previous section. Additionally, the reflectivity spectra were collected for iSPR chips rotated 90^{o}, such that the electrode arms were oriented in the direction of SP propagation.

5.2.4 *Characterization of Inherent Sensitivity of iSPR Chips*

Ionic solutions were made by dissolution of NaCl into DI H_2O to achieve concentrations ranging from 6.25 x 10^{-4} – 1 x 10^{0} M. A fixed volumetric flowrate of 50 μL/min was used for all NaCl solutions on conventional SPR and iSPR chips (E_G = 5 μm, E_W = 100 μm), with freshly prepared ODT SAMs. DI H_2O was initially injected into the SPR device for 20 min to establish

the baseline. The flow was stopped, and the inlets were inserted into each NaCl solution for 10 min in increasing concentration. The concentrations were then stepped down, and DI H_2O was reintroduced into the device for 10 min to reestablish the baseline.

5.2.5 *Surface Modification with 1-Deoxy Amino Mannopyranose (DAMP)*

ODT SAMs from freshly prepared iSPR chips were removed with UV-O_3 cleaning for 25 min, followed by an ethanol rinse. The clean iSPR chips were immersed in a 2 mM ethanolic MUA solution for 16 h. EDC and NHS were dissolved in DI H_2O to concentrations of 400 and 40 mM, respectively. iSPR chips were removed from the MUA solution, sequentially rinsed with ethanol and DI H_2O, and dried in a stream of air. The EDC and NHS solutions were poured over the iSPR chips, and gently shaken for 30 min. After 30 min, the iSPR chips were rinsed with DI H_2O, immersed in a 1 mg/mL DAMP solution for 1 h, and rinsed again with DI H_2O. The iSPR chips were immersed in a 1 M glycine deactivating solution for 30 min. Mannosylated iSPR chips were immediately used for SPR detection of *E. coli*.

5.2.6 *Bacterial Culture*

E. coli (ATCC 25922) and *S. epidermidis* (ATCC 14990) samples were received as freeze-dried pellets. The pellets were used to inoculate 5 mL of LB broth at 37^{o}C for 16 h on a shaker plate at 250 RPM. Cell stocks were prepared by dilution (50% by volume) of the inoculate with glycerol. The cell stocks were stored at -80^{o}C, and used throughout the study. Immediately prior to SPR characterization, cell stocks were grown to density. A micropipettor was used to transfer ~2.5 μL of cell stock to 5 mL of LB broth, and grown overnight at 37^{o}C and 250 RPM. The inoculate was added to a 250 mL Erlenmeyer flask with 50 mL fresh LB, and returned to the shaker plate in the warm room. The culture remained in the warm room for ~1 h

until an OD_{600} of 0.6 was reached, corresponding to a concentration of ~1 x 10^8 CFU/mL. The cells were rinsed by three iterations of centrifugation (15,000 x g for 15 min) followed by resuspension in fresh DI H_2O.

5.2.7 *SPR Detection of E. coli with Externally Applied DEP*

Bacterial suspensions were tested immediately after growing to an OD_{600} of ~0.6. Suspensions were adjusted to concentrations of 10^3 – 10^8 CFU/mL in increments of 10^1 CFU/mL in DI H_2O. Sensorgram baselines were established by flowing DI H_2O over the conventional and iSPR chips for 20 min. The volumetric flowrates for all bacterial detections were held constant at 10 µL/min. Bacterial suspensions were introduced into the flow channels of the SPR instrument for 20 min, and switched back for DI H_2O for 20 min. A function generator (Instek, AFG-2225) supplied a 5 V_{pp} voltage potential across the iSPR chips, which was applied simultaneously as the inlets were switched from DI H_2O to bacterial suspensions. The potential was removed when the inlets were switched back to DI H_2O.

5.2.8 *Incorporation of Biorecognition Elements in the Sensing Strategy*

Rabbit anti-*E. coli* polyclonal antibodies (PAb) were used to demonstrate selective detection of target *E. coli* over non-target *S. epidermidis*. The running buffer consisted of BSA dissolved in PBS at 1 mg/mL to block non-specific adsorption sites on the conventional and iSPR chips. PAb was dissolved in the PBS/BSA buffer at a concentration of 50 µg/mL. After detection of *E. coli* on iSPR chips or *S. epidermidis* on conventional chips (described in the preceding section), the inlets were switched to the PBS/BSA buffer for 20 min at 10 µL/min to reestablish the baseline. Three channels were then switched to the PAb-spiked PBS/BSA buffer

for 20 min, while the fourth channel served as a reference. The inlets were switched back to the PBS/BSA buffer for 20 min to remove any unbound PAb.

5.3 Results and Discussions

5.3.1 *Development of DEP-Enhanced SPR System*

Figure 5.3a shows the generalized schematic for the sensing strategy. IDEs on iSPR chips were generated by modifying conventional SPR chips with micron-sized gaps. iSPR chips could then be integrated into the SPR system, which was operated in the Kretschmann configuration to generate attenuated total reflection. The asymmetrical electric fields produced by the IDEs imposed an external force on individual bacterial cells. A laminar flow with a parabolic velocity profile was established in the flow cell, which exerted a drag force on individual cells. IDEs on the iSPR chips were oriented with the electrode arms perpendicular to the fluid flow (Fig. 5.3b). Under proper conditions, the DEP force could overcome the drag force, and drive cellular adsorption on the IDE surface for detection.

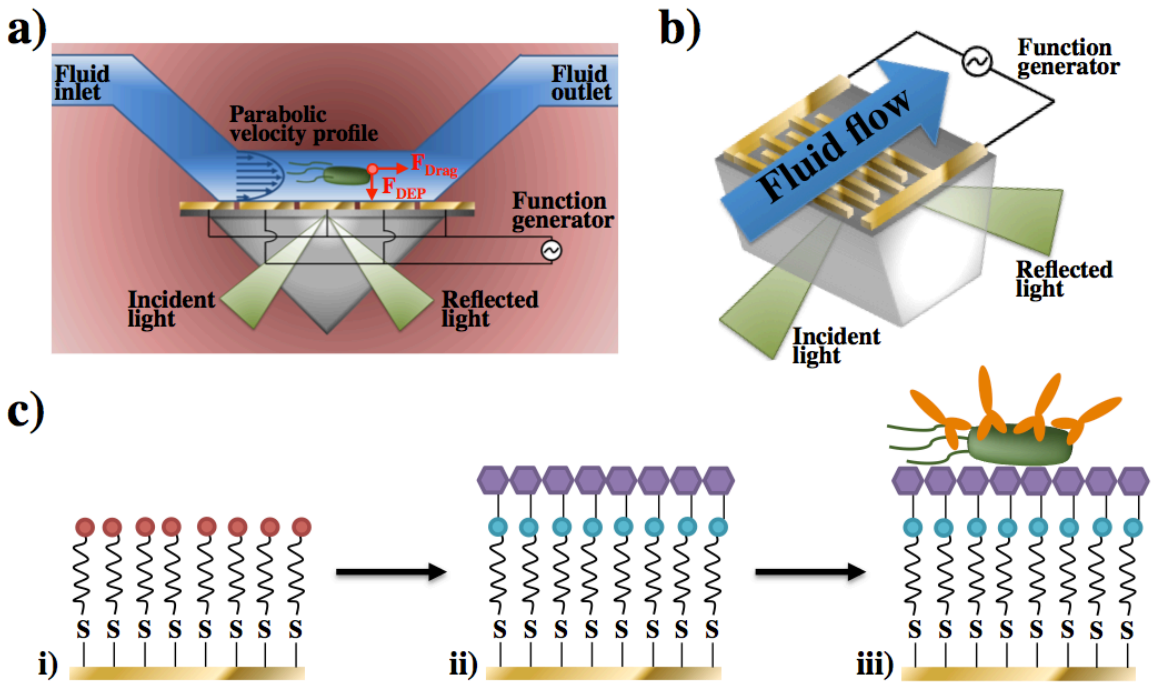

Figure 5.3. a) Schematic illustration of the proposed DEP-SPR device. DEP-active IDEs replace the conventional Au sensing surface (i.e. electrodeless film) in the Kretschmann SPR configuration. Alternating IDEs are connected to a function generator that establishes an AC potential across the IDEs, and generates the necessary asymmetric electric field for DEP. The IDEs induce a dielectrophoretic force on bacterial cells that can overcome the drag force exerted by the fluid on the bacterial cells, and drive bacterial mass transport to the IDE sensing surface. b) IDEs were oriented such that the electrode "arms" were oriented perpendicular to the fluid flow. c) Surface modification with DAMP and detection of *E. coli* scheme: i) 11-MUA SAMs were immobilized on the surface, ii) EDC/NHS chemistry was used to covalently link DAMP to 11-MUA, and iii) *E. coli* adsorbs on the mannosylated surface through interaction of DAMP with the FimH adhesin on *E. coli*, followed by secondary antibody amplification.

IDEs with a fixed electrode gap (E_G) of 5 μm and electrode widths (E_w) of 10, 20, and 100 μm were fabricated on iSPR chips. IDEs enabled investigation of (1) the effect that externally applied DEP has on the generation of SPs, and (2) the influence the imposed dielectrophoretic force has on mass transfer of bacterial cells during SPR-based detection. IDEs were fabricated following previously reported methods using microcontact printing[103] followed by wet etching.[107] ODT SAMs were formed on chip surfaces to investigate the comparative optical responses and inherent sensitivities of conventional and iSPR chips. For *E. coli* detection, mannosylated surfaces were used to improve cellular adsorption on conventional and iSPR chips through interaction of the FimH adhesin with surface-bound mannose, with selective detection enabled by secondary antibody amplification (Fig. 5.3c).[169, 170]

5.3.2 *The Effect of IDE Width on SPR Spectral Resolution*

Figure 5.4a shows the optical images of the Au IDEs on glass substrates with E_G = 5 μm and E_w = 10, 20, and 100 μm, respectively. The reflectivity spectra for the iSPR chips with E_w = 10, 20, and 100 μm were collected, and compared against a conventional SPR chip (Fig. 5.4b). It was desired to determine how the presence of the IDEs affected the resolution of the SPR reflectivity spectra, and the wavelength at which SPR occurred (λ_{SPR}). With DI H_2O as the background medium, all electrodes generated SPR at the Au/H_2O interface. All iSPR chips were

mounted such that the electrode arms were perpendicular to the propagation of SPs (Fig. 5.1b). The coupling efficiency and SP generation exhibited dependencies on E_w. Redshifted reflectivity dips were generated at 769 ± 18 and 774 ± 12 nm, for E_w = 10 and 20 μm respectively, exhibiting broad and shallow reflectivity dips compared to the conventional SPR chip at 751 ± 6 nm. As E_w increased to 100 μm, the reflectivity dip blueshifted to 745 ± 5 nm, and drastically deepened and narrowed. The full-width at half-minimum (FWHM) for E_w = 10, 20, and 100 μm were 147 ± 15, 176 ± 10, and 80 ± 19 nm, respectively, with the conventional producing the most narrow dip of 74 ± 3 nm.

The reduced performance characteristics of iSPR chips with E_w = 10 and 20 μm were attributed to obstruction of SP propagation by the high density of discontinuities in the Au films. SP propagation lengths are dependent on the metal sustaining SP excitation, the dielectric medium directly above the metal, and the wavelength of the incident light. The propagation length of SPs generated at Au/H_2O interfaces, ranges from 3 – 24 μm in the 630 – 850 nm spectral window.[18] Therefore, it is speculated that the high density of discontinuities in the Au films on iSPR chips with E_w = 10 and 20 μm prevented efficient SP propagation, and poor resolution of the reflectivity spectra. For wavelength-modulated SPR sensors, the resolution is dependent on how accurately the reflectance dip can be monitored with the local change in refractive index.[18] iSPR chips with E_w = 10 and 20 μm are therefore rendered nonviable for SPR sensing due to broad, shallow reflectance dips.

To further explore the SPR resolution of iSPR chips (E_w = 10 and 20 μm) with respect to the length of SP propagation, the iSPR chips were rotated 90^o such that the Au electrode arms were oriented in the direction of SP propagation. As seen in Fig. 5.4c, the reflectivity spectra of IDEs rotated 90^o displayed smaller deviations from the reflectivity spectrum of the conventional

device. The orientation-dependent reflectivity spectra further support the claim that the poor SPR resolution on narrow IDEs was attributed to impediment of SP propagation due to the discontinuities present in the Au film.

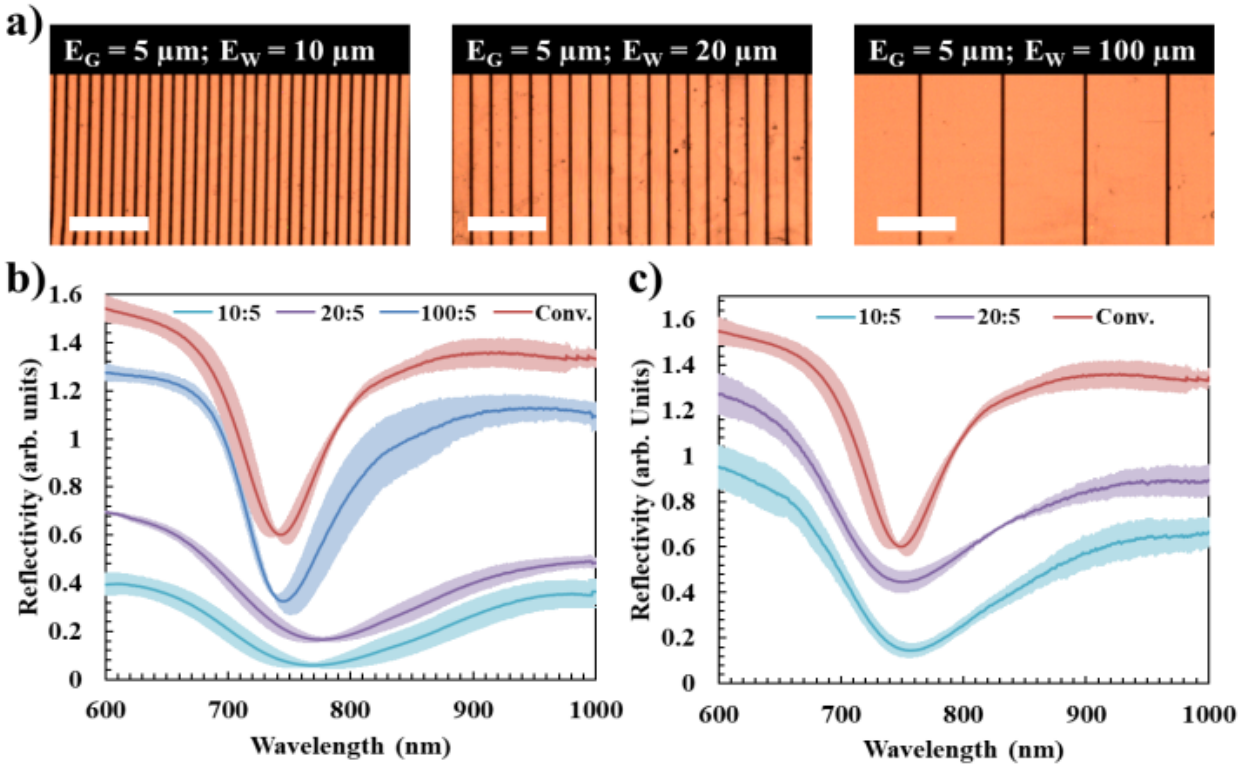

Figure 5.4. a) Optical microscopy images of iSPR chips fabricated from the conventional SPR chips with fixed electrode gaps of 5 µm and electrode widths (E_w) = 10, 20, and 100 µm. b) Reflectivity of the conventional chip (~50 nm Au film), and iSPR chips with fixed electrode gaps of 5 µm and electrode widths (E_w) = 10, 20, and 100 µm. c) Reflectivity of iSPR chips with E_G = 5 and E_W = 10 and 20 rotated 90° (i.e. such that the electrode "arms" are parallel to the fluid flow depicted in Fig. 5.3b). The error bars represent the standard deviations from reflectivity measurements from the four sensing channels integrated in the SPR instrument. Note: reflectivity spectra have been vertically shifted for clarity.

5.3.3 *Inherent Sensitivity to Bulk Refractive Index Variations on iSPR Chips*

The iSPR chip (E_w = 100 µm) was further characterized relative to the conventional SPR chip to determine if the discontinuities produced by the electrode gaps in the Au film of the iSPR chip hampered the inherent sensitivity to changes in the refractive index of the dielectric medium. Figure 5.5a shows the temporal response of the conventional and iSPR chips to bulk

solution refractive index changes. The refractive indexes of the solutions were adjusted by addition of NaCl to concentrations of 6.25 x 10^{-4}, 6.25 x 10^{-3}, 6.25 x 10^{-2}, 1.25 x 10^{-1}, 2.5 x 10^{-1}, 5 x 10^{-1}, and 1 x 10^{0} M. Both chips displayed similar shifts in the SPR wavelength ($\Delta\lambda_{SPR}$) with respect to the change in solution refractive index.

Quantitative comparison of the SPR response of the conventional and iSPR chips revealed that the inherent sensitivity of the iSPR chip was not diminished by the presence of the electrode gaps. The sensitivities of the conventional (S_C) and iSPR (S_i) chips were found to be dependent on [NaCl], and nearly identical (Fig. 5.5b). When exposed to 6.25 x 10^{-4} M NaCl, corresponding to a refractive index change of 0.00125 RIU, the conventional and iSPR chips produced sensitivities of 6103 and 6104 nm•RIU^{-1}, respectively. S_C and S_i both increased as [NaCl] increased, with the ratio of S_C/S_i near unity for all [NaCl]. Therefore, the 5 μm electrode gaps for the IDE with 100 μm width electrodes did not reduce the inherent sensitivity of iSPR chips compared to conventional chips without discontinuities in the Au film, and could be used as effective SPR substrates.

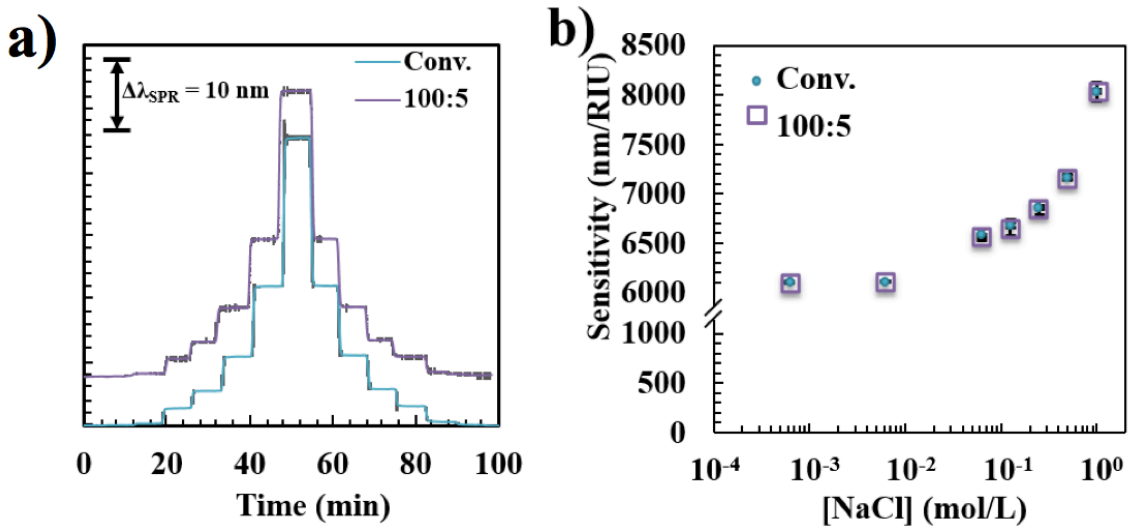

Figure 5.5. a) Sensorgrams from the conventional (bulk) and iSPR (E_G = 5 μm, E_W = 100 μm) chips in response to NaCl solutions of 6.25 x 10^{-4}, 6.25 x 10^{-3}, 6.25 x 10^{-2}, 1.25 x 10^{-1}, 2.5 x 10^{-1}, 5 x $10^{-1}$and 1 x 10^{0} M. Note the sensorgram for the iSPR chip was vertically shifted for clarity. b) Calculated sensitivity for the conventional (S_C) and iSPR (S_i) chips upon exposure to NaCl

solutions. The error bars in both panels represent the standard deviation from three separate sensing channels.

5.3.4 *Theoretical DEP Calculations for E. coli Cells in iSPR Electric Fields*

With equal performance in the inherent sensitivity of the conventional and iSPR chips, it was desired to investigate how the chips responded to surface changes in the refractive index (i.e. bacterial cell adsorption). However, it was critical to first predict how the DEP force (F_{DEP}) would affect cell movement in the microchannel. The time-averaged expression for the dielectrophoretic force exerted on a dielectric particle is given by Eq. 1.1. The direction of cell migration in a DEP-active, asymmetric electric field is determined by the CM factor.[129] The CM factor is dependent on the permittivity of the particle, conductivity of the suspending medium, and frequency of the applied AC potential. As previously reported, a two-shell model was developed to accurately describe the CM factor for Gram-negative bacteria such as *E. coli* by accounting for the different dielectric properties of the interstitial layers including the cytoplasm, cell membrane, and cell wall.[141] This model was used to calculate the CM factor for *E. coli*.

Figure 5.6a shows the calculated CM factor for *E. coli* in suspending media ranging in conductivities of 10^{-4} (pure DI H_2O) – 2 S/m as a function of the applied AC potential frequency. For media conductivities of 10^{-4} – 10^{-2} S/m only pDEP was predicted for *E. coli*. Conversely, for highly conductive media (1 and 2 S/m), only nDEP was predicted. A single crossover frequency (COF) was observed at 8.31 x 10^5 Hz for a medium conductivity of 10^{-1} S/m. The location of cellular adsorption on the IDEs will be determined by whether the cell experiences positive or negative DEP.

The location of cell adsorption can be predicted by interrogation of the DEP force potential, and determination of whether the cells will experience pDEP or nDEP. Analytical solutions to the DEP force potential, defined by the square of the electric field intensity (E_x^2 +

E_y^2), on IDEs were taken from a previous report.[77] The gradient of the DEP force potential can be directly used to calculate the force exerted by the DEP field on the bacterial cell. Figure 5.6b shows the DEP force potential for IDEs on iSPR chips (E_G = 5 μm, E_w = 100 μm). The electric field gradient is largest at sharp vertices between adjacent electrodes (i.e. electrode edges), and at a minimum in the center of the electrodes. Bacterial cells experiencing pDEP or nDEP therefore preferentially localize at the edges or centers of the IDEs, respectively.[163] While pDEP and nDEP promote cellular adsorption to different locations on the iSPR electrodes, both will induce changes in local dielectric environment, and thus an observable shift in $\Delta\lambda_{SPR}$.

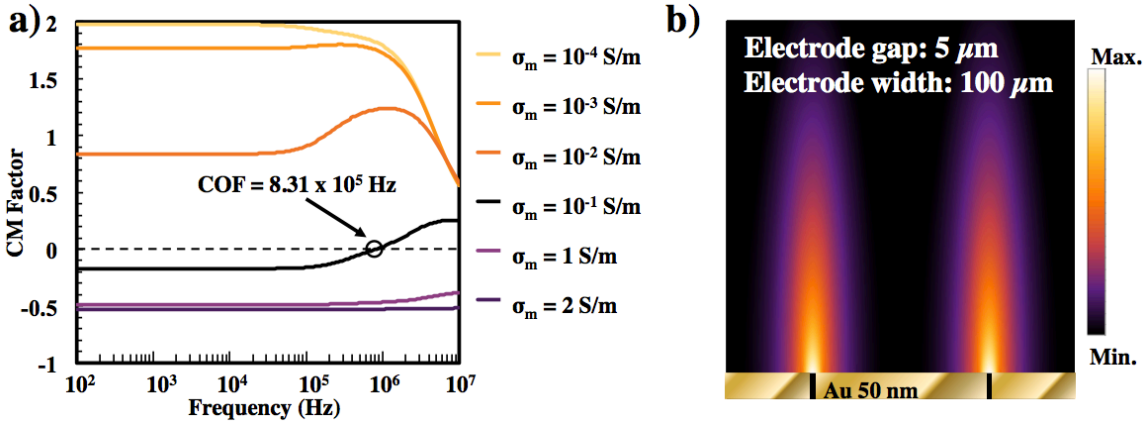

Figure 5.6. a) CM factor calculation for an *E. coli* cell suspended in media of varying conductivities. A single cross over frequency (COF) is observed at 8.31 x 10^5 Hz with a medium conductivity (σ_m) of 10^{-1} S/m. For σ_m = 10^{-4}, 10^{-3}, and 10^{-2} S/m, positive DEP (pDEP) is observed, whereas for σ_m = 1 and 2 S/m only negative DEP (nDEP) occurs. b) Cross-sectional view of the DEP force potential ($E_x^2 + E_y^2$) for IDEs on iSPR chips with E_G and E_W of 5 and 100 μm, respectively. Bacterial cells that experience pDEP localize at the potential maximum (i.e. edges of the electrodes), and cells under nDEP localize at the potential minimum (i.e. center of the electrodes).

5.3.5 *Effect of Applied DEP Field on Resonant Wavelength*

The SPR response under application of DEP revealed new features in the iSPR sensorgram not observed in the conventional sensorgram, manifesting as a negative shift in $\Delta\lambda_{SPR}$. To better understand the nature of the negative $\Delta\lambda_{SPR}$ shift, DI H_2O was introduced into the sensing channels over the iSPR chip at flowrates of 5, 10, 25 and 50 μL/min. Voltage

potentials of 5 and 10 V_{pp} at 500 Hz were then sequentially applied across the iSPR chip. An immediate negative shift in $\Delta\lambda_{SPR}$ was observed upon application of the 5 V_{pp} potential for all flowrates (Fig. 5.7a). The negative shift in $\Delta\lambda_{SPR}$ was independent of the volumetric flowrate, but larger negative shifts were observed at 10 V_{pp}. Importantly, the baseline was regained, returning to $\Delta\lambda_{SPR}$ = 0 nm, after removal of the DEP potential.

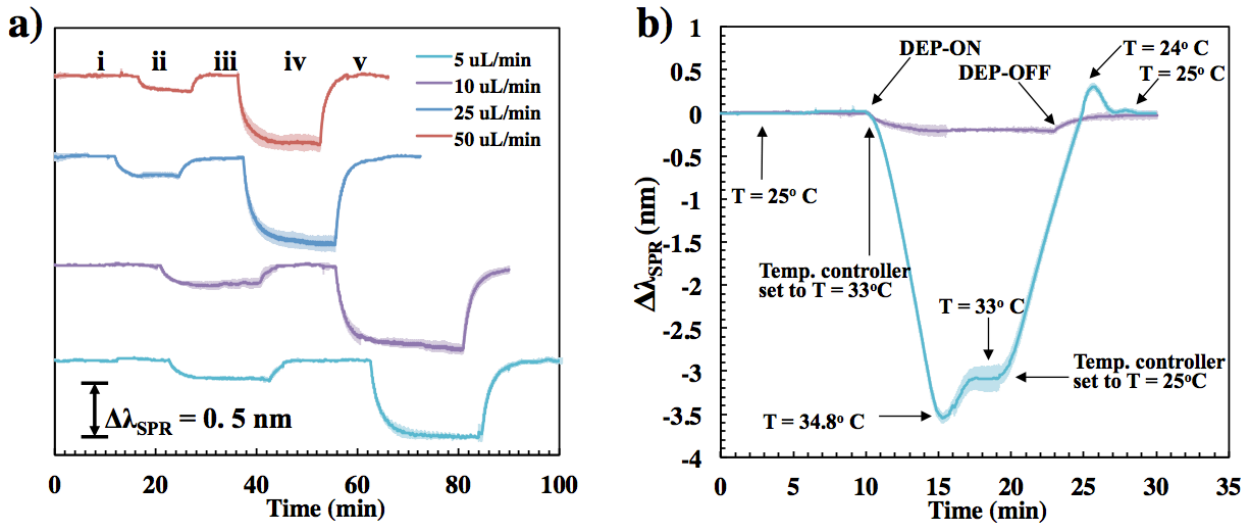

Figure 5.7. a) Effect of DEP on the SPR sensorgram as a function of voltage and volumetric flowrate. iSPR chips (E_G = 5 µm, E_W = 100 µm) were connected to the function generator, and an on-off cycle was applied with a fixed 500 Hz frequency. The flowrate of DI H_2O was varied from 5 – 50 µL/min. The following conditions apply to all four sensorgrams in a): i) function generator turned off, ii) function generator turned on with 5 V_{pp} potential, iii) function generator turned off, iv) function generator turned on with 5 V_{pp} potential, and v) function generator turned off. b) Effect of temperature on the SPR sensorgram. A temperature controller was used to modulate the inlet DI H_2O (10 µL/min) temperature from 25 – 33°C, and then reduced again to 25°C (blue trace). For comparison, the sensorgram from the iSPR chip under a 5 V_{pp} AC potential at 500 Hz and DI H_2O flowrate of 10 µL/min is also plotted (purple trace). The error bars represent the standard deviation from three sensing channels. In both panels, the error bars represent the standard deviation from three sensing channels.

It was speculated that the negative $\Delta\lambda_{SPR}$ shift was caused by increased temperature in the immediate vicinity of the IDEs. In the 20 – 35°C temperature range, the refractive index of DI H_2O decreases with increased temperature.[171] Therefore, λ_{SPR} must blueshift for the momentum of the incident light vector and free electron plasma to remain equal. To test this, a temperature controller was employed to modulate the inlet DI H_2O temperature in the absence of DEP. The

inlet flowrate was held fixed at 10 μL/min. After the baseline was established, the temperature controller was used to increase the inlet DI H_2O temperature from 25 to 33°C. It can be seen that the temperature controller overshot the set point to a maximum temperature of 34.8°C before reaching a steady-state temperature of 33°C. A negative shift of $\Delta\lambda_{SPR}$ = -3.066 ± 0.038 nm was observed when a steady-state temperature of 33°C was reached (Fig. 5.7b). After which, the inlet temperature was reduced back to 25°C, and the original baseline was regained. The negative $\Delta\lambda_{SPR}$ shift of –0.203 ± 0.035 nm caused by the application of a 5 V_{pp} potential at 500 Hz and flowrate of 10 μL/min is estimated to have increased the local temperature near the IDEs by ~0.53°C. The application of DEP under these conditions should therefore not induce thermal stress on the *E. coli* cells.

5.3.6 *DEP-Enhanced SPR Detection of E. coli*

The detection sensitivities towards *E. coli* suspensions for conventional and iSPR chips were directly compared. As shown in Fig. 5.6a, non-conductive media such as DI H_2O ($\sigma_m = 10^{-4}$ S/m) produce the highest, positive CM factor values, and thus pDEP force, in the low frequency regime. Therefore, the applied potential was held constant at 500 Hz and 5 V_{pp} for the duration of the DEP-SPR experiments to ensure a maximal pDEP force. The Au surfaces of conventional and iSPR chips were first mannoyslated, as the LOD for conventional chips was extraordinarily high (10^8 CFU/mL) using a simple octadecane thiol SAM (Fig. 5.8). *E. coli* containing type-1 fimbriae express the FimH adhesin that recognize and adhere to highly mannosylated surfaces.[169, 170] Highly mannosylated surfaces have been previously employed in SPR biosensing, and were shown to drastically increase cellular adherence to the SPR sensing surface.[172]

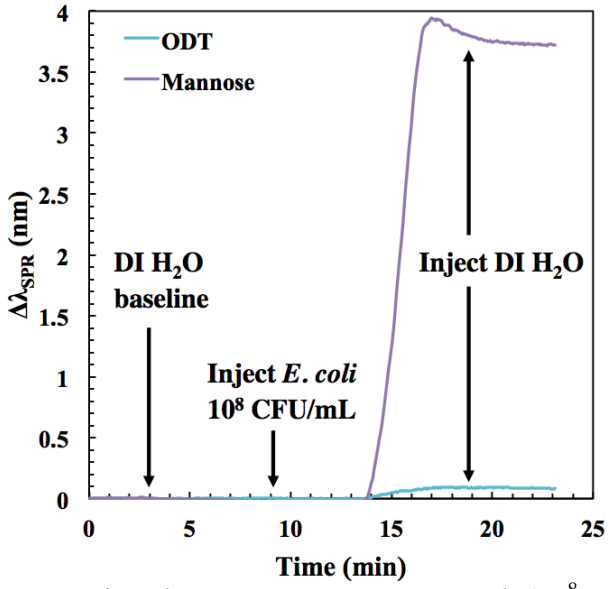

Figure 5.8. Sensorgram comparing the SPR response to *E. coli* (10^8 CFU/mL) on conventional SPR chips with different surface modifications. A 42.8x increase in $\Delta\lambda_{SPR}$ was observed for the mannosylated SPR chip compared to that functionalized with an octadecane thiol (ODT) self-assembled monolayer.

Figure 5.9a shows the results for *E. coli* detection with the conventional SPR chip. SPR wavelength shifts ($\Delta\lambda_{SPR}$) of 3.734 ± 0.009 and 0.429 ± 0.017 nm were observed for *E. coli* concentrations of 10^8 and 10^7 CFU/mL, respectively. Reduction in the bacterial concentration to 10^6 CFU/mL produced no observable shift in $\Delta\lambda_{SPR}$ (Fig. 5.9b).

For *E. coli* detection with the iSPR chip, DEP was applied simultaneously as the inlets were switched from DI H_2O to the bacterial suspensions. Immediately a negative $\Delta\lambda_{SPR}$ was observed. Approximately 5 min after DEP application, the bacterial suspensions reached the IDE surfaces, and were drawn to the surface through pDEP leading to positive shifts in $\Delta\lambda_{SPR}$ (Fig. 5.9c). The slope of the temporal response was concentration dependent, with the most concentrated suspension (10^8 CFU/mL) producing the steepest slope. Compared to the conventional chip, ~15 and ~3-fold increases in $\Delta\lambda_{SPR}$ for the iSPR chip were observed for the 10^7 and 10^8 CFU/mL bacterial suspensions, respectively.

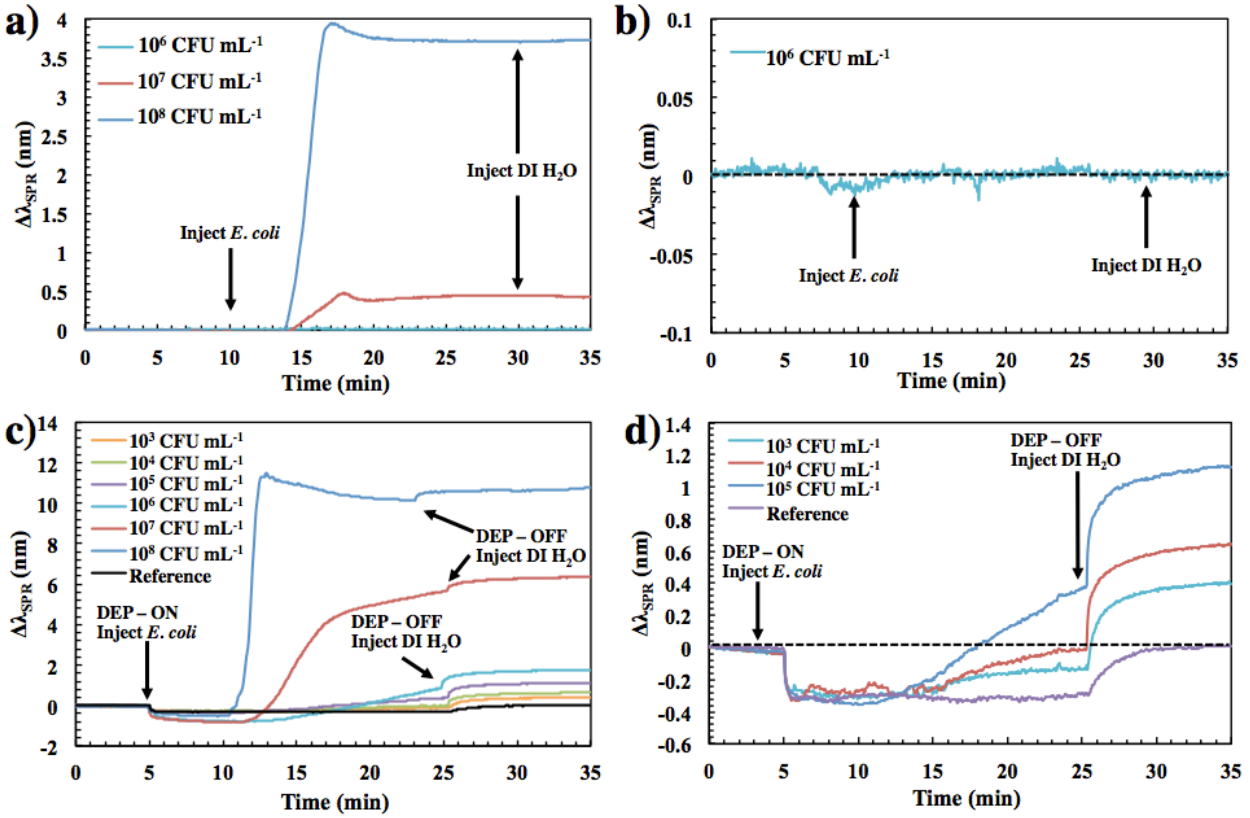

Figure 5.9. Sensorgrams for the real-time detection of *E. coli* on mannosylated a,b) conventional SPR and c,d) iSPR chips. DI H_2O was used to establish the baseline prior to injection of bacterial suspensions ranging in concentration from 10^3 – 10^8 CFU/mL. The flowrates for both DI H_2O and bacterial suspensions were held fixed at 10 µL/min. A 5 V_{pp} AC potential at 500 Hz was applied to the iSPR chip with a function generator immediately as the inlets were immersed in the bacterial suspensions. DEP was applied for 20 min, at which time the potential was removed and the inlets were reinserted in DI H_2O.

Furthermore, the iSPR chip was able to resolve shifts in $\Delta\lambda_{SPR}$ in dilute *E. coli* suspensions as low as 10^3 CFU/mL (Fig. 5.9d). Upon first application of DEP, the negative $\Delta\lambda_{SPR}$ was clearly visible, but increased rapidly when bacterial cells began flowing over the IDEs. A minimal $\Delta\lambda_{SPR}$ value of -0.322 nm was observed for the 10^3 CFU/mL suspension, before increasing to -0.138 nm during the 20 min application of DEP. Removal of the 5 V_{pp} potential resulted in a rapid increase in $\Delta\lambda_{SPR}$ as the local temperature near the IDEs was speculated to have decreased. The total compensated shift in $\Delta\lambda_{SPR}$ for the 10^3 CFU/mL was found to be 0.619 ± 0.016 nm.

The LOD in SPR biosensing is commonly defined as the $\Delta\lambda_{SPR}$ equal to 3x the standard deviation of the noise (σ_n) of the reference channel. The DI H_2O baseline was used to define σ_n = 0.141 nm. The DEP-SPR data were fit to a linear model, and the LOD for the iSPR chip was determined to be ~3.0 x 10^2 CFU/mL. Therefore, the increased cell flux to the IDEs induced by DEP led to a nearly five orders of magnitude improvement in the LOD of the iSPR chip compared to the conventional chip.

5.3.7 *Incorporation of Biorecognition Elements for the Selective Detection of E. coli*

Biorecognition elements were incorporated into the DEP-SPR sensing strategy to enable selective detection of *E. coli*. Biorecognition elements, such as antibodies and aptamers, integrated into SPR-based bacterial biosensors are typically configured to react with specific binding sites on the exterior of the bacteria to promote selective adhesion to the sensing surface. Both antibodies and aptamers can be selected to have broad or narrow band reactivity. The continuum of reactivity can enable highly selective detection of bacteria down to the strain level, or exhibit a varying degree of cross-reactivity against multiple strains/genera of bacteria. In this work, two strategies to improve selectivity of the DEP-SPR sensing strategy using biorecognition elements were explored: (1) secondary amplification with polyclonal antibody (PAb) suspensions, and (2) surface-bound aptamers.

Secondary Amplification with Polyclonal Antibodies (PAb):

Using anti-*E. coli* polyclonal antibodies (PAb) enabled selective detection in the DEP-SPR detection strategy. *Staphylococcus epidermidis* served as non-target bacteria to verify the method. A mannosylated, conventional chip was used to immobilize *S. epidermidis* suspensions prior to secondary amplification with PAb. Figure 5.10a shows the SPR response to *S. epidermidis* on the conventional chip. Similar to *E. coli*, the 10^7 and 10^8 CFU/mL *S. epidermidis*

suspensions caused shifts in $\Delta\lambda_{SPR}$ of 1.621 ± 0.029 and 3.502 ± 0.101 nm, respectively, while no response was observed for the 10^6 CFU/mL suspension (Fig. 5.10b).

Subsequent exposure to PAb revealed that only *E. coli* generated a secondary amplification. Therefore, DEP can be used to capture dilute (10^3 CFU/mL) bacterial suspensions, and secondary antibody amplification enables a selective control handle to discriminate between target and non-target bacteria. After immobilization of 10^7 and 10^8 CFU/mL *S. epidermidis* suspensions on a conventional chip and a 10^3 CFU/mL *E. coli* suspension on an iSPR chip, the adsorbed bacteria were exposed to PAb. A PBS/BSA buffer solution was flowed through the channels to block non-specific adsorption sites on the chips prior to flowing 50 μg/mL PAb in the PBS/BSA buffer solution. The 10^7 and 10^8 CFU/mL *S. epidermidis* suspensions produced maximal $\Delta\lambda_{SPR}$ shifts of 0.191 ± 0.004 and 0.126 ± 0.003 nm, respectively, when exposed to PAb. However, theses responses dropped to 0.028 ± 0.003 and 0.053 ± 0.004 nm, respectively, once the inlets were switched back to the PBS/BSA buffer solution (Fig. 5.10c). The negligible increase in $\Delta\lambda_{SPR}$ for the secondary amplification of *S. epidermidis* indicates the lack of interaction of *S. epidermidis* with PAb. Conversely, *E. coli* exhibited non-reversible binding to PAb, and a stable increase in $\Delta\lambda_{SPR}$ upon secondary amplification. Unlike the non-target *S. epidermidis*, *E. coli* displayed a large $\Delta\lambda_{SPR}$ of 0.741 ± 0.054 nm, which was not diminished when the inlets were switched back to the PBS/BSA buffer solution. The secondary amplification demonstrates that dilute (10^3 CFU/mL) suspensions of target bacteria can be selectively detected in the presence of non-target bacteria with iSPR chips. The complete sensorgrams for the 10^7 and 10^8 CFU/mL *S. epidermidis* suspensions on a mannosylated conventional SPR chip and for the 10^3 CFU/mL *E. coli* suspension on a mannosylated iSPR chip are shown in Fig. 5.10d. The secondary amplification demonstrates that

dilute (10^3 CFU/mL) suspensions of target bacteria can be selectively detected in the presence of non-target bacteria with iSPR chips

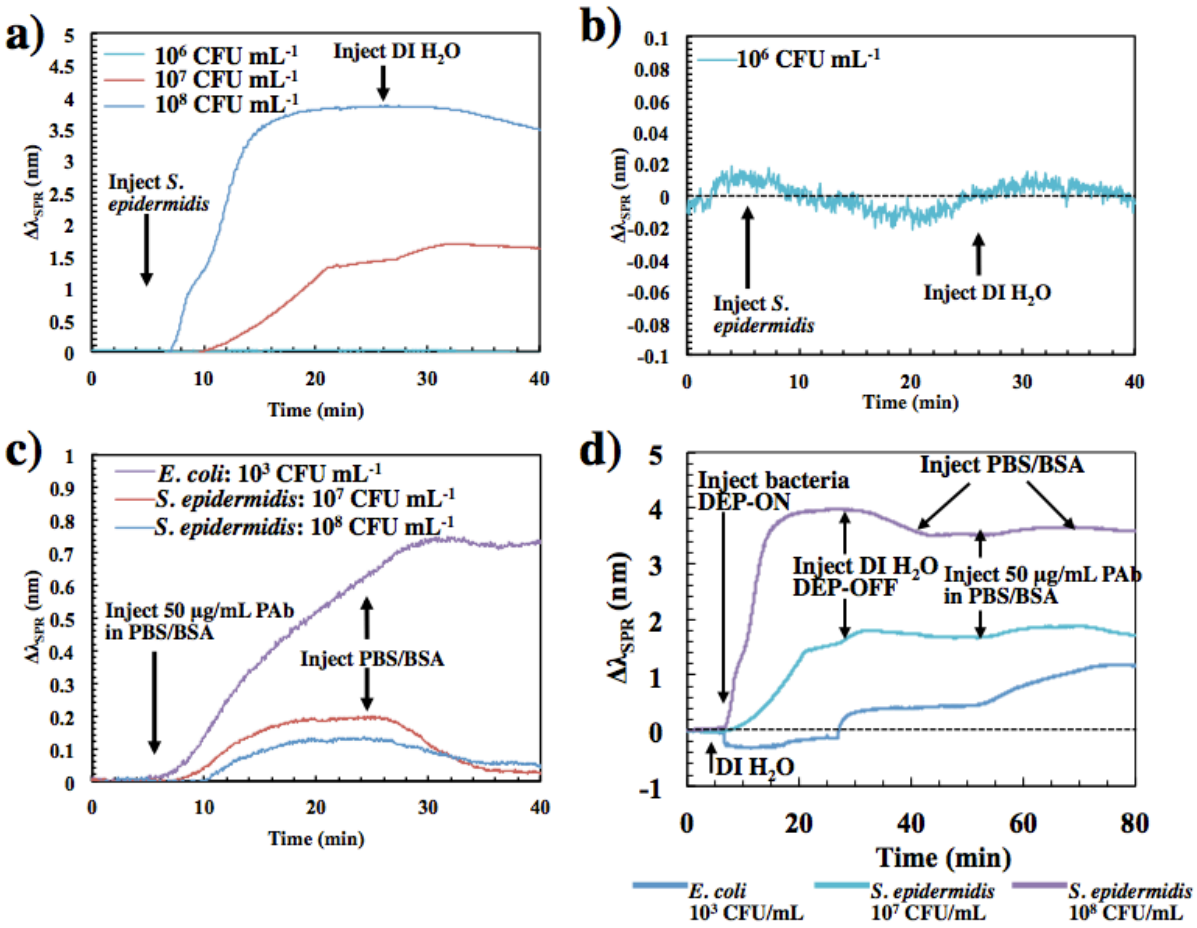

Figure 5.10. Selective detection of *E. coli* with secondary PAb amplification. a) Sensorgrams showing the response to *S. epidermidis* suspensions ranging in concentrations from 10^6 – 10^8 CFU/mL on a conventional SPR chip. b) Expanded view of the 10^6 CFU/mL *S. epidermidis* suspension, showing no response. c) Secondary PAb amplification of the 10^7 and 10^8 CFU/mL *S. epidermidis* in a), and the 10^3 CFU/mL *E. coli* suspension captured with DEP in Fig. 5.9d. d) Complete sensorgrams for detection and secondary antibody amplification of *S. epidermidis* on mannosylated, conventional chips, and *E. coli* on a mannosylated, iSPR chip. Following detect of bacteria suspended in DI H_2O, the inlets were switched to a PBS/BSA buffer solution. After baseline establishment, the adsorbed bacteria were exposed to PAb, and the inlets were finally switched back to the PBS/BSA buffer.

Surface-Bound Aptamers Against E. coli:

Aptamers are olgionucelotide sequences that kind bind to a host of targets including ions, peptides, small molecules, and large microorganisms (i.e. bacterial cells).[173] Aptamers can be selected against their target in vitro through Systematic Evolution of Ligands by EXponential

enrichment (SELEX). Previous work using SELEX was able to identify an aptamer possessing a high level of selectively towards *E. coli* (ATCC 25922).[174] The aptamer, referred to as "P12-31", consisted of 85 DNA bases: 5'-CATACGATTTAGGTGACACTATAGCCCTCCGGGGGGGTCATCGGGATACCTGGTAAG GATAATTTCTCCTACTGGGATAGGTGGA-3'. The 5' end was modified with an amine group to enable linkage to the surface with EDC/NHS coupling.

The selectivity of P12-31 was investigated using conventional SPR chips. The chips were cleaned, and modified with mixed 11-mercaptoundecanol (11-MU) and 11-mercaptoundecanoic acid (11-MUA). Mixtures of 1:1, 1:5, 1:20, and 1:100 of 11-MUA:11-MU were immobilized on the Au surfaces of conventional chips. The hydrophilic 11-MU served as the non-fouling background, while the carboxylic acid group of 11-MUA was used to link P12-31 to the surface with EDC/NHS coupling. Figure 5.11 shows the reflectivity spectra of the different ratios of mixed SAMs, which indicate that the inherent SPR responses were not altered.

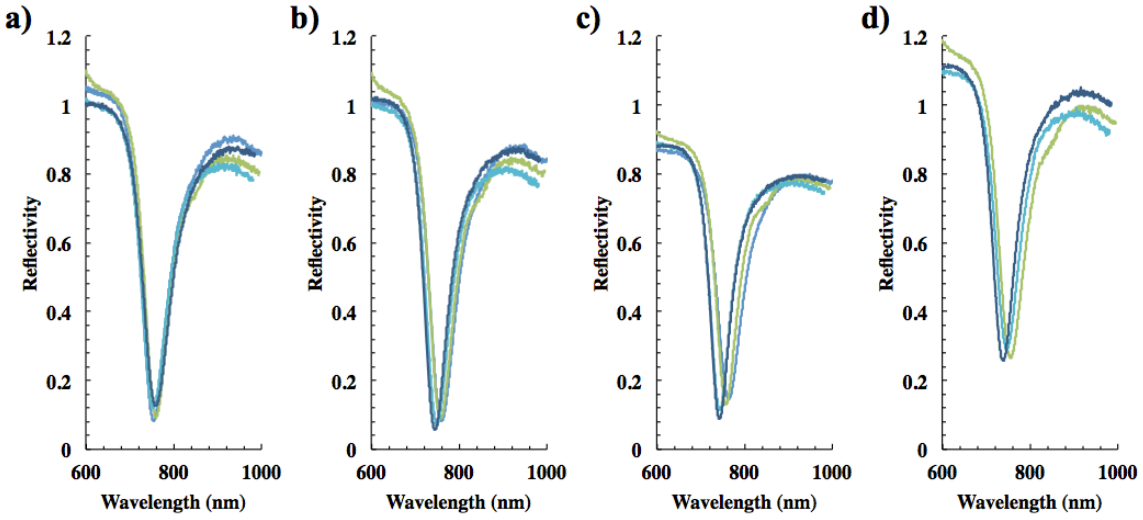

Figure 5.11. Reflectivity spectra for mixed 11-MU and 11-MUA SAMs at ratios of 11-MUA:11-MU a) 1:1, b) 1:5, c) 1:20, and d) 1:100.

Pure *E. coli* (10^8 CFU/mL), pure *S. epidermidis* (10^8 CFU/mL), and mixed *E. coli* and *S. epidermidis* (5 x 10^7 CFU/mL each, total bacterial concentration = 10^8 CFU/mL) suspensions

were injected into the SPR instrument after baseline establishment with DI H_2O. The flowrate was held fixed at 10 µL/min for all experiments. The results of the SPR experiments are summarized in Fig. 5.12. For all chips no response for *E. coli* was observed, and small responses of ~0.075 and 0.15 nm were observed for *S. epidermidis* on the 1:5 and 1:20 surfaces, respectively.

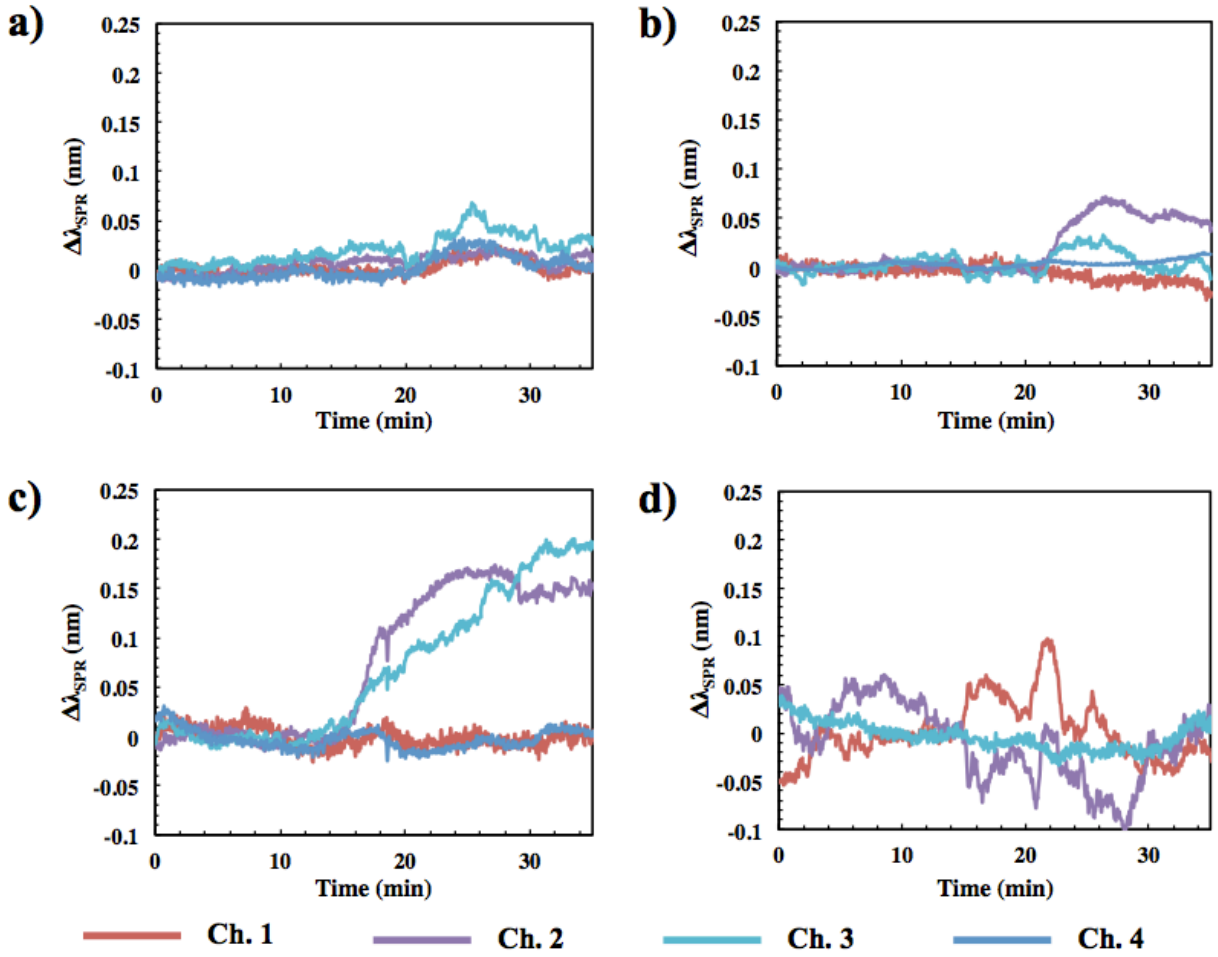

Figure 5.12. SPR sensorgrams of *E. coli* detection (10^8 CFU/mL) on conventional chips functionalized with mixed 11-MU and 11-MUA SAMs at ratios of 11-MUA:11-MU a) 1:1, b) 1:5, c) 1:20, and d) 1:100, with further aptamer conjugation. In each of the four panels the SPR channels contained: Ch.1 – *E. coli* (10^8 CFU/mL), Ch.2 – *S. epidermidis* (10^8 CFU/mL), Ch.3 – mixed *E. coli* and *S. epidermidis* (5 x 10^7 CFU/mL each), and Ch.4 – DI H_2O.

The inverted selectivity of P12-31 observed in the SPR experiments is attributed to its secondary structure. The SELEX process used to isolate P12-31 is solution-based, and allows

the aptamer freedom of rotation around the exterior of the bacteria. Immobilization of P12-31 on the SPR surface at the 5' end effectively fixed the orientation of the aptamer. It is speculated that the fixed orientation inhibited reactivity of *E. coli* with the secondary structure of P12-31.

5.4 CONCLUSIONS

In this work, the integration of dually functional IDEs capable of sustaining SPR and generating DEP into a single iSPR chip was investigated. SP generation was found to be dependent on the presence of discontinuities in the Au films used to define the width of the IDEs. IDEs with widths greater that the SP propagation length were found to sustain sharp reflectivity dips comparable to the conventional SPR device. The inherent sensitivity to changes in the bulk refractive index of the iSPR chip was found to be nearly identical to the conventional chip, indicating that the 5 μm electrode gaps did not introduce detrimental sensitivity side effects.

The iSPR chip was used to improve the LOD of *E. coli* by nearly five orders of magnitude with the application of DEP compared to the conventional SPR chip without DEP. The LOD for the iSPR chip was found to be ~3.0 x 10^2 CFU/mL, compared to ~1 x 10^7 CFU/mL for the conventional SPR chip. The improved LOD in the iSPR chip was attributed to increased mass transport of bacterial cells to the IDE surface. Unlike the conventional SPR chips that rely solely on diffusion of cells to the sensing surface, the iSPR chips increased cellular accumulation on the IDE surface due to the additional DEP driving force. Furthermore, selective detection of *E. coli* over non-target *S. epidermidis* was enabled through secondary antibody amplification. While the secondary antibody amplification generated additional SPR shifts for dilute (10^3 CFU/mL) *E. coli*, the *S. epidermidis* signals of concentrated suspensions (10^7 and 10^8 CFU/mL) were unamplified. The strategy developed here demonstrates that the integration of DEP and SPR into a bacterial detection module can enable sensitive detection of dilute, bacterial

suspensions, and when combined with downstream antibody amplification, can discriminate target from non-target bacteria.

Chapter 6. BACTERIAL DETECTION AND SEPARATION ENHABLED BY THE COMBINATION OF SERS AND DEP ON INTERDIGITATED ELECTRODES

6.1 INTRODUCTION

While the previous studies reported here and throughout most of the literature focus on classification and identification of pure bacterial isolates, samples in the clinical and environmental sectors exist as inhomogeneous suspensions of bacterial diversity.[2] Additional complexities arise due to the media in which the bacterial samples are suspended, which can contain organic matter from soil or plants, blood cells, or proteins and enzymes.[175] Larger contaminants such as organic matter and blood cells can easily be removed from the sample by membrane filtration. However, depending on the particular sample, the elutant can contain bacterial inhomogeneity at both the species and strain levels.[176] The combined use of DEP and SERS can be used post-filtration to simultaneously separate bacterial species based on inherent differences in dielectric properties by DEP,[42] and differentiate bacterial cells from the biochemical differences in the SERS spectra.[177]

DEP has been successfully shown to separate mixtures containing different classes of cells.[42] However, examples of separation by DEP followed by SERS identification of bacteria have been limited to septic samples in both microfluidic[68, 69] and static conditions.[70, 71] In the static configuration, an applied frequency of 10 MHz induced pDEP and nDEP in bacterial and red blood cells (RBCs), respectively. Bacterial cells were concentrated on the SERS-active surface while RBCs were simultaneously repelled. A limit of detection of 10^5 CFU/mL of

bacterial cells in 10^8 cells/mL of RBCs was obtained. Impressively, identification was achieved in less than 5 minutes.

Due to variation in the dielectric properties of bacterial cells, DEP has been used to separate heterogeneous bacterial mixtures.[178] While the concurrent use of DEP and SERS is unreported, other techniques such as impedance and optical spectroscopies have unveiled DEP as a viable technique for this application. Combined used of DEP with optical spectroscopy was used to distinguish live versus dead populations of *Escherichia Coli* and *Klebsiella pneumonia*,[179, 180] *Mycobacterium smegmatis*,[181] and clinical Gram-negative isolates.[182] The technique reduced the required time for a successful antibiotic susceptibility test (AST), and determination of the minimum inhibitory concentration (MIC). The working principal of the technique capitalized on the elongation of bacterial cells after antibiotic treatment. Prior to treatment cells were concentrated in the gaps between DEP electrodes, and the antibiotics induced a change in the DEP response of the bacterial cells causing them to relocate on the DEP chip. Cellular migration was detected through optical microscopy and used to determine the MICs.

While DEP has been studied for ~50 years,[183] new application-driven devices are still being created. The work described in Chapter 4 and summarized here indicate two important aspects of DEP-enhanced bacterial biosensing: (1) DEP electrodes can provide both sensitive SERS surfaces and DEP manipulation of bacterial cells, and (2) bacterial cells down to the strain-level can interact with the DEP field differently.[161] Therefore, DEP separation and subsequent identification with SERS could offer a potentially new route to identify subpopulations in bacterial mixtures.

In this chapter, we describe the development of a DEP-SERS device for the separation of Gram-negative and Gram-positive bacterial cells. The device consists of hierarchical electrode configuration. Micron-scale interdigitated electrodes (IDEs) effectively generate non-uniform electric fields for cellular manipulation, and metal film over nanospheres (MFONs) deposited on IDEs provide nanostructured, SERS-active surfaces. Finite-difference time-domain (FDTD) simulations were used to design the MFON surfaces to provide effective enhancement and accessibility of the SERS 'hot-spot' to the bacterial cells. Fabricated devices were characterized with surface-bound small molecules, and found to have uniform enhancement. The DEP-SERS device here could be used in the clinical setting to rapidly separate bacterial cells for further processing such as antibiotic susceptibility and minimum inhibitory testing.

6.2 EXPERIMENTAL

6.2.1 *FDTD Simulations of Metal Film Over Nanosphere (MFON) Structures*

FDTD simulations were conducted to study the electric field distributions and scattering profiles of MFON structures. Multilayered plasmonic structures were embedded in an aqueous background (n = 1.33) and from the bottom up consisted of four discrete layers: glass substrate (n =1.52), 100 nm Au film, polystyrene (PS) nanospheres (n = 1.59), and a capping 20 nm Au film (Fig. 6.1a). The refractive indices of glass and PS were taken as 1.51 and 1.45, respectively, while wavelength-dependent Au values were taken from the literature[85] and fit to a multi coefficient model. The FDTD unit cell was comprised of five, hexagonally-packed PS nanospheres (Fig. 6.1b). In the vertical direction, the unit cell extended 500 nm above the capping Au film and 200 nm below the glass/Au interface in the vertical direction. The lateral dimensions were defined by the nanosphere diameter (d_{ns}) as $2d_{ns}$ and $d_{ns}\sqrt{3}$ in the x and y

directions, respectively. A plane wave light source with the electric field component polarized in the x-direction was placed 400 nm above the Au capping film and injected normal to the surface. A reflectance monitor placed 450 nm above the Au capping layer collected backscattered light. Electric field distributions were collected at the simulation boundaries and at the bottom of the Au capping layer, where the nanosphere gap is the smallest.

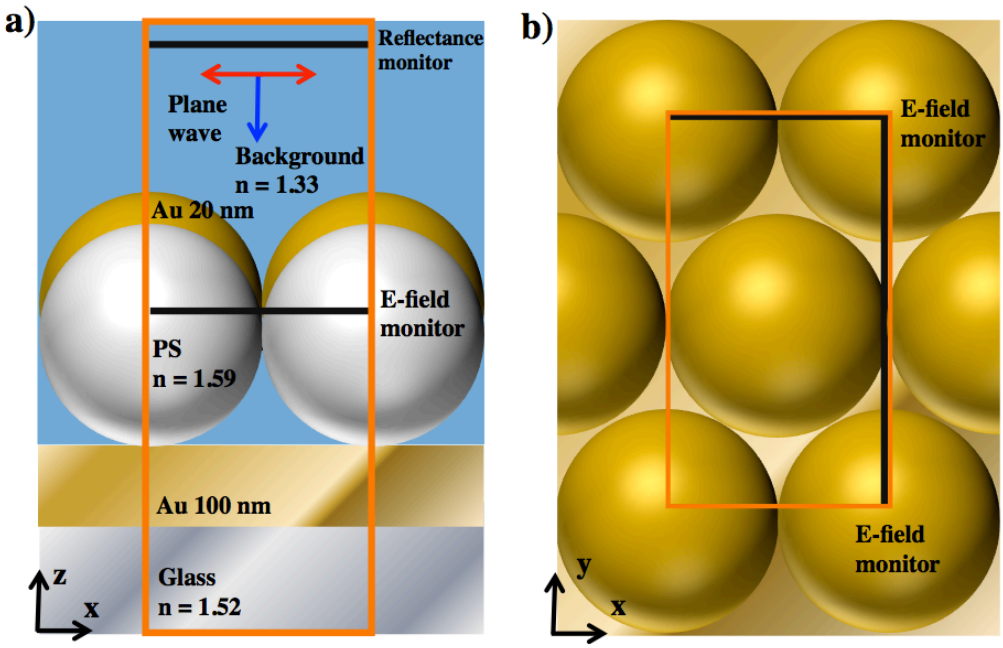

Figure 6.1. Schematic illustration of the MFON structures simulated with the FDTD method. a) Cross-sectional view of the xz plane and b) top-down view of the xy plane of the simulation region. The simulation unit cell was defined by the orange boundaries.

6.2.2 *Fabrication of Planar IDEs*

Glass slides (75 mm x 25 mm) were sonicated sequentially in soapy DI H_2O, acetone, and isopropyl alcohol for 20 min each. The glass substrates were then placed in an UV-O_3 cleaner for an additional 20 min. Glass substrates were desiccated with 3-mercaptopropyl(trimethoxy) silane (50 µL) to increase the adhesion of gold to the glass substrates. Deposition masks (PET tape) were patterned with IDEs with approximate electrode widths and gaps of 400 µm each with a CO_2 laser. The clean glass substrates with the aligned

deposition masks were then coated with a 100 nm Au film. Immediately following deposition PS nanospheres (d = 200 nm) were drop coated on the IDE substrates by placing 500 μL of a 1:1 solution of stock solution (Phosphorex, sulfate-capped, 1% solids by wt.) and DI H_2O directly on the substrates. The solution was dried in an oven at 50^oC for 1 hr. The dried IDE substrates were then coated with an additional 20 nm of Au, and the mask was removed to realize the finalized IDE device.

6.2.3 *SERS Measurements*

The freshly fabricated IDEs were surface modified with self-assembled monolayers (SAMs) of 4-mercaptophenyl boronic acid (4-MPBA) to characterize the SERS enhancement of the devices. 4-MPBA solutions (1 mM) were prepared by dissolving 4-MPBA powder into a 10%(v:v) mixture of ethanol and DI H_2O. IDEs were immersed in the 4-MPBA solution for 16 hr prior to SERS characterization. SERS measurements were collected on the Renishaw inVia Raman microscope equipped with a 785 nm excitation source (0.7 mW) and 50x objective. The Raman scattered photons were collected in the spectral window of 300 – 1800 cm^{-1} with a single 10s acquisition.

6.3 RESULTS AND DISCUSSIONS

6.3.1 *DEP of Gram-Positive and Gram-Negative Bacteria*

To explore the separation capabilities of the IDEs, *Escherichia Coli* (*E. coli*) and *Staphylococcus epidermidis* (*S. epidermidis)* were used as model cells. Combined these strains are responsible for ~50 - 77% of urinary tract infections (UTIs) annually in the United States.[184] However, because of the differences in their biochemical compositions, antibiotic treatments differ

substantially. Gram-negative bacteria such as *E. coli* and Gram-positive bacteria such as *S. epidermidis* have a lipopolysaccharide and peptidoglycan exteriors, respectively (Fig. 1.2).[38, 144]

It is hypothesized that the inherent differences of the cellular makeup of *E. coli* and *S. epidermidis* will lead to different responses to the non-uniform electric fields generated by the DEP-active IDEs that can be used for separations. Bacterial cells will experience positive DEP (pDEP) or negative DEP (nDEP) induced by the IDEs depending on the specific cellular dielectric properties. The Clausius-Mossotti (CM) factor dictates particle movement (i.e. pDEP vs. nDEP), and is dependent on inherent dielectric properties of the particle, and the conductivity of the background. The CM factor for *E. coli*, calculated using a two-shell model, is given by Eqs. 4.1- 4.8. Similarly, the CM factor for *S. epidermidis* was calculated using a single shell model for Gram-positive bacteria. The model accounted for the permittivity and conductivity of each interstitial cellular layer, including the cytoplasm and cell membrane, as well as the cell shape and surrounding media conductivity. *Staphylococcus epidermidis* was modeled as a 1 µm spherical particle, consisting of a cytoplasm encapsulated by a 20 nm membrane. The CM factor for an *S. epidermidis* particle was calculated with the following equation:[185]

$$\varepsilon_p^* = \varepsilon_{mem}^* \frac{(\frac{a_0}{a_1})^3 + 2\,(\frac{\varepsilon_{cyto}^* - \varepsilon_{mem}^*}{\varepsilon_{cyto}^* + 2\varepsilon_{mem}^*})}{(\frac{a_0}{a_1})^3 - 2\,(\frac{\varepsilon_{cyto}^* - \varepsilon_{mem}^*}{\varepsilon_{cyto}^* + 2\varepsilon_{mem}^*})} \qquad \text{Eq. 5.1}$$

where ε_p^* is the complex particle permittivity as in Eqs. 1.3 and 1.4, a_0 and a_1 are the radii of the cytoplasm and cell membrane, respectively. Here, the particle permittivity is comprised of contributions from the cell membrane (ε_{mem}^*) and cytoplasm (ε_{cyto}^*), as opposed to the homogeneous particle described in Eq. 1.2. The CM factor as a function of frequency in media conductivities in the range of 10^{-4} – 2 S/m for *S. epidermidis* is shown in Fig. 6.2.

The conductivity of the background medium can play a significant role in the DEP force induced on the bacterial cell. No crossover frequencies (COFs) are observed for *S. epidermidis* cells in low conductivity media (10^{-4} – 10^{-3} S/m), indicating that the cell experiences only pDEP. However, when the media conductivity is increased to 10^{-2}, 10^{-1}, and 1 S/m COFs are observed at 6.76 x 10^{3}, 6.31 x 10^{4}, and 5.17 x 10^{5} Hz, respectively. The CM factor for the most conductive media (2 S/m) remained negative, indicating the *S. epidermidis* cell only experiences nDEP. Therefore, the CM factor calculations predict that tuning the medium conductivity can alter the direction of the DEP force on S. epidermidis cells.

Comparison of Figs. 4.4a and 6.2 suggest separation of *E. coli* and *S. epidermidis* bacterial mixtures is possible. For a medium conductivity of 10^{-2} S/m *E. coli* cells experience a pDEP force in the entire frequency range of 500 Hz to 10 MHz. However, for the same medium conductivity *S. epidermidis* cells remain in the nDEP regime for frequencies below ~6.8 kHz. Interestingly, the DEP behavior of the two bacterial cell types is inversed as the medium conductivity increases to 10^{-1} S/m. At this conductivity both *E. coli* and *S. epidermidis* cells experience nDEP at low frequencies, with COFs of ~831 kHz and ~63 kHz, respectively. Within the frequency range of 63 to 831 kHz, *S. epidermidis* bacterial cells move into the pDEP regime, while *E. coli* cells remain in the nDEP regime. Thus, it is predicted that proper tuning of the applied frequency and medium conductivity can separate *E. coli* and *S. epidermidis* bacterial mixtures.

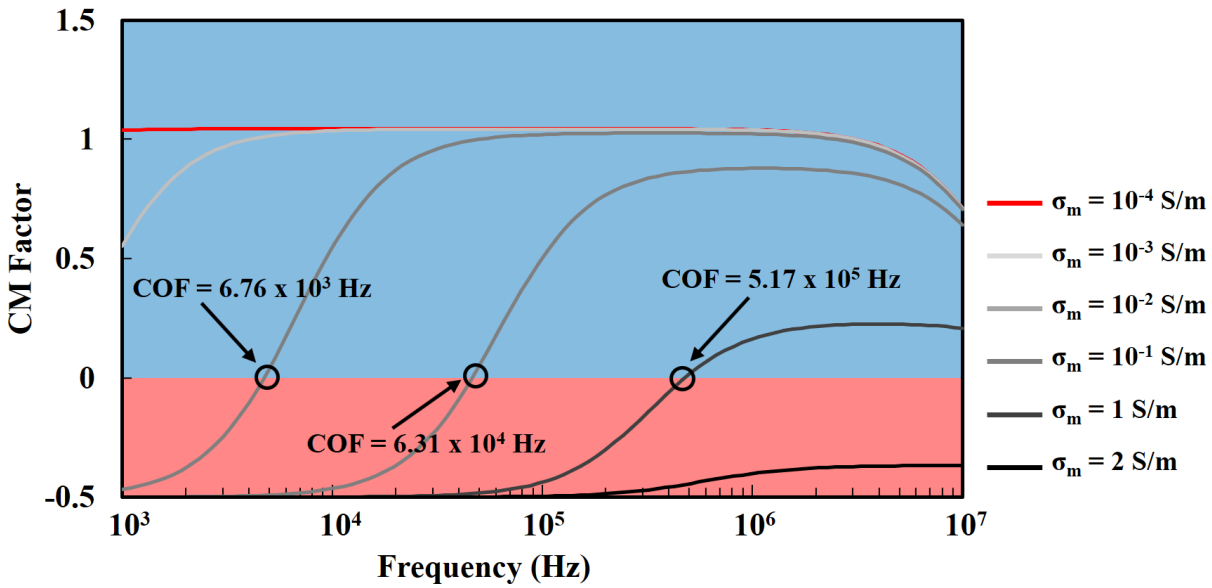

Figure 6.2. Clausius-Mossotti factor for an *S. epidermidis* bacterial cell suspended in a background medium with conductivity ranging from 10^{-4} – 2 S/m. The blue and pink regions indicate frequencies at which pDEP and nDEP occur, respectively.

6.3.2 *Design of IDE Devices*

DEP-active electrodes were configured in the interdigitated configuration.[77] Individual DEP-SERS devices consisted of 22 individual electrodes with widths and gaps of 400 µm each. Analytical solutions to the electric field distributions and gradients have been solved as a function of electrode width and spacing, and revealed that the effective distance at which the DEP force extends in the vertical direction is approximately the electrode width.[77] Bacterial cells in the DEP-SERS devices will experience the DEP force approximately 400 µm above the IDEs, and will concentrate at the electrode edges and electrode centers when in the pDEP and nDEP regimes, respectively.[140] However, cells in the nDEP regime above the ~400 µm DEP-active zone will experience a levitation force, and be excluded from the IDEs.[77] Bacterial cells in the nDEP regime will only migrate to the electrode centers if they are first brought within ~400 µm before the application of DEP. Therefore, the entirety of each individual electrode

surface need to provide uniform SERS enhancement sites that can be used to amplify the Raman signals of bacterial cells in both the pDEP and nDEP regimes.

MFONs were patterned over the IDEs to produce enhancing SERS surfaces over each electrode. MFONs are comprised of a self-assembled monolayer of polystyrene nanospheres coated with a thin Au film.[186] Large-area, highly-uniform patterns enabled by MFON structure formation, as no nanolithography techniques are required in the fabrication process. The plasmonic response of MFONs is primarily dictated by the size of the nanospheres, which controls the pitch of the hexagonally-packed arrays, and thus the LSPR absorption wavelength.[101] As discussed in Chapters 1 and 2, an optimal SERS substrate has an LSPR absorption in the 795 – 854 nm spectral window for a 785 nm NIR excitation source, and efficient confinement of electromagnetic energy to maximize the SERS enhancement.

FDTD simulations were used to optimize the plasmonic response of the MFON structures. The polystyrene nanosphere diameter and Au film thickness were varied from 200 – 542 and 20 – 50 nm, respectively. The effect of the underlying 100 nm Au film on the plasmonic response was also studied. Structures were characterized by the LSPR absorption wavelengths, and the location and intensity of the electromagnetic field confinement.

Electric field monitors were placed in the xy plane Au shell/PS sphere/H_2O interface (Fig. 6.1a). This interface includes all regions were neighboring Au shells are the closest and confinement of electromagnetic radiation should result in the largest SERS enhancement. Structures with d = 542 nm and Au thickness of 20 nm exhibited a maximum enhancement of $|E_{max}/E_0|^2 = 8.79 \times 10^4$ at $\lambda_{LSPR} = 1020$ nm, and removal of the 'resonant mirror' reduced the enhancement at $\lambda_{LSPR} = 1020$ nm to $|E_{max}/E_0|^2 = 7.42 \times 10^4$ (Fig. 6.3a). As the Au thickness was increased to 50 nm, the maximum enhancements of the structures with and without the resonant

mirror were reduced to $|E_{max}/E_0|^2$ = 9.87 x 10^3 and 8.94 x 10^3, respectively. However, the enhancement blueshifted to λ_{LSPR} = 884 nm, which lies nearer to the optimal range of 794 – 849 nm for SERS enhancement described by Eq. 2.2. For structures with d = 271 nm, the maximum enhancement of $|E_{max}/E_0|^2$ = 2.23 x 10^4 occurred at λ_{LSPR} = 892 nm with the resonant mirror and Au film thickness of 20 nm (Fig. 6.3b). Similarly, a maximum enhancement of $|E_{max}/E_0|^2$ = 2.50 x 10^3 was obtained for d = 200 nm with the resonant mirror and Au film thickness of 20 nm at λ_{LSPR} = 880.

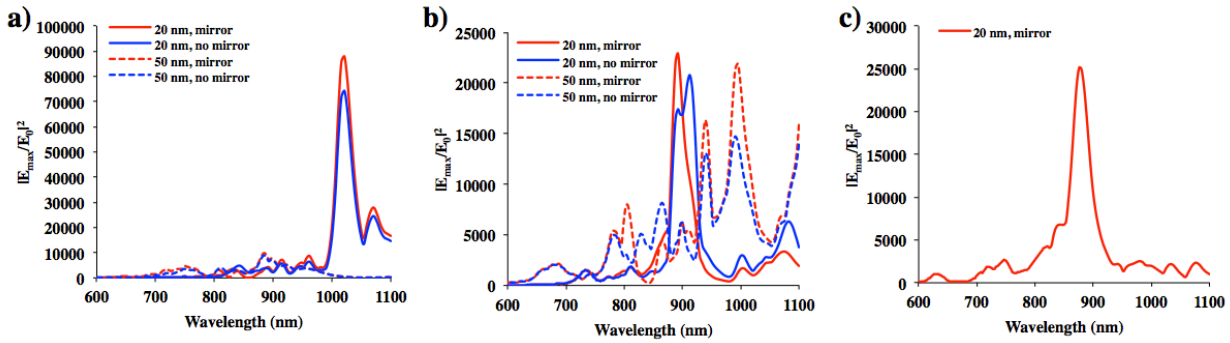

Figure 6.3. Electric field intensities at the Au shell/PS nanosphere/H_2O interface for nanosphere diameters of a) 542, b) 271, and c) 200 nm.

Therefore, d = 200 nm was found to be the optimal diameter for fabrication of the IDE SERS devices. While the maximal enhancement for d = 200 nm was less than d = 542 nm by a factor of ~3.5, at λ_{LSPR} for d = 542 nm was redshifted out of the optimal SERS range by 171 nm. However, λ_{LSPR} for d = 200 nm is only 31 nm redshifted from the optimal SERS range, making the maximal enhancement accessible for SERS measurements. Further reducing the nanosphere size could lead to further blueshift of λ_{LSPR} into the optimal range, but synthesis of monodisperse PS nanospheres is difficult for diameters less than 200 nm. Additionally, a reduction in the diameter from 542 to 200 nm increases accessibility of the SERS 'hot spots' to the bacterial cells. As the radii of *E. coli* and *S. epidermidis* are ~500 nm, the depth of the wells created by the nanospheres should be reduced to allow intimate contact of the cell wall with the SERS hot spot.

The hot spots follow the Au/PS contour around the nanospheres (Fig. 6.4a), and occur at the lowest edge of the Au shell (Fig. 6.4b). The optimal MFON structures contain the resonant mirror. While the resonant mirror provides an increased enhancement, it additionally provides an electrical path for the DEP current to flow.

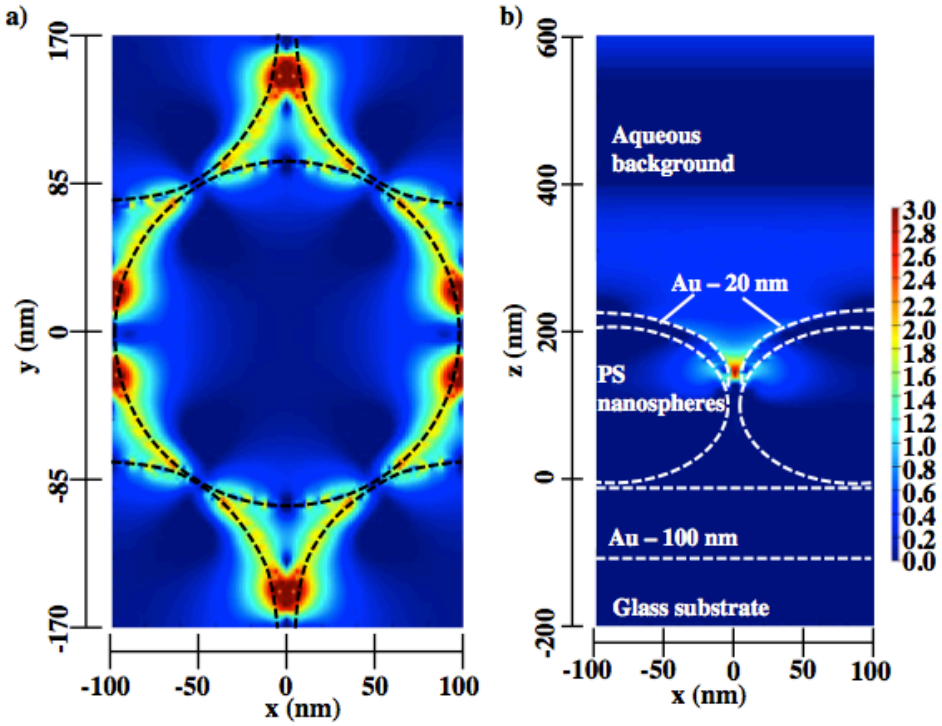

Figure 6.4. Electric field distribution of MFON structures (d = 200 nm) in the a) xy plane, and b) xz plane. The scale bar represents $|E_0/E_{max}|^2$ on a log scale.

6.3.3 *SERS Characterization of MFON-Coated IDE Structures*

SERS measurements of 4-MPBA immobilized on MFON structures were collected to quantify the intensity of the SERS signals on individual electrodes. A non-uniform PS nanosphere was observed on individual electrodes, which displayed a concentrated band of nanospheres in center of the electrodes (Fig. 6.5a). SERS spectra were collected across individual IDEs with ~50 μm lateral spacing to quantify the variance in the SERS signal within each IDE. The intensity of the 1075 cm^{-1} band served as the standard vibrational mode to compare the SERS signals from different locations on the device. The strongest SERS

intensities were obtained from the central band where PS nanoparticles were the most concentrated, with an intensity of 2.03 x 10^4 counts at the 1075 cm^{-1} band. The outermost regions of the individual IDEs produced the lowest intensities, which averaged 2.03 x 10^3 counts. A large variance in the 1075 cm^{-1} band was observed. For a sample size of 15 spectra collected over the DEP-SERS device, and average intensity and standard deviation of 8.01 x 10^3 and 5.01 x 10^3 counts, respectively, were obtained. The large variance must be corrected if quantitative signals relating to bacterial concentration are to be collected. However, after standardization the spectra display an average and narrower standard deviation of 7.97 and 0.59, respectively.

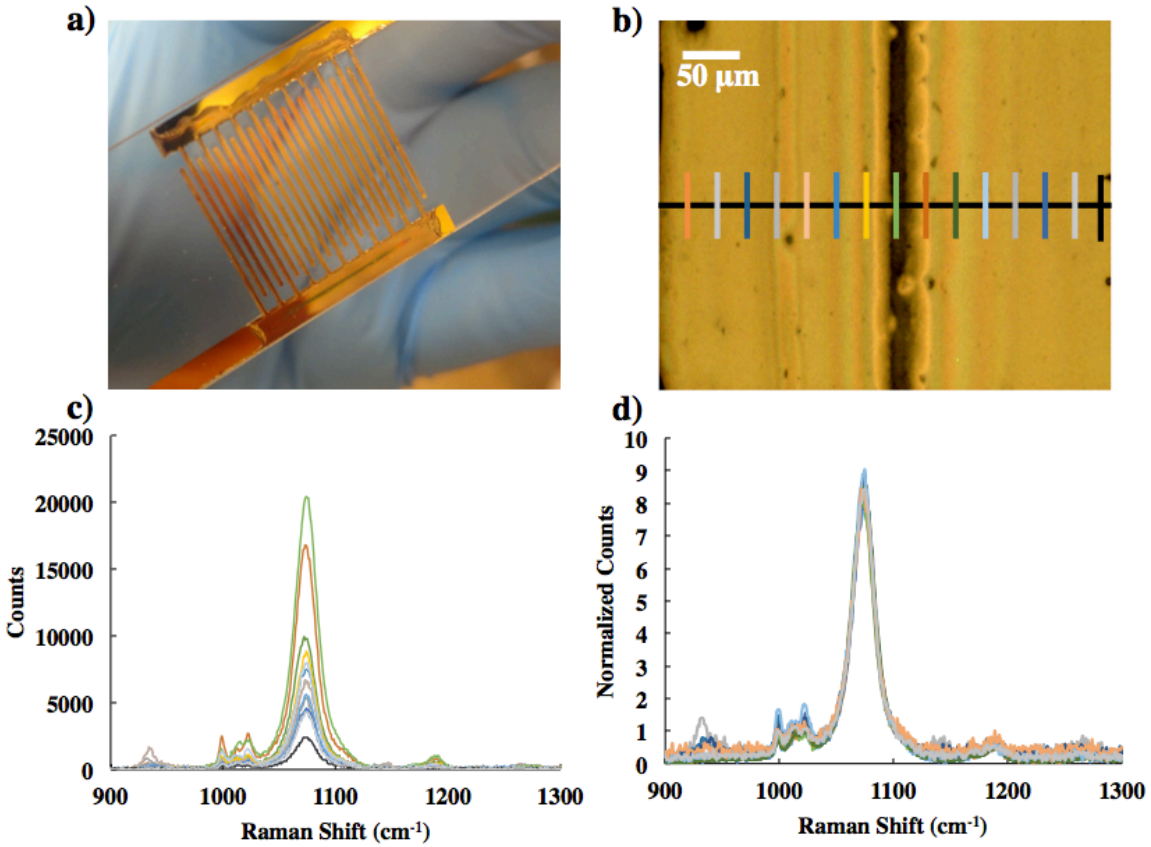

Figure 6.5. a) The as-fabricated DEP-SERS chip in the IDE configuration. b) Optical image of an individual IDE, which shows concentrated PS nanoparticles in the center of the electrode. b) SERS spectra of 4-MPBA collected laterally across the IDE in a) with ~ 50 µm increments. The color key is matched to where the spectra were collected from on the IDE in b). d) SERS spectra in c) standardized with the standard normal variate method.

The non-uniform distribution of PS nanospheres can lead to variance in SERS spectra of small molecules due to the increase in the hot spot density of multilayered nanospheres. However, for large microorganisms such as bacterial cells the sequestered hot spots will be inaccessible, and thus SERS will only occur on the outermost nanosphere layer producing uniform signals. Obtaining uniform coverage of nanospheres on the IDEs is currently under investigation. One possible route to nanosphere monolayers is to replace the sulfate surface groups with carboxyl groups. An increase in the surface concentration of carboxyl groups on the nanospheres leads to an increased surface charge density that allows individual nanospheres to overcome electrostatic repulsion forces.[187, 188] Overcoming the electrostatic repulsion forces enables spontaneous packing of the nanospheres on planar surfaces, and surfaces with hierarchical micron-scale surfaces such as IDEs.

The SERS signal frequency dependence of surface bound 4-MPBA was studied in the range of 500 Hz – 10 MHz. As discussed in Chapter 4, spectral invariance was observed on the SERS spectra of Gram-negative and Gram-positive bacterial cells, implying that the cellular structure was unaltered by the applied DEP field. However, it is also necessary to determine if the applied DEP field will alter the electromagnetic properties of LSPR. To investigate the effects of DEP on LSPR, the DEP-SERS device was submerged in DI H_2O and SERS spectra of 4-MPBA were collected at different applied frequencies. The baseline corrected and normalized spectra displayed spectral invariance with respect to the DEP condition (Fig. 6.6a). The spectra were further processed by principal component analysis (PCA). Similar to the results presented in Fig. 4.6, no definitive groupings were observed for different DEP conditions, which indicates the LSPR is unaffected by applied DEP field (Fig. 6.6b).

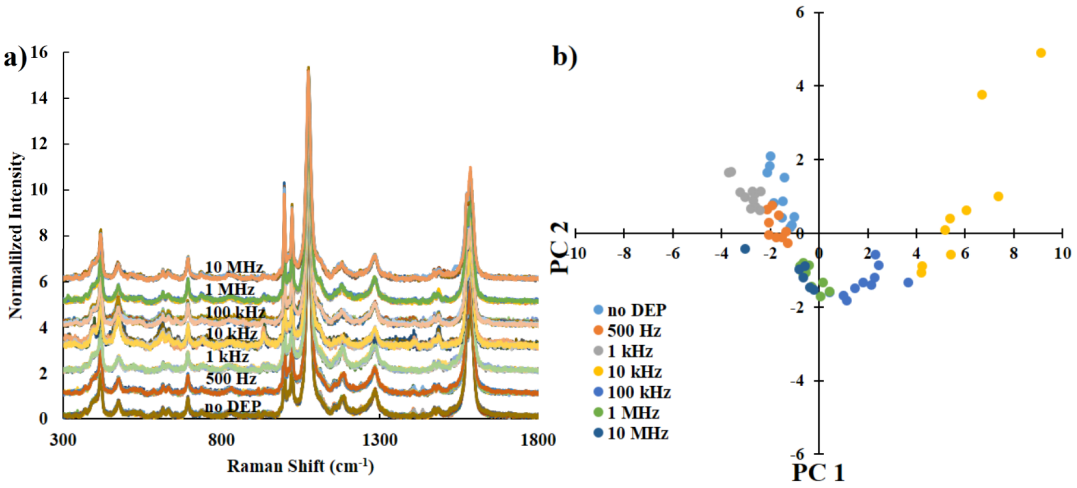

Figure 6.6. a) SERS spectra of 4-MPBA collected with different no DEP and applied frequencies of 500 Hz – 10 MHz. Ten spectra were collected for each DEP configuration. c) Principal component analysis of the spectra collected in b), with PC1 and PC2 accounting for 46.3% and 9.6% of the variance in the dataset, respectively.

6.4 CONCLUSIONS

A DEP-SERS device for bacterial separation and detection was designed with MFON structures on IDEs. The plasmonic behaviors of the MFON structures were investigated with FDTD simulations, and the optimized diameter was found to be 200 nm. The devices showed a non-uniform nanosphere distribution, with a concentrated band of nanospheres in the center of individual electrodes. However, the SERS intensities of the bare substrates were found to be stable across the device. Future work to improve the monolayer fidelity will be focused on the use of carboxylated PS nanospheres. The separation abilities of the DEP-SERS device on *E. coli* and *S. epidermidis* bacterial mixtures will then be assessed.

Chapter 7. CONCLUSIONS AND OUTLOOK

7.1 CONCLUSIONS

The work presented here has focused on improving bacterial detection performance characteristics in plasmonic biosensors, including surface-enhanced Raman scattering (SERS) and surface plasmon resonance (SPR) – based approaches. The overarching goal of the studies has been to provide rapid, sensitive, and selective detection of bacterial pathogens. Technologies to achieve this goal are urgently needed for environmental, homeland defense, and medical applications. The conclusions and observations drawn from this work can help aid future research and development to obtain effective bacterial detection.

My initial studies investigated the incorporation of long-range surface plasmons (LR-SPs) into extend the effective sensing volume near SERS-active nanostructures. Extensive finite-difference time domain (FDTD) simulations were conducted to help understand how the geometric parameters and dielectric environment of the nanoscale features affected the resultant SERS-active electric field. With the pitch of neighboring nanostructures fixed at 604 nm from theoretical calculations, the nanohole diameter, dielectric thickness, and the presence of an underlying “resonant mirror” were varied.

We found that the resonant mirror and a refractive index-matched buffer layer were critical to electric field extension to increase the effective sensing volume of the SERS-active nanostructures. The refractive index-matched buffer layer allowed for the momentum of surface plasmons on either side of the nanostructured, metal film to match, and sustain LR-SPs. The resonant mirror proved necessary to prevent leakage of light from the device. Coupling between the resonant mirror and metal nanostructured resulted in a Fabry-Perot nanocavity, which could be further tuned by adjusting the thickness of the index-matched buffer layer. The FDTD

simulations allowed us to optimize the nanoscale features and plasmonic response of the SERS-active devices prior to fabrication.

Fabrication of the SERS-active nanostructures sustaining LR-SPs (LR-SERS substrates) was accomplished through solvent-assisted nanomolding (SANM). The SAMN process used poly(dimethyl siloxane) (PDMS) molds cast from a Si master mold that contained nanopillars with the dimensions of the FDTD optimized nanostructures. The PDMS molds were used to transfer the nanopatterns into a sacrificial polymer layer. The nanohole arrays were realized after plasma etching to remove the residual sacrificial polymer, and deposition of gold.

The SERS performance of the LR-SERS substrates was drastically improved compared to conventional nanohole arrays (i.e. Au nanohole arrays directly on glass substrates). Self-assembled monolayers (SAMs) of 4-mercaptobenzoic acid (4-MBA) were used to probe the SERS enhancements of LR-SERS and conventional substrates. The optimized LR-SERS substrates displayed a ~28x signal enhancement of the 4-MBA SAMs over the conventional substrates. Furthermore, the LR-SERS substrates enabled successful detection of aqueous phase analytes ~10 nm from the nanostructured surfaces, which was not observed in the conventional substrates. The increased sensitivity of the LR-SERS substrates could be used for sensitive detection of bacterial suspensions.

A large part of my work aimed at integration of dielectrophoresis (DEP) into SERS and SPR biosensors. Micron-scale bacteria are highly amenable to spatial manipulation through externally applied DEP. We speculated that the additional DEP force could overcome inherent mass-transport limitations in SERS and SPR biosensors. Typically, bacterial mass transport is limited by diffusion to the SERS or SPR sensing surface, an inherently slow process. By capitalizing on the inherent conductivity of Au surfaces used in plasmonic biosensing, we were

able to convert the SERS and SPR surfaces into dually functional electrodes: electrodes which sustain the propagation of surface plasmons and are DEP-active.

We first explored the development of a SERS, microfluidic biosensor with DEP capabilities. Both fundamental and applied studies were conducted. SERS biosensors with DEP-active electrodes have been previously developed for bacterial detection. However, a systemic investigation to understand how the external DEP field interacts with the localized surface plasmons, and therefore SERS bacterial signatures was lacking in the literature.

A point-and-plate electrode configuration was developed using quasi-3-dimensional nanostructures as both the SERS-active surface and DEP-active electrode. The "point" and "plate" electrodes were situated on opposite sides of a 90 μm microchannel to allow for dynamic trapping and detection. Polystyrene (PS) microspheres, used to model bacteria, displayed particle trapping dynamics in good agreement with theoretical Clausius-Mossotti (CM) factor calculations. A single crossover frequency (COF) of 7.93 x 10^5 Hz was predicted for PS microspheres suspended in DI H_2O. PS microspheres were successfully trapped with frequencies in the positive DEP (pDEP) region below the COF ranging from 500 Hz – 100 kHz, whereas negative DEP (nDEP) repelled the microspheres from the point electrode for frequencies of 1 and 10 MHz. Dynamic trapping of *E. coli* cells was also in good agreement with theoretical CM factor calculations, which remained in the pDEP region for the entire 500 Hz – 10 MHz frequency range. The device enabled the dynamic detection of *E. coli* at concentrations of 10^5 CFU/mL, three orders of magnitudes lower than Q3D arrays in the diffusion-limited regime.

Statistical analyses on SERS spectra of Gram-negative *E. coli* and Gram-positive *S. epidermidis* were conducted over the 500 Hz – 10 MHz frequency range, which revealed an

independence of the SERS features with respect to the applied DEP frequency. Principal component analysis (PCA) was employed to group the individual SERS spectra based on subtle differences in the spectra at different frequencies. No identifiable frequency-based clustering was observed, and only 23% and 33% of the variance in the datasets was explained by the first principle component for *E. coli* and *S. epidermidis*, respectively. Three machine learning algorithms, k-nearest neighbor (kNN), linear discriminant analysis (LDA), and support vector machine (SVM) were employed to further classify the spectra with respect to the applied DEP frequency. Bacterial spectra were classified with accuracies ranging from 50 – 88% accuracy for datasets segregated between *E. coli* and *S. epidermidis*. However, combining the datasets led to a classification accuracy of 100% for all three classifiers. Therefore, the DEP-SERS device developed in this work can successfully increase the mass transport of bacteria to the nanostructured surface, reducing the limit of detection, and the SERS spectra were found to be independent of the DEP frequency at which the detection occurred.

Finally, we developed dually functional electrodes for DEP-enhanced SPR detection of bacteria. Conventional SPR chips, consisting of ~50 nm Au films on glass substrates, were modified with micron-sized interdigitated electrodes (IDEs). The plasmon generation, inherent sensitivity, and bacterial detection properties of interdigitated SPR (iSPR) chips were investigated and compared to conventional chips.

Surface plasmon generation on iSPR chips was found to be dependent on electrode width, and the propagation length of SPs. iSPR chips with electrode widths of 10 and 20 μm poorly coupled SPs on the electrode surfaces, whereas 100 μm electrodes generation SPR comparable to the conventional chip. The poor coupling of narrow electrodes was attributed to the propagation length of SPs near at excitation source of 750 nm. In this range SPs have a propagation length of

~20 μm. Therefore, the discontinuities in the Au film from the electrode gaps prevented propagation and sustention of SPs, resulting in poor coupling of SPs and poor SPR resolution. Strong SP coupling on wide (100 μm) IDEs produced a similar sensitivity response from the iSPR chips when compared to the conventional chips.

The iSPR chips enabled sensitive, rapid, and selective *E. coli*. Compared to the conventional chips, operating in the diffusion-limited regime, DEP-enhanced mass transport of *E. coli* with iSPR chips led to a nearly five orders of magnitude improvement in the limit of detection (LOD) of *E. coli* suspensions. The LOD of iSPR chips was found to be 3 x 10^2 CFU/mL, well within the clinically relevant range (<10^5 CFU/mL). After baseline establishment, the detection was made in approximately 30 min. Furthermore, secondary antibody amplification enabled selective detection of *E. coli* over *S. epidermidis*. Highly concentrated S. epidermidis suspensions (10^7 and 10^8 CFU/mL) produced no secondary response when exposed to anti-*E. coli* polyclonal antibodies (PAb). However, after immobilization of 10^3 CFU/mL *E. coli* suspensions, a large secondary response to PAb was observed. Therefore, not only can the DEP-SPR strategy detect dilute bacterial targets, but it can also do so selectively in ~2 h. This strategy could be further developed for a host of applications where sensitive, rapid, and selective bacterial detection is desired.

7.2 OUTLOOK

My work investigating novel approaches in SERS and SPR-based bacterial biosensing has made contributions to the larger field of bacterial diagnostics. While vast improvements in biosensing technologies have been made in recent years, culture-based methods remain the gold standard for bacterial diagnosis. Culture-based methods, while inherently time consuming and therefore expensive, are extraordinarily reliable with a proven track record and standardized

operating procedures. The strengths of culture-based methods have effectively prevented biosensing technologies, still in their infancy, from gaining a larger market share. Biosensing technologies will continually be developed and improved, inevitably making them more competitive with culture-based methods.

Regardless of the biosensor subcategory (i.e. electrochemical, genotypical, optical, etc.), the overall process flows for bacterial detection can be broken down into four essential sections: sample preparation, transduction, signal processing, and diagnosis. Eventually, the size of the instruments used for biosensing will need to be reduced to enable truly point-of-care and field-based applications. Improvements to any of these four categories will lead to more effective biosensing technologies.

The work presented here was primarily focused on improving the sensitivity of optical-based transduction for model systems. Therefore, future work should be focused on further improvements in transduction as well as sample preparation and signal processing. While the sensitivity of the developed strategies (i.e. limits of detection) is well within the clinically relevant range ($<10^5$ CFU/mL), the selectivity of the strategies could be drastically improved. Future efforts to incorporate highly selective biorecognition elements such as antibodies, aptamers, and polysaccharides should take priority. Applications with real-world samples will necessitate the use of non-fouling surfaces and pre-filtration to prevent contamination from small molecules and large debris, respectively.

Rapid bacterial diagnosis is complex problem that is difficult to solve, but nevertheless an important one as bacterial infections will remain a global burden. The CDC estimates that in the United States alone, over 20,000 deaths are attributed to drug resistant bacterial infections per year. Slow diagnosis times with culture-based techniques has led to increased use of wide-

spectrum antibiotics, and increased prevalence of drug resistant bacteria. Biosensing technologies will inevitably replace culture-based techniques allowing for real-time diagnosis and prescription of highly targeted antibiotic treatments, thereby eliminating stress on bacteria to develop further defense mechanisms.

REFERENCES

1. Swaminathan, B.; Feng, P., RAPID DETECTION OF FOOD-BORNE PATHOGENIC BACTERIA. *Annual Review of Microbiology* **1994,** *48*, 401-426.

2. Ivnitski, D.; Abdel-Hamid, I.; Atanasov, P.; Wilkins, E., Biosensors for detection of pathogenic bacteria. *Biosensors & Bioelectronics* **1999,** *14* (7), 599-624.

3. Ahmed, A.; Rushworth, J. V.; Hirst, N. A.; Millner, P. A., Biosensors for Whole-Cell Bacterial Detection. *Clinical Microbiology Reviews* **2014,** *27* (3), 631-646.

4. Scallan, E.; Griffin, P. M.; Angulo, F. J.; Tauxe, R. V.; Hoekstra, R. M., Foodborne Illness Acquired in the United States-Unspecified Agents. *Emerging Infectious Diseases* **2011,** *17* (1), 16-22.

5. Scharff, R. L., State Estimates for the Annual Cost of Foodborne Illness. *Journal of Food Protection* **2015,** *78* (6), 1064-1071.

6. Chambers, H. F.; Deleo, F. R., Waves of resistance: Staphylococcus aureus in the antibiotic era. *Nature Reviews Microbiology* **2009,** *7* (9), 629-641.

7. Lewis, K., Persister Cells. *Annual Review of Microbiology, Vol 64, 2010* **2010,** *64*, 357-372.

8. Bradley, J. S., Which antibiotic for resistant Gram-positives, and why? *Journal of Infection* **2014,** *68*, S63-S75.

9. Salazar, E., The United States Market For In Vitro Diagnostic Tests. Kalorama Information Market Intelligence Reports: 2014.

10. Beyond Plates: Rapid, Automated Diagnosis of Antimicrobial Susceptiblity. https://www.cbdstconference.com/sessions-2017/sessiondescriptions (accessed July 6, 2017).

11. Turner, A. P. F., Biosensors: sense and sensibility. *Chemical Society Reviews* **2013,** *42* (8), 3184-3196.

12. Van Dorst, B.; Mehta, J.; Bekaert, K.; Rouah-Martin, E.; De Coen, W.; Dubruel, P.; Blust, R.; Robbens, J., Recent advances in recognition elements of food and environmental biosensors: A review. *Biosensors & Bioelectronics* **2010,** *26* (4), 1178-1194.

13. Vikesland, P. J.; Wigginton, K. R., Nanomaterial Enabled Biosensors for Pathogen Monitoring - A Review. *Environmental Science & Technology* **2010,** *44* (10), 3656-3669.

14. Justino, C. I. L.; Freitas, A. C.; Pereira, R.; Duarte, A. C.; Santos, T., Recent developments in recognition elements for chemical sensors and biosensors. *Trac-Trends in Analytical Chemistry* **2015,** *68*, 2-17.

15. Chen, H.; Huang, J. F.; Palaniappan, A.; Wang, Y.; Liedberg, B.; Platt, M.; Tok, A. I. Y., A review on electronic bio-sensing approaches based on non-antibody recognition elements. *Analyst* **2016,** *141* (8), 2335-2346.

16. Templier, V.; Roux, A.; Roupioz, Y.; Livache, T., Ligands for label-free detection of whole bacteria on biosensors: A review. *Trac-Trends in Analytical Chemistry* **2016,** *79*, 71-79.

17. Liu, Y.; Zhou, H. B.; Hu, Z. W.; Yu, G. X.; Yang, D. T.; Zhao, J. S., Label and label-free based surface-enhanced Raman scattering for pathogen bacteria detection: A review. *Biosensors & Bioelectronics* **2017,** *94*, 131-140.

18. Homola, J.; Yee, S. S.; Gauglitz, G., Surface plasmon resonance sensors: review. *Sensors and Actuators B-Chemical* **1999,** *54* (1-2), 3-15.

19. Hanlon, E. B.; Manoharan, R.; Koo, T. W.; Shafer, K. E.; Motz, J. T.; Fitzmaurice, M.; Kramer, J. R.; Itzkan, I.; Dasari, R. R.; Feld, M. S., Prospects for in vivo Raman spectroscopy. *Physics in Medicine and Biology* **2000,** *45* (2), R1-R59.

20. Czamara, K.; Majzner, K.; Pacia, M. Z.; Kochan, K.; Kaczor, A.; Baranska, M., Raman spectroscopy of lipids: a review. *Journal of Raman Spectroscopy* **2015,** *46* (1), 4-20.

21. Munchberg, U.; Rosch, P.; Bauer, M.; Popp, J., Raman spectroscopic identification of single bacterial cells under antibiotic influence. *Analytical and Bioanalytical Chemistry* **2014,** *406* (13), 3041-3050.

22. Kastanosa, E. K., A.; Hadjigeorgioub, K.; Pitrisb, P., Urinary Tract Infection Diagnosis and Response to Antibiotics Using Raman Spectroscopy. *Proc. of SPIE* **2009,** *7169*.

23. Moritz, T. J.; Polage, C. R.; Taylor, D. S.; Krol, D. M.; Lane, S. M.; Chan, J. W., Evaluation of Escherichia coli Cell Response to Antibiotic Treatment by Use of Raman Spectroscopy with Laser Tweezers. *Journal of Clinical Microbiology* **2010,** *48* (11), 4287-4290.

24. Walter, A.; Reinicke, M.; Bocklitz, T.; Schumacher, W.; Rosch, P.; Kothe, E.; Popp, J., Raman spectroscopic detection of physiology changes in plasmid-bearing Escherichia coli with and without antibiotic treatment. *Analytical and Bioanalytical Chemistry* **2011,** *400* (9), 2763-2773.

25. Williams, A. C.; Edwards, H. G. M., FOURIER-TRANSFORM RAMAN-SPECTROSCOPY OF BACTERIAL-CELL WALLS. *Journal of Raman Spectroscopy* **1994,** *25* (7-8), 673-677.

26. Choo-Smith, L. P.; Maquelin, K.; van Vreeswijk, T.; Bruining, H. A.; Puppels, G. J.; Thi, N. A. G.; Kirschner, C.; Naumann, D.; Ami, D.; Villa, A. M.; Orsini, F.; Doglia, S. M.; Lamfarraj, H.; Sockalingum, G. D.; Manfait, M.; Allouch, P.; Endtz, H. P., Investigating microbial (micro)colony heterogeneity by vibrational spectroscopy. *Applied and Environmental Microbiology* **2001,** *67* (4), 1461-1469.

27. Maquelin, K.; Kirschner, C.; Choo-Smith, L. P.; van den Braak, N.; Endtz, H. P.; Naumann, D.; Puppels, G. J., Identification of medically relevant microorganisms by vibrational spectroscopy. *Journal of Microbiological Methods* **2002,** *51* (3), 255-271.

28. Tu, A. T., *Raman Spectroscopy in Biology: Principles and Applications*. Wiley: New York, 1982.

29. Fleischmann, M.; Hendra, P. J.; McQuilla.Aj, RAMAN-SPECTRA OF PYRIDINE ADSORBED AT A SILVER ELECTRODE. *Chemical Physics Letters* **1974,** *26* (2), 163-166.

30. Jeanmaire, D. L.; Vanduyne, R. P., SURFACE RAMAN SPECTROELECTROCHEMISTRY .1. HETEROCYCLIC, AROMATIC, AND ALIPHATIC-AMINES ADSORBED ON ANODIZED SILVER ELECTRODE. *Journal of Electroanalytical Chemistry* **1977,** *84* (1), 1-20.

31. Albrecht, M. G.; Creighton, J. A., ANOMALOUSLY INTENSE RAMAN-SPECTRA OF PYRIDINE AT A SILVER ELECTRODE. *Journal of the American Chemical Society* **1977,** *99* (15), 5215-5217.

32. King, F. W.; Vanduyne, R. P.; Schatz, G. C., THEORY OF RAMAN-SCATTERING BY MOLECULES ADSORBED ON ELECTRODE SURFACES. *Journal of Chemical Physics* **1978,** *69* (10), 4472-4481.

33. McNay, G.; Eustace, D.; Smith, W. E.; Faulds, K.; Graham, D., Surface-Enhanced Raman Scattering (SERS) and Surface-Enhanced Resonance Raman Scattering (SERRS): A Review of Applications. *Applied Spectroscopy* **2011,** *65* (8), 825-837.

34. Stiles, P. L.; Dieringer, J. A.; Shah, N. C.; Van Duyne, R. R., Surface-Enhanced Raman Spectroscopy. *Annual Review of Analytical Chemistry* **2008,** *1*, 601-626.

35. Valley, N.; Greeneltch, N.; Van Duyne, R. P.; Schatz, G. C., A Look at the Origin and Magnitude of the Chemical Contribution to the Enhancement Mechanism of Surface-Enhanced Raman Spectroscopy (SERS): Theory and Experiment. *Journal of Physical Chemistry Letters* **2013,** *4* (16), 2599-2604.

36. Schatz, G. C.; Van Duyne, R. P., Electromagnetic Mechanism of Surface-enhanced Spectroscopy. In *Handbook of Vibrational Spectroscopy*, Chalmers, J. M.; Griffiths, P. R., Eds. Wiley: New York, 2002; pp 759-774.

37. Willets, K. A.; Van Duyne, R. P., Localized surface plasmon resonance spectroscopy and sensing. *Annual Review of Physical Chemistry* **2007,** *58*, 267-297.

38. Brown, L.; Wolf, J. M.; Prados-Rosales, R.; Casadevall, A., Through the wall: extracellular vesicles in Gram-positive bacteria, mycobacteria and fungi. *Nature Reviews Microbiology* **2015,** *13* (10), 620-630.

39. Homola, J., Surface plasmon resonance sensors for detection of chemical and biological species. *Chemical Reviews* **2008,** *108* (2), 462-493.

40. Jarvis, R. M.; Goodacre, R., Discrimination of bacteria using surface-enhanced Raman spectroscopy. *Analytical Chemistry* **2004,** *76* (1), 40-47.

41. Xu, J.; Turner, J. W.; Idso, M.; Biryukov, S. V.; Rognstad, L.; Gong, H.; Trainer, V. L.; Wells, M. L.; Strom, M. S.; Yu, Q., In Situ Strain-Level Detection and Identification of Vibrio parahaemolyticus Using Surface-Enhanced Raman Spectroscopy. *Analytical Chemistry* **2013,** *85* (5), 2630-2637.

42. Fernandez, R. E.; Rohani, A.; Farmehini, V.; Swami, N. S., Review: Microbial analysis in dielectrophoretic microfluidic systems. *Analytica Chimica Acta* **2017,** *966*, 11-33.

43. Mouffouk, F.; da Costa, A. M. R.; Martins, J.; Zourob, M.; Abu-Salah, K. M.; Alrokayan, S. A., Development of a highly sensitive bacteria detection assay using fluorescent pH-responsive polymeric micelles. *Biosensors & Bioelectronics* **2011,** *26* (8), 3517-3523.

44. Wang, Y.; Knoll, W.; Dostalek, J., Bacterial Pathogen Surface Plasmon Resonance Biosensor Advanced by Long Range Surface Plasmons and Magnetic Nanoparticle Assays. *Analytical Chemistry* **2012,** *84* (19), 8345-8350.

45. Nguyen, H. H.; Park, J.; Kang, S.; Kim, M., Surface Plasmon Resonance: A Versatile Technique for Biosensor Applications. *Sensors* **2015,** *15* (5), 10481-10510.

46. Murray, C. A.; Allara, D. L.; Rhinewine, M., SILVER-MOLECULE SEPARATION DEPENDENCE OF SURFACE-ENHANCED RAMAN-SCATTERING. *Physical Review Letters* **1981,** *46* (1), 57-60.

47. Kennedy, B. J.; Spaeth, S.; Dickey, M.; Carron, K. T., Determination of the distance dependence and experimental effects for modified SERS substrates based on self-assembled monolayers formed using alkanethiols. *Journal of Physical Chemistry B* **1999,** *103* (18), 3640-3646.

48. Whitney, A. V.; Elam, J. W.; Zou, S. L.; Zinovev, A. V.; Stair, P. C.; Schatz, G. C.; Van Duyne, R. P., Localized surface plasmon resonance nanosensor: A high-resolution distance-dependence study using atomic layer deposition. *Journal of Physical Chemistry B* **2005,** *109* (43), 20522-20528.

49. Kumari, G.; Kandula, J.; Narayana, C., How Far Can We Probe by SERS? *Journal of Physical Chemistry C* **2015,** *119* (34), 20057-20064.

50. Lin, H. Y.; Huang, C. H.; Hsieh, W. H.; Liu, L. H.; Lin, Y. C.; Chu, C. C.; Wang, S. T.; Kuo, I. T.; Chau, L. K.; Yang, C. Y., On-line SERS Detection of Single Bacterium Using Novel SERS Nanoprobes and A Microfluidic Dielectrophoresis Device. *Small* **2014,** *10* (22), 4700-4710.

51. Gervais, T.; Jensen, K. F., Mass transport and surface reactions in microfluidic systems. *Chemical Engineering Science* **2006,** *61* (4), 1102-1121.

52. Singh, A. K.; Khan, S. A.; Fan, Z.; Demeritte, T.; Senapati, D.; Kanchanapally, R.; Ray, P. C., Development of a Long-Range Surface-Enhanced Raman Spectroscopy Ruler. *Journal of the American Chemical Society* **2012,** *134* (20), 8662-8669.

53. Liu, Y.; Xu, S. P.; Xuan, X. Y.; Zhao, B.; Xu, W. Q., Long-Range Surface Plasmon Field-Enhanced Raman Scattering Spectroscopy Based on Evanescent Field Excitation. *Journal of Physical Chemistry Letters* **2011,** *2* (17), 2218-2222.

54. Xuan, X. Y.; Xu, S. P.; Liu, Y.; Li, H. B.; Xu, W. Q.; Lombardi, J. R., A Long-Range Surface Plasmon Resonance/Probe/Silver Nanoparticle (LRSPR-P-NP) Nanoantenna Configuration for Surface-Enhanced Raman Scattering. *Journal of Physical Chemistry Letters* **2012,** *3* (19), 2773-2778.

55. Berini, P., Long-range surface plasmon polaritons. *Advances in Optics and Photonics* **2009,** *1* (3), 484-588.

56. Nenninger, G. G.; Tobiska, P.; Homola, J.; Yee, S. S., Long-range surface plasmons for high-resolution surface plasmon resonance sensors. *Sensors and Actuators B-Chemical* **2001,** *74* (1-3), 145-151.

57. Sarid, D., LONG-RANGE SURFACE-PLASMA WAVES ON VERY THIN METAL-FILMS. *Physical Review Letters* **1981,** *47* (26), 1927-1930.

58. Craig, A. E.; Olson, G. A.; Sarid, D., EXPERIMENTAL-OBSERVATION OF THE LONG-RANGE SURFACE-PLASMON POLARITON. *Optics Letters* **1983,** *8* (7), 380-382.

59. Dostalek, J.; Kasry, A.; Knoll, W., Long range surface plasmons for observation of biomolecular binding events at metallic surfaces. *Plasmonics* **2007,** *2* (3), 97-106.

60. Toma, K.; Dostalek, J.; Knoll, W., Long range surface plasmon-coupled fluorescence emission for biosensor applications. *Optics Express* **2011,** *19* (12), 11090-11099.

61. Vala, M.; Etheridge, S.; Roach, J. A.; Homola, J., Long-range surface plasmons for sensitive detection of bacterial analytes. *Sensors and Actuators B-Chemical* **2009,** *139* (1), 59-63.

62. Chabot, V.; Miron, Y.; Grandbois, M.; Charette, P. G., Long range surface plasmon resonance for increased sensitivity in living cell biosensing through greater probing depth. *Sensors and Actuators B-Chemical* **2012,** *174*, 94-101.

63. Schmiemann, G.; Kniehl, E.; Gebhardt, K.; Matejczyk, M. M.; Hummers-Pradier, E., The Diagnosis of Urinary Tract Infection A Systematic Review. *Deutsches Arzteblatt International* **2010,** *107* (21), 361-U9.

64. Avci, E.; Kaya, N. S.; Ucankus, G.; Culha, M., Discrimination of urinary tract infection pathogens by means of their growth profiles using surface enhanced Raman scattering. *Analytical and Bioanalytical Chemistry* **2015,** *407* (27), 8233-8241.

65. Wang, J. F.; Wu, X. Z.; Wang, C. W.; Shao, N. S.; Dong, P. T.; Xiao, R.; Wang, S. Q., Magnetically Assisted Surface-Enhanced Raman Spectroscopy for the Detection of Staphylococcus aureus Based on Aptamer Recognition. *Acs Applied Materials & Interfaces* **2015,** *7* (37), 20919-20929.

66. Zhang, L.; Xu, J. J.; Mi, L.; Gong, H.; Jiang, S. Y.; Yu, Q. M., Multifunctional magnetic-plasmonic nanoparticles for fast concentration and sensitive detection of bacteria using SERS. *Biosensors & Bioelectronics* **2012,** *31* (1), 130-136.

67. Walter, A.; Marz, A.; Schumacher, W.; Rosch, P.; Popp, J., Towards a fast, high specific and reliable discrimination of bacteria on strain level by means of SERS in a microfluidic device. *Lab on a Chip* **2011,** *11* (6), 1013-1021.

68. Cheng, I. F.; Chang, H. C.; Hou, D., An integrated dielectrophoretic chip for continuous bioparticle filtering, focusing, sorting, trapping, and detecting. *Biomicrofluidics* **2007,** *1* (2).

69. Cheng, I. F.; Lin, C. C.; Lin, D. Y.; Chang, H., A dielectrophoretic chip with a roughened metal surface for on-chip surface-enhanced Raman scattering analysis of bacteria. *Biomicrofluidics* **2010,** *4* (3).

70. Cheng, I. F.; Chang, H. C.; Chen, T. Y.; Hu, C. M.; Yang, F. L., Rapid (< 5 min) Identification of Pathogen in Human Blood by Electrokinetic Concentration and Surface-Enhanced Raman Spectroscopy. *Scientific Reports* **2013,** *3*.

71. Cheng, I. F.; Chen, T. Y.; Lu, R. J.; Wu, H. W., Rapid identification of bacteria utilizing amplified dielectrophoretic force-assisted nanoparticle-induced surface-enhanced Raman spectroscopy. *Nanoscale Research Letters* **2014,** *9*, 1-8.

72. Madiyar, F. R.; Bhana, S.; Swisher, L. Z.; Culbertson, C. T.; Huang, X. H.; Li, J., Integration of a nanostructured dielectrophoretic device and a surface-enhanced Raman probe for highly sensitive rapid bacteria detection. *Nanoscale* **2015,** *7* (8), 3726-3736.

73. Deng, Y. L.; Juang, Y. J., Electrokinetic trapping and surface enhanced Raman scattering detection of biomolecules using optofluidic device integrated with a microneedles array. *Biomicrofluidics* **2013,** *7* (1).

74. Pohl, H. A., *Dielectrophoresis: the behavior of neutral matter in non-uniform electric fields*. Cambridge University Press: New York, 1978.

75. Sun, T.; Holmes, D.; Gawad, S.; Green, N. G.; Morgan, H., High speed multi-frequency impedance analysis of single particles in a microfluidic cytometer using maximum length sequences. *Lab on a Chip* **2007,** *7* (8), 1034-1040.

76. Pethig, R., Review Article-Dielectrophoresis: Status of the theory, technology, and applications. *Biomicrofluidics* **2010,** *4* (2).

77. Morgan, H.; Izquierdo, A. G.; Bakewell, D.; Green, N. G.; Ramos, A., The dielectrophoretic and travelling wave forces generated by interdigitated electrode arrays:

analytical solution using Fourier series. *Journal of Physics D-Applied Physics* **2001,** *34* (10), 1553-1561.

78. Kunz, K. S.; Luebbers, R. J., *The Finite Difference Time Domain Method for Electromagnetics*. CRC Press: Boca Raton, 1993.

79. Taflove, A., Review of the Formulation and Applications of the Finite-Difference Time-Domain Method for Numerical Modeling of Electromagnetic Wave Interactions with Arbitrary Structures. *Wave Motion* **1988,** *10*, 547-582.

80. Haynes, C. L.; Van Duyne, R. P., Plasmon-sampled surface-enhanced Raman excitation spectroscopy. *Journal of Physical Chemistry B* **2003,** *107* (30), 7426-7433.

81. Chang, S. H.; Gray, S. K.; Schatz, G. C., Surface plasmon generation and light transmission by isolated nanoholes and arrays of nanoholes in thin metal films. *Optics Express* **2005,** *13* (8), 3150-3165.

82. Uzayisenga, V.; Lin, X. D.; Li, L. M.; Anema, J. R.; Yang, Z. L.; Huang, Y. F.; Lin, H. X.; Li, S. B.; Li, J. F.; Tian, Z. Q., Synthesis, Characterization, and 3D-FDTD Simulation of Ag@SiO2 Nanoparticles for Shell-Isolated Nanoparticle-Enhanced Raman Spectroscopy. *Langmuir* **2012,** *28* (24), 9140-9146.

83. Xu, J.; Zhang, L.; Gong, H.; Homola, J.; Yu, Q., Tailoring Plasmonic Nanostructures for Optimal SERS Sensing of Small Molecules and Large Microorganisms. *Small* **2011,** *7* (3), 371-376.

84. Homola, J., *Surface Plasmon Resonance Based Biosensors*. Springer: 2006.

85. Johnson, P. B.; Christy, R. W., OPTICAL CONSTANTS OF NOBLE METALS. *Physical Review B* **1972,** *6* (12), 4370-4379.

86. Born, M.; Wolf, E., *Principles of Optics*. 7th (expanded) edition ed.; Cambridge University Press: New York, 1999.

87. Blaber, M. G.; Schatz, G. C., Extending SERS into the infrared with gold nanosphere dimers. *Chemical Communications* **2011,** *47* (13), 3769-3771.

88. Stewart, M. E.; Mack, N. H.; Malyarchuk, V.; Soares, J.; Lee, T. W.; Gray, S. K.; Nuzzo, R. G.; Rogers, J. A., Quantitative multispectral biosensing and 1D imaging using quasi-3D plasmonic crystals. *Proceedings of the National Academy of Sciences of the United States of America* **2006,** *103* (46), 17143-17148.

89. Artar, A.; Yanik, A. A.; Altug, H., Fabry-Peacuterot nanocavities in multilayered plasmonic crystals for enhanced biosensing. *Applied Physics Letters* **2009,** *95* (5).

90. Xu, J. J.; Guan, P.; Kvasnicka, P.; Gong, H.; Homola, J.; Yu, Q. M., Light Transmission and Surface-Enhanced Raman Scattering of Quasi-3D Plasmonic Nanostructure

Arrays with Deep and Shallow Fabry-Perot Nanocavities. *Journal of Physical Chemistry C* **2011,** *115* (22), 10996-11002.

91. Xu, J.; Kvasnicka, P.; Idso, M.; Jordan, R. W.; Gong, H.; Homola, J.; Yu, Q., Understanding the effects of dielectric medium, substrate, and depth on electric fields and SERS of quasi-3D plasmonic nanostructures. *Optics Express* **2011,** *19* (21), 20493-20505.

92. Jarvis, R. M.; Law, N.; Shadi, L. T.; O'Brien, P.; Lloyd, J. R.; Goodacre, R., Surface-enhanced Raman scattering from intracellular and extracellular bacterial locations. *Analytical Chemistry* **2008,** *80* (17), 6741-6746.

93. Schluecker, S., Surface-Enhanced Raman Spectroscopy: Concepts and Chemical Applications. *Angewandte Chemie-International Edition* **2014,** *53* (19), 4756-4795.

94. Leopold, N.; Lendl, B., A new method for fast preparation of highly surface-enhanced Raman scattering (SERS) active silver colloids at room temperature by reduction of silver nitrate with hydroxylamine hydrochloride. *Journal of Physical Chemistry B* **2003,** *107* (24), 5723-5727.

95. Brolo, A. G.; Arctander, E.; Gordon, R.; Leathem, B.; Kavanagh, K. L., Nanohole-enhanced Raman scattering. *Nano Letters* **2004,** *4* (10), 2015-2018.

96. Sannomiya, T.; Scholder, O.; Jefimovs, K.; Hafner, C.; Dahlin, A. B., Investigation of Plasmon Resonances in Metal Films with Nanohole Arrays for Biosensing Applications. *Small* **2011,** *7* (12), 1653-1663.

97. Escobedo, C., On-chip nanohole array based sensing: a review. *Lab on a Chip* **2013,** *13* (13), 2445-2463.

98. Ebbesen, T. W.; Lezec, H. J.; Ghaemi, H. F.; Thio, T.; Wolff, P. A., Extraordinary optical transmission through sub-wavelength hole arrays. *Nature* **1998,** *391* (6668), 667-669.

99. Schafer, C.; Kern, D. P.; Fleischer, M., Capturing molecules with plasmonic nanotips in microfluidic channels by dielectrophoresis. *Lab on a Chip* **2015,** *15* (4), 1066-1071.

100. Stewart, M. E.; Anderton, C. R.; Thompson, L. B.; Maria, J.; Gray, S. K.; Rogers, J. A.; Nuzzo, R. G., Nanostructured plasmonic sensors. *Chemical Reviews* **2008,** *108* (2), 494-521.

101. Haynes, C. L.; Van Duyne, R. P., Nanosphere lithography: A versatile nanofabrication tool for studies of size-dependent nanoparticle optics. *Journal of Physical Chemistry B* **2001,** *105* (24), 5599-5611.

102. Malinsky, M. D.; Kelly, K. L.; Schatz, G. C.; Van Duyne, R. P., Nanosphere lithography: Effect of substrate on the localized surface plasmon resonance spectrum of silver nanoparticles. *Journal of Physical Chemistry B* **2001,** *105* (12), 2343-2350.

103. Qin, D.; Xia, Y.; Whitesides, G. M., Soft lithography for micro- and nanoscale patterning. *Nature Protocols* **2010,** *5* (3), 491-502.

104. Chou, S. Y.; Krauss, P. R.; Renstrom, P. J., Nanoimprint lithography. *Journal of Vacuum Science & Technology B* **1996,** *14* (6), 4129-4133.

105. Jeon, S.; Menard, E.; Park, J. U.; Maria, J.; Meitl, M.; Zaumseil, J.; Rogers, J. A., Three-dimensional nanofabrication with rubber stamps and conformable photomasks. *Advanced Materials* **2004,** *16* (15), 1369-1373.

106. Kim, E.; Xia, Y. N.; Zhao, X. M.; Whitesides, G. M., Solvent-assisted microcontact molding: A convenient method for fabricating three-dimensional structures on surfaces of polymers. *Advanced Materials* **1997,** *9* (8), 651-654.

107. Xia, Y. N.; Zhao, X. M.; Kim, E.; Whitesides, G. M., A selective etching solution for use with patterned self-assembled monolayers of alkanethiolates on gold. *Chemistry of Materials* **1995,** *7* (12), 2332-2337.

108. Kumar, A.; Whitesides, G. M., FEATURES OF GOLD HAVING MICROMETER TO CENTIMETER DIMENSIONS CAN BE FORMED THROUGH A COMBINATION OF STAMPING WITH AN ELASTOMERIC STAMP AND AN ALKANETHIOL INK FOLLOWED BY CHEMICAL ETCHING. *Applied Physics Letters* **1993,** *63* (14), 2002-2004.

109. Bessueille, F.; Pla-Roca, M.; Mills, C. A.; Martinez, E.; Samitier, J.; Errachid, A., Submerged microcontact printing (S mu CP): An unconventional printing technique of thiols using high aspect ratio, elastomeric stamps. *Langmuir* **2005,** *21* (26), 12060-12063.

110. Leosson, K.; Ingason, A. S.; Agnarsson, B.; Kossoy, A.; Olafsson, S.; Gather, M. C., Ultra-thin gold films on transparent polymers. *Nanophotonics* **2013,** *2* (1), 3-11.

111. Kossoy, A.; Merk, V.; Simakov, D.; Leosson, K.; Kena-Cohen, S.; Maier, S. A., Optical and Structural Properties of Ultra-thin Gold Films. *Advanced Optical Materials* **2015,** *3* (1), 71-77.

112. Szafranski, C. A.; Tanner, W.; Laibinis, P. E.; Garrell, R. L., Surface-enhanced Raman spectroscopy of aromatic thiols and disulfides on gold electrodes. *Langmuir* **1998,** *14* (13), 3570-3579.

113. Han, S. W.; Lee, S. J.; Kim, K., Self-assembled monolayers of aromatic thiol and selenol on silver: Comparative study of adsorptivity and stability. *Langmuir* **2001,** *17* (22), 6981-6987.

114. Masango, S. S.; Hackler, R. A.; Large, N.; Henry, A.-I.; McAnally, M. O.; Schatz, G. C.; Stair, P. C.; Van Duyne, R. P., High-Resolution Distance Dependence Study of Surface-Enhanced Raman Scattering Enabled by Atomic Layer Deposition. *Nano Letters* **2016,** *16* (7), 4251-4259.

115. Hildebrandt, P.; Stockburger, M., SURFACE-ENHANCED RESONANCE RAMAN-SPECTROSCOPY OF RHODAMINE-6G ADSORBED ON COLLOIDAL SILVER. *Journal of Physical Chemistry* **1984,** *88* (24), 5935-5944.

116. Watanabe, H.; Hayazawa, N.; Inouye, Y.; Kawata, S., DFT vibrational calculations of Rhodamine 6G adsorbed on silver: Analysis of tip-enhanced Raman spectroscopy. *Journal of Physical Chemistry B* **2005,** *109* (11), 5012-5020.

117. Marston, H. D.; Dixon, D. M.; Knisely, J. M.; Palmore, T. N.; Fauci, A. S., Antimicrobial Resistance. *Jama-Journal of the American Medical Association* **2016,** *316* (11), 1193-1204.

118. Levy, S. B., The challenge of antibiotic resistance. *Scientific American* **1998,** *278* (3), 46-53.

119. Hart, C. A.; Kariuki, S., Antimicrobial resistance in developing countries. *British Medical Journal* **1998,** *317* (7159), 647-650.

120. Levy, S. B.; Marshall, B., Antibacterial resistance worldwide: causes, challenges and responses. *Nature Medicine* **2004,** *10* (12), S122-S129.

121. Lazcka, O.; Del Campo, F. J.; Munoz, F. X., Pathogen detection: A perspective of traditional methods and biosensors. *Biosensors & Bioelectronics* **2007,** *22* (7), 1205-1217.

122. Jarvis, R. M.; Brooker, A.; Goodacre, R., Surface-enhanced Raman scattering for the rapid discrimination of bacteria. *Faraday Discussions* **2006,** *132*, 281-292.

123. Huang, W. E.; Li, M. Q.; Jarvis, R. M.; Goodacre, R.; Banwart, S. A., Shining Light on the Microbial World: The Application of Raman Microspectroscopy. *Advances in Applied Microbiology* **2010,** *70*, 153-186.

124. Barik, A.; Otto, L. M.; Yoo, D.; Jose, J.; Johnson, T. W.; Oh, S. H., Dielectrophoresis-Enhanced Plasmonic Sensing with Gold Nanohole Arrays. *Nano Letters* **2014,** *14* (4), 2006-2012.

125. Liu, T. Y.; Tsai, K. T.; Wang, H. H.; Chen, Y.; Chen, Y. H.; Chao, Y. C.; Chang, H. H.; Lin, C. H.; Wang, J. K.; Wang, Y. L., Functionalized arrays of Raman-enhancing nanoparticles for capture and culture-free analysis of bacteria in human blood. *Nature Communications* **2011,** *2*.

126. Cheng, I. F.; Lin, C. C.; Lin, D. Y.; Chang, H., A dielectrophoretic chip with a roughened metal surface for on-chip surface-enhanced Raman scattering analysis of bacteria. *Biomicrofluidics* **2010,** *4* (3), 034104.

127. Cheng, I. F.; Chang, H. C.; Chen, T. Y.; Hu, C. M.; Yang, F. L., Rapid (< 5 min) Identification of Pathogen in Human Blood by Electrokinetic Concentration and Surface-Enhanced Raman Spectroscopy. *Scientific Reports* **2013,** *3* (2365).

128. Deng, Y. L.; Juang, Y. J., Electrokinetic trapping and surface enhanced Raman scattering detection of biomolecules using optofluidic device integrated with a microneedles array. *Biomicrofluidics* **2013,** *7* (1), 014111.

129. Pethig, R., Review Article-Dielectrophoresis: Status of the theory, technology, and applications. *Biomicrofluidics* **2010,** *4* (2), 022811.

130. Schroder, U. C.; Ramoji, A.; Glaser, U.; Sachse, S.; Leiterer, C.; Csaki, A.; Hubner, U.; Fritzsche, W.; Pfister, W.; Bauer, M.; Popp, J.; Neugebauer, U., Combined Dielectrophoresis-Raman Setup for the Classification of Pathogens Recovered from the Urinary Tract. *Analytical Chemistry* **2013,** *85* (22), 10717-10724.

131. Cherukulappurath, S.; Lee, S. H.; Campos, A.; Haynes, C. L.; Oh, S. H., Rapid and Sensitive in Situ SERS Detection Using Dielectrophoresis. *Chemistry of Materials* **2014,** *26* (7), 2445-2452.

132. Barik, A.; Cherukulappurath, S.; Wittenberg, N. J.; Johnson, T. W.; Oh, S. H., Dielectrophoresis-Assisted Raman Spectroscopy of Intravesicular Analytes on Metallic Pyramids. *Analytical Chemistry* **2016,** *88* (3), 1704-1710.

133. Folch, A., Introduction to BioMEMS. CRC Press: Boca Raton, 2013.

134. Sun, F.; Bai, T.; Zhang, L.; Ella-Menye, J.-R.; Liu, S.; Nowinski, A. K.; Jiang, S.; Yu, Q., Sensitive and Fast Detection of Fructose in Complex Media via Symmetry Breaking and Signal Amplification Using Surface-Enhanced Raman Spectroscopy. *Analytical Chemistry* **2014,** *86* (5), 2387-2394.

135. Sun, F.; Zhang, P.; Bai, T.; Galvan, D. D.; Hung, H. C.; Zhou, N.; Jiang, S. Y.; Yu, Q. M., Functionalized plasmonic nanostructure arrays for direct and accurate mapping extracellular pH of living cells in complex media using SERS. *Biosensors & Bioelectronics* **2015,** *73*, 202-207.

136. Sun, F.; Ella-Menye, J.-R.; Galvan, D. D.; Bai, T.; Hung, H.-C.; Chou, Y.-N.; Zhang, P.; Jiang, S.; Yu, Q., Stealth Surface Modification of Surface-Enhanced Raman Scattering Substrates for Sensitive and Accurate Detection in Protein Solutions. *Acs Nano* **2015,** *9* (3), 2668-2676.

137. Sun, F.; Hung, H. C.; Sinclair, A.; Zhang, P.; Bai, T.; Galvan, D. D.; Jain, P.; Li, B. W.; Jiang, S. Y.; Yu, Q. M., Hierarchical zwitterionic modification of a SERS substrate enables real-time drug monitoring in blood plasma. *Nature Communications* **2016,** *7*.

138. Deng, Y.; Idso, M. N.; Galvan, D. D.; Yu, Q. M., Optofluidic microsystem with quasi-3 dimensional gold plasmonic nanostructure arrays for online sensitive and reproducible SERS detection. *Analytica Chimica Acta* **2015,** *863*, 41-48.

139. Li, H. B.; Bashir, R., Dielectrophoretic separation and manipulation of live and heat-treated cells of Listeria on microfabricated devices with interdigitated electrodes. *Sensors and Actuators B-Chemical* **2002,** *86* (2-3), 215-221.

140. Yang, L.; Banada, P. P.; Bhunia, A. K.; Bashir, R., Effects of Dielectrophoresis on Growth, Viability and Immuno-reactivity of *Listeria monocytogenes*. *Journal of Biological Engineering* **2008,** *2* (6).

141. Castellarnau, M.; Errachid, A.; Madrid, C.; Juarez, A.; Samitier, J., Dielectrophoresis as a tool to characterize and differentiate isogenic mutants of Escherichia coli. *Biophysical Journal* **2006,** *91* (10), 3937-3945.

142. Asami, K.; Hanai, T.; Koizumi, N., DIELECTRIC ANALYSIS OF ESCHERICHIA-COLI SUSPENSIONS IN THE LIGHT OF THE THEORY OF INTERFACIAL POLARIZATION. *Biophysical Journal* **1980,** *31* (2), 215-228.

143. Efrima, S.; Zeiri, L., Understanding SERS of bacteria. *Journal of Raman Spectroscopy* **2009,** *40* (3), 277-288.

144. Bowden, M. G.; Chen, W.; Singvall, J.; Xu, Y.; Peacock, S. J.; Valtulina, V.; Speziale, P.; Hook, M., Identification and preliminary characterization of cell-wall-anchored proteins of Staphylococcus epidermidis. *Microbiology-Sgm* **2005,** *151*, 1453-1464.

145. Zhou, H. B.; Yang, D. T.; Ivleva, N. P.; Mircescu, N. E.; Schubert, S.; Niessner, R.; Wieser, A.; Haisch, C., Label-Free in Situ Discrimination of Live and Dead Bacteria by Surface-Enhanced Raman Scattering. *Analytical Chemistry* **2015,** *87* (13), 6553-6561.

146. Lu, X. N.; Samuelson, D. R.; Xu, Y. H.; Zhang, H. W.; Wang, S.; Rasco, B. A.; Xu, J.; Konkel, M. E., Detecting and Tracking Nosocomial Methicillin-Resistant Staphylococcus aureus Using a Microfluidic SERS Biosensor. *Analytical Chemistry* **2013,** *85* (4), 2320-2327.

147. Haley, R. W.; Culver, D. H.; White, J. W.; Morgan, W. M.; Emori, T. G., The Nationwide Nosocomial Infection-Rate - A New Need for Vital Statistics. *American Journal of Epidemiology* **1985,** *121* (2), 159-167.

148. Weinstein, R. A., Nosocomial infection update. *Emerging Infectious Diseases* **1998,** *4* (3), 416-420.

149. Taylor, A. D.; Ladd, J.; Yu, Q. M.; Chen, S. F.; Homola, J.; Jiang, S. Y., Quantitative and simultaneous detection of four foodborne bacterial pathogens with a multi-channel SPR sensor. *Biosensors & Bioelectronics* **2006,** *22* (5), 752-758.

150. Vaisocherova-Lisalova, H.; Visova, I.; Ermini, M. L.; Springer, T.; Song, X. C.; Mrazek, J.; Lamacova, J.; Lynn, N. S.; Sedivak, P.; Homola, J., Low-fouling surface plasmon resonance biosensor for multi-step detection of foodborne bacterial pathogens in complex food samples. *Biosensors & Bioelectronics* **2016,** *80*, 84-90.

151. Farka, Z.; Jurik, T.; Pastucha, M.; Skladal, P., Enzymatic Precipitation Enhanced Surface Plasmon Resonance Immunosensor for the Detection of Salmonella in Powdered Milk. *Analytical Chemistry* **2016,** *88* (23), 11830-11836.

152. Huang, C. J.; Dostalek, J.; Sessitsch, A.; Knoll, W., Long-Range Surface Plasmon-Enhanced Fluorescence Spectroscopy Biosensor for Ultrasensitive Detection of E. coli O157:H7. *Analytical Chemistry* **2011,** *83* (3), 674-677.

153. Huang, C. J.; Knoll, W.; Sessitsch, A.; Dostalek, J., SPR bacterial pathogen biosensor: The importance of fluidic conditions and probing depth. *Talanta* **2014,** *122*, 166-171.

154. Ruppel, N.; Troger, V.; Sandetskaya, N.; Kuhlmeier, D.; Schmieder, S.; Sonntag, F., Detection and identification of Staphylococcus aureus using magnetic particle enhanced surface plasmon spectroscopy. *Engineering in Life Sciences* **2018,** *18* (4), 263-268.

155. Liu, X.; Hu, Y. X.; Zheng, S.; Liu, Y.; He, Z.; Luo, F., Surface plasmon resonance immunosensor for fast, highly sensitive, and in situ detection of the magnetic nanoparticles-enriched Salmonella enteritidis. *Sensors and Actuators B-Chemical* **2016,** *230*, 191-198.

156. Pohl, H. A., THE MOTION AND PRECIPITATION OF SUSPENSOIDS IN DIVERGENT ELECTRIC FIELDS. *Journal of Applied Physics* **1951,** *22* (7), 869-871.

157. Hamada, R.; Takayama, H.; Shonishi, Y.; Mao, L.; Nakano, M.; Suehiro, J., A rapid bacteria detection technique utilizing impedance measurement combined with positive and negative dielectrophoresis. *Sensors and Actuators B-Chemical* **2013,** *181*, 439-445.

158. Kim, M.; Jung, T.; Kim, Y.; Lee, C.; Woo, K.; Seol, J. H.; Yang, S., A microfluidic device for label-free detection of Escherichia coli in drinking water using positive dielectrophoretic focusing, capturing, and impedance measurement. *Biosensors & Bioelectronics* **2015,** *74*, 1011-1015.

159. del Moral-Zamora, B.; Punter-Villagrassa, J.; Oliva-Branas, A. M.; Alvarez-Azpeitia, J. M.; Colomer-Farrarons, J.; Samitier, J.; Homs-Corbera, A.; Miribel-Catala, P. L., Combined dielectrophoretic and impedance system for on-chip controlled bacteria concentration: Application to Escherichia coli. *Electrophoresis* **2015,** *36* (9-10), 1130-1141.

160. Couniot, N.; Francis, L. A.; Flandre, D., Resonant dielectrophoresis and electrohydrodynamics for high-sensitivity impedance detection of whole-cell bacteria. *Lab on a Chip* **2015,** *15* (15), 3183-3191.

161. Braff, W. A.; Willner, D.; Hugenholtz, P.; Rabaey, K.; Buie, C. R., Dielectrophoresis-Based Discrimination of Bacteria at the Strain Level Based on Their Surface Properties. *Plos One* **2013,** *8* (10).

162. Park, S.; Zhang, Y.; Wang, T. H.; Yang, S., Continuous dielectrophoretic bacterial separation and concentration from physiological media of high conductivity. *Lab on a Chip* **2011,** *11* (17), 2893-2900.

163. Yang, L. J., Dielectrophoresis assisted immuno-capture and detection of foodborne pathogenic bacteria in biochips. *Talanta* **2009,** *80* (2), 551-558.

164. Schroder, U. C.; Beleites, C.; Assmann, C.; Glaser, U.; Hubner, U.; Pfister, W.; Fritzsche, W.; Popp, J.; Neugebauer, U., Detection of vancomycin resistances in enterococci within 3 1/2 hours. *Scientific Reports* **2015,** *5*.

165. Zhang, P. R.; Ren, L. H.; Zhang, X.; Shan, Y. F.; Wang, Y.; Ji, Y. T.; Yin, H. B.; Huang, W. E.; Xu, J.; Ma, B., Raman-Activated Cell Sorting Based on Dielectrophoretic Single-Cell Trap and Release. *Analytical Chemistry* **2015,** *87* (4), 2282-2289.

166. Cheng, I. F.; Chang, H. C.; Hou, D., An integrated dielectrophoretic chip for continuous bioparticle filtering, focusing, sorting, trapping, and detecting. *Biomicrofluidics* **2007,** *1* (2), 021503.

167. Boozer, C.; Yu, Q. M.; Chen, S. F.; Lee, C. Y.; Homola, J.; Yee, S. S.; Jiang, S. Y., Surface functionalization for self-referencing surface plasmon resonance (SPR) biosensors by multi-step self-assembly. *Sensors and Actuators B-Chemical* **2003,** *90* (1-3), 22-30.

168. Vaisocherova, H.; Faca, V. M.; Taylor, A. D.; Hanash, S.; Jiang, S. Y., Comparative study of SPR and ELISA methods based on analysis of CD166/ALCAM levels in cancer and control human sera. *Biosensors & Bioelectronics* **2009,** *24* (7), 2143-2148.

169. Barshavit, Z.; Goldman, R.; Ofek, I.; Sharon, N.; Mirelman, D., MANNOSE-BINDING ACTIVITY OF ESCHERICHIA-COLI - A DETERMINANT OF ATTACHMENT AND INGESTION OF THE BACTERIA BY MACROPHAGES. *Infection and Immunity* **1980,** *29* (2), 417-424.

170. Bouckaert, J.; Mackenzie, J.; de Paz, J. L.; Chipwaza, B.; Choudhury, D.; Zavialov, A.; Mannerstedt, K.; Anderson, J.; Pierard, D.; Wyns, L.; Seeberger, P. H.; Oscarson, S.; De Greve, H.; Knight, S. D., The affinity of the FimH fimbrial adhesin is receptor-driven and quasi-independent of Escherichia coli pathotypes. *Molecular Microbiology* **2006,** *61* (6), 1556-1568.

171. Dobbins, H. M.; Peck, E. R., CHANGE OF REFRACTIVE-INDEX OF WATER AS A FUNCTION OF TEMPERATURE. *Journal of the Optical Society of America* **1973,** *63* (3), 318-320.

172. Yazgan, I.; Noah, N. M.; Toure, O.; Zhang, S. Y.; Sadik, O. A., Biosensor for selective detection of E-coli in spinach using the strong affinity of derivatized mannose with fimbrial lectin. *Biosensors & Bioelectronics* **2014,** *61*, 266-273.

173. Song, S. P.; Wang, L. H.; Li, J.; Zhao, J. L.; Fan, C. H., Aptamer-based biosensors. *Trac-Trends in Analytical Chemistry* **2008,** *27* (2), 108-117.

174. Marton, S.; Cleto, F.; Krieger, M. A.; Cardoso, J., Isolation of an Aptamer that Binds Specifically to E. coli. *Plos One* **2016,** *11* (4).

175. Pickup, R. W., DEVELOPMENT OF MOLECULAR METHODS FOR THE DETECTION OF SPECIFIC BACTERIA IN THE ENVIRONMENT. *Journal of General Microbiology* **1991,** *137*, 1009-1019.

176. Ravindranath, S. P.; Wang, Y. L.; Irudayaraj, J., SERS driven cross-platform based multiplex pathogen detection. *Sensors and Actuators B-Chemical* **2011,** *152* (2), 183-190.

177. Jarvis, R. M.; Goodacre, R., Characterisation and identification of bacteria using SERS. *Chemical Society Reviews* **2008,** *37* (5), 931-936.

178. Yang, L. J., A REVIEW OF MULTIFUNCTIONS OF DIELECTROPHORESIS IN BIOSENSORS AND BIOCHIPS FOR BACTERIA DETECTION. *Analytical Letters* **2012,** *45* (2-3), 187-201.

179. Chung, C. C.; Cheng, I. F.; Yang, W. H.; Chang, H. C., Antibiotic susceptibility test based on the dielectrophoretic behavior of elongated Escherichia coli with cephalexin treatment. *Biomicrofluidics* **2011,** *5* (2).

180. Chung, C. C.; Cheng, I. F.; Chen, H. M.; Kan, H. C.; Yang, W. H.; Chang, H. C., Screening of Antibiotic Susceptibility to beta-Lactam-Induced Elongation of Gram-Negative Bacteria Based on Dielectrophoresis. *Analytical Chemistry* **2012,** *84* (7), 3347-3354.

181. Elitas, M.; Martinez-Duarte, R.; Dhar, N.; McKinney, J. D.; Renaud, P., Dielectrophoresis-based purification of antibiotic-treated bacterial subpopulations. *Lab on a Chip* **2014,** *14* (11), 1850-1857.

182. Su, I. H.; Ko, W. C.; Shih, C. H.; Yeh, F. H.; Sun, Y. N.; Chen, J. C.; Chen, P. L.; Chang, H. C., Dielectrophoresis System for Testing Antimicrobial Susceptibility of Gram-Negative Bacteria to beta-Lactam Antibiotics. *Analytical Chemistry* **2017,** *89* (8), 4635-4641.

183. Hughes, M. P., Fifty years of dielectrophoretic cell separation technology. *Biomicrofluidics* **2016,** *10* (3).

184. Kastanos, E. K.; Kyriakides, A.; Hadjigeorgiou, K.; Pitris, C., A novel method for urinary tract infection diagnosis and antibiogram using Raman spectroscopy. *Journal of Raman Spectroscopy* **2010,** *41* (9), 958-963.

185. Jones, T. B., *Electromechanics of Particles*. Cambridge University Press: New York, NY, 1995.

186. Dick, L. A.; McFarland, A. D.; Haynes, C. L.; Van Duyne, R. P., Metal film over nanosphere (MFON) electrodes for surface-enhanced Raman spectroscopy (SERS): Improvements in surface nanostructure stability and suppression of irreversible loss. *Journal of Physical Chemistry B* **2002,** *106* (4), 853-860.

187. Malaquin, L.; Kraus, T.; Schmid, H.; Delamarche, E.; Wolf, H., Controlled particle placement through convective and capillary assembly. *Langmuir* **2007,** *23* (23), 11513-11521.

188. Weekes, S. M.; Ogrin, F. Y.; Murray, W. A.; Keatley, P. S., Macroscopic arrays of magnetic nanostructures from self-assembled nanosphere templates. *Langmuir* **2007,** *23* (3), 1057-1060.

VITA

D.D. Galvan II received his Bachelor's of Science in Chemical Engineering at the University of Arizona in Tucson, AZ in 2013, and his Master's of Science in Chemical Engineering at the University of Washington in Seattle, WA in 2016. He is expected to receive his Doctor of Philosophy in Chemical Engineering at the University of Washington in Seattle, WA in 2018.

Publications

1. **Galvan, D. D.** and Yu, Q. M., 2018. Surface-Enhanced Raman Scattering for Rapid Detection and Characterization of Antibiotic-Resistant Bacteria. Advanced Healthcare Materials. doi: 10.1002/adhm.201701335.
2. Hou, C., **Galvan, D. D.**, Meng, G. W., and Yu, Q. M., 2017. Long-range surface plasmon resonance and surface-enhanced Raman scattering on X-shaped Au plasmonic nanohole arrays. Physical Chemistry Chemical Physics, 19, pp 24126-24134.
3. Sun F., **Galvan D. D.**, Jain P., Yu Q. M., 2017. Multi-functional, thiophenol-based surface chemistry for surface-enhanced Raman spectroscopy. Chemical Communications, 53 (33), pp 4550-4561.
4. **Galvan, D. D.**, Špačková, B., Slabý, J., Sun, F., Ho, Y., Homola, J., and Yu, Q. M., 2016. Surface-enhanced Raman scattering (SERS) on gold nanohole arrays in symmetrical dielectric environments exhibiting electric field extension. Journal of Physical Chemistry C, 120 (44), pp 25519–25529.
5. Sun, F., Hung, H. C., Sinclair, A., Zhang, P., Tao, B., **Galvan, D. D.**, Jain, P., Li, B., Jiang, S. and Yu, Q. M., 2016. Hierarchical zwitterionic modification of a SERS substrate

enables real-time drug monitoring in blood plasma. Nature Communication, 7, Article number: 13437.

6. Sun, F., Zhang, P., Bai, T., **Galvan, D. D.**, Hung, H.C., Zhou, N., Jiang, S. and Yu, Q. M., 2015. Functionalized plasmonic nanostructure arrays for direct and accurate mapping extracellular pH of living cells in complex media using SERS. Biosensors and Bioelectronics, 73, pp 202-207.
7. Sun, F., Ella-Menye, J. R., **Galvan, D. D.**, Bai, T., Hung, H. C., Chou, Y. N., Zhang, P., Jiang, S. and Yu, Q. M., 2015. Stealth surface modification of surface-enhanced Raman scattering substrates for sensitive and accurate detection in protein solutions. ACS Nano, 9(3), pp 2668-2676.
8. Deng Y., Idso M.N., **Galvan D.D.**, Yu Q.M., 2015. Optofluidic microsystem with quasi-3 dimensional gold plasmonic nanostructure arrays for online sensitive and reproducible SERS detection. Analytical Chimica Acta 2015. 863 pp 41-49.